ISSN 2074-272X

науково-практичний журнал

2021/4

Електротехніка і Електромеханіка

Electrical Engineering & Electromechanics

Інженерна електрофізика.
Техніка сильних електричних та магнітних полів
Електричні машини та апарати
Електротехнічні комплекси та системи
Електричні станції, мережі і системи
Електричний транспорт

Журнал включено до найвищої категорії «А»
Переліку фахових видань України

З 2015 р. журнал індексується у міжнародній наукометричній базі Web of Science Core Collection: Emerging Sources Citation Index

«ELECTRICAL ENGINEERING & ELECTROMECHANICS»

Scientific Journal was founded in 2002

Founders are:

National Technical University «Kharkiv Polytechnic Institute» (Kharkiv, Ukraine)

State Institution «Institute of Technical Problems of Magnetism of the NAS of Ukraine» (Kharkiv, Ukraine)

Journal «Electrical Engineering & Electromechanics» from no. 1 2015 is indexing in Web of Science Core Collection : Emerging Sources Citation Index (ESCI).

Also included in DOAJ (Directory of Open Access Journals), in EBSCO's database, in ProQuest's databases – Advanced Technologies & Aerospace Database and Materials Science & Engineering Database, in Gale/Cengage Learning databases.

Editorial office address:

National Technical University «Kharkiv Polytechnic Institute», Kyrpychova Str., 2, Kharkiv, 61002, Ukraine

phones: +380 57 7076281, +380 67 3594696, **e-mail:** a.m.grechko@gmail.com (**Grechko O.M.)**

ISSN (print) 2074-272X

ISSN (online) 2309-3404

Printed 27 August 2021. Format 60 × 90 ⅛. Paper – offset. Laser printing. Edition 200 copies.

Printed by Printing house «Madrid Ltd» (18, Gudanova Str., Kharkiv, 61024, Ukraine)

ELECTRICAL ENGINEERING & ELECTROMECHANICS
Scientific journal

no. 4, 2021

TABLE OF CONTENTS

Electrical Machines and Apparatus

Bouchaoui L., Hemsas K.E., Mellah H., Benlahneche S. Power transformer faults diagnosis using undestructive methods (Roger and IEC) and artificial neural network for dissolved gas analysis applied on the functional transformer in the Algerian north-eastern: a comparative study **3**

Milykh V.I., Tymin M.G. A comparative analysis of the parameters of a rotating magnetic field inductor when using concentric and loop windings **12**

Shevchenko V.V., Minko A.N., Dimov M. Improvement of turbogenerators as a technical basis for ensuring the energy independence of Ukraine **19**

Electrotechnical Complexes and Systems

Benbouhenni H., Driss A., Lamdani S. Indirect active and reactive powers control of doubly fed induction generator fed by three-level adaptive-network-based fuzzy inference system – pulse width modulation converter with a robust method based on super twisting algorithms **31**

Denisov Y.O, Denisov O.I., Bursala O.O. Synthesis of the digital regulator of the main contour of the three-circuit system of the linear electric drive of the working body of the mechanism of onboard aviation equipment **39**

Engineering Electrophysics. High Electric and Magnetic Field Engineering

Brzhezitsky V.O., Haran Y.O., Derzhuk A.O., Protsenko O.R., Trotsenko Y.O., Dixit M.M. Ultimate effect of non-identity of capacitive elements of high-voltage arm on frequency characteristics of voltage divider (analytical research) **46**

Power Stations, Grids and Systems

Boussaid A., Chelli S.E.I., Nemmour A.L., Khezzar A. An effective control algorithm for dynamic voltage restorer under symmetrical and asymmetrical grid voltage conditions **53**

Electric Transport

Omelyanenko V.I., Riabov Ie.S., Overianova L.V., Omelianenko H.V. Traction electric drive based on fuel cell batteries and on-board inertial energy storage for multi unit train **64**

UDC 621.314 https://doi.org/10.20998/2074-272X.2021.4.01

L. Bouchaoui, K.E. Hemsas, H. Mellah, S. Benlahneche

POWER TRANSFORMER FAULTS DIAGNOSIS USING UNDESTRUCTIVE METHODS (ROGER AND IEC) AND ARTIFICIAL NEURAL NETWORK FOR DISSOLVED GAS ANALYSIS APPLIED ON THE FUNCTIONAL TRANSFORMER IN THE ALGERIAN NORTH-EASTERN: A COMPARATIVE STUDY

Introduction. *Nowadays, power transformer aging and failures are viewed with great attention in power transmission industry. Dissolved gas analysis (DGA) is classified among the biggest widely used methods used within the context of asset management policy to detect the incipient faults in their earlier stage in power transformers. Up to now, several procedures have been employed for the lecture of DGA results. Among these useful means, we find Key Gases, Rogers Ratios, IEC Ratios, the historical technique less used today Doernenburg Ratios, the two types of Duval Pentagons methods, several versions of the Duval Triangles method and Logarithmic Nomograph.* ***Problem***. *DGA data extracted from different units in service served to verify the ability and reliability of these methods in assessing the state of health of the power transformer.* ***Aim.*** *An improving the quality of diagnostics of electrical power transformer by artificial neural network tools based on two conventional methods in the case of a functional power transformer at Sétif province in East North of Algeria.* ***Methodology***. *Design an inelegant tool for power transformer diagnosis using neural networks based on traditional methods IEC and Rogers, which allows to early detection faults, to increase the reliability, of the entire electrical energy system from transport to consumers and improve a continuity and quality of service.* ***Results***. *The solution of the problem was carried out by using feed-forward back-propagation neural networks implemented in MATLAB- Simulink environment. Four real power transformers working under different environment and climate conditions such as: desert, humid, cold were taken into account. The practical results of the diagnosis of these power transformers by the DGA are presented.* ***Practical value.*** *The structure and specific features of power transformer winding insulation ageing and defect state diagnosis by the application of the artificial neural network (ANN) has been briefly given. MATLAB programs were then developed to automate the evaluation of each method. This paper presents another tool to review the results obtained by the delta X software widely used by the electricity company in Algeria.* References 29, table 15, figures 9.

Key words: **analysis of dissolved gases in oil, diagnostics of power transformers, feed-forward neural networks, Rogers method, IEC method.**

Вступ. *У наш час старіння та несправності силових трансформаторів уважно розглядаються у галузі передачі електричної енергії. Аналіз розчиненого газу виділяється серед найбільш широко використовуваних методів, що застосовуються в контексті політики управління активами для виявлення початкових несправностей на їх попередній стадії в силових трансформаторах. Дотепер для отримання результатів аналізу розчиненого газу було використано кілька процедур. Серед цих корисних засобів зазначимо такі, як метод основних газів, коефіцієнти Роджерса, коефіцієнти МЕК, історичний підхід, менш використовувані сьогодні коефіцієнти Дерненбурга, два типи методів п'ятикутників Дюваля, кілька варіантів методу трикутників Дюваля та логарифмічний номограф.* ***Проблема***. *Дані аналізу розчиненого газу, отримані з різних об'єктів, що експлуатуються, слугували для перевірки здатності та надійності цих методів при оцінці стану працездатності силового трансформатора.* ***Мета.*** *Підвищення якості діагностики електричного силового трансформатора за допомогою штучних нейромережевих інструментів, заснованих на двох звичайних методах, у випадку функціонуючого силового трансформатора в провінції Сетіф на північному сході Алжиру.* ***Методологія***. *Розробка нетипового засобу для діагностики силових трансформаторів з використанням нейронних мереж на основі традиційних методів МЕК і Роджерса, який дозволяє раннє виявлення несправностей, підвищення надійності всієї електроенергетичної системи від передачі енергії до споживачів та покращення безперервності та якості обслуговування.* ***Результати.*** *Розв'язання проблеми було здійснено за допомогою нейронних мереж зворотного розповсюдження із зворотним зв'язком, реалізованих в середовищі MATLAB-Simulink. Були враховані чотири діючі силові трансформатори, що працюють в різних умовах оточуючого середовища та клімату, таких як: пустеля, волога, холод. Представлені практичні результати діагностики цих силових трансформаторів з використанням аналізу розчиненого газу.* ***Практичне значення***. *Стисло наведено структуру та специфічні особливості старіння ізоляції обмоток силових трансформаторів та діагностики стану дефектів за допомогою штучної нейронної мережі. Далі були розроблені програми у MATLAB для автоматизації оцінки кожного методу. Ця стаття представляє ще один засіб для аналізу результатів, отриманих за допомогою програмного забезпечення delta X, що широко використовується електричною компанією в Алжирі.* Бібл. 29, табл. 15, рис. 9.

Ключові слова: **аналіз розчинених газів у маслі, діагностика силових трансформаторів, нейронні мережі зі зворотним зв'язком, метод Роджерса, метод МЕК.**

Introduction. The power transformer is a capital device in the power electrical system and we can't give up it, many researchers interested to diagnosis and protect the power transformers to improve their lifespan, their performance and their reliability [1-5]. For that, improved techniques for power transformer diagnosis and early fault detection are really important. The transformer is subject to electrical and thermal stresses. These two stresses could break down the insulating materials and release gaseous decomposition products.

According to literature [4, 6-11], the main causes of power transformer faults related gases are: overheating, corona, cellulose degradation by overheating (OH) and arcing (ARC).

Principally, gases generated from several well-known faults involved inside the active parts are represented in the Table 1 [3].

Dissolved gas analysis (DGA) is widely used for diagnosing the developing faults in power transformers,

this method is classified among effective methods. Several diagnostic criteria have been developed to interpret the dissolved gases inside the power transformers [3], the interested reader is referred to IEEE Guide [12] for more details. These methods should be able to get the relations between the dissolved gases inside a power transformer and distinguishing the type of fault that occurred. Some of these relations are clear, others are less obvious and ambiguous, or even hidden relations [13]. Yet, much of the power transformer diagnostic data requires expert hands to properly analyze, approve and interpret its results[3, 13].

Table 1

Gases generated inside the power transformer due to several faults

Chemical symbol	Name gas
H_2	Hydrogen
CH_4	Methane
C_2H_2	Acetylene
C_2H_6	Ethane
C_2H_4	Ethylene
CO	Carbon monoxide
CO_2	Carbon dioxide

Non-conventional methods are usually computer-aided, will be able to detect reliably and efficiency the incipient-faults for the inexperienced engineer. More than that, in certain cases, even the well experienced engineers can benefit further insights [13], several researches have been published in [14].

Artificial intelligence and/or optimization algorithm-based expert systems [4, 7-11, 15-18] have been developed to expose some of the secret relations to well interpret the dissolved gases in purpose of power transformer fault diagnosis.

The artificial neural network (ANN) method was also applied to this type of study, by exploiting their capacities, their properties in terms of learning and their processing of complex data in order to extract the ambiguous relations between dissolved gases inside the power transformer and the type of faults. Zhang et al. in [11] use a two-step ANN approach in order to detect faults in the diagnosis of power transformers by DGA without cellulose involved or even with cellulose involved.

Bondarenko et al. in [4] combine two powerful technique and propose a fuzzy-ANN to power transformer oil gases analysis.

Enriquez et al. in [19] propose as tools for power transformer diagnosis a K-Nearest Neighbors algorithm (K-NN) classifier with weighted classification distance, applied to a DGA data, where K-NN is one of the most fundamental and basic classifiers widely used in pattern recognition applications, this classifier was developed by T.M Cover et al in 1967 [20].

A two types of feed-forward neural network classifiers for power transformer diagnosis has been designed and used by Seifeddine et al. in [21], the two types are MLP and the Radial Basis Function (RBF). In order to train the two NN classifier the authors get the experimental data from the Tunisian Company of Electricity and Gas (STEG).

However, the diagnosis presented by [21] is not precise enough in certain types of faults such as partial discharge (PD) and temperature overheating faults. Where in PD fault condition for [21] it is only one type of fault, whereas in our work here, we separate between PD faults with low energy density and with high energy density faults.

Likewise, with regard to temperature overheating, [21] present three ambiguous overheating levels: low, medium and high, while in our study the diagnosis is precise and divided into four different states limited by clear numerical values; which more clearly show the thermal state of power transformer.

This diagnosis allows us to judge whether or not the maintenance of the power transformer is necessary. In the worst cases, immediate shutdown. This judgement is depending on the maximum temperature supported by the insulation.

The goal of the work is to improve the quality of diagnostics of electrical power transformer by artificial neural network tools based on two conventional methods in the case of a functional power transformer at Sétif province in east north Algeria. The type of the used ANN is Feedforward Neural Network (FNN) trained by Levenberg-Marquardt Backpropagation (LMBP). The training patterns set used to learn ANN are a practical result obtained in this functional power transformer.

Dissolved gas-in-oil analysis. In power transformer faults detection and analysis, dissolved gas in oil analysis (DGA) is a famous standard practice. The origin of this method goes back to 1973, where Halstead carried out of study in formation of gaseous hydrocarbons in faulty transformers based on thermodynamic assessment [11]. Under extreme thermal and electrical pressures applied to the power transformer, also under the effect of aging, mineral oils and cellulosic materials used for winding electrical insulations of a power transformer are degrading. This degradation of the material results in several types of gas emitted inside that we can use them as identifying indices of the type and intensity of the stresses. To estimate the transformer health-state, concentrations of dissolved gas in oil, relative gases proportions and gas creation rates, are analyzed and applied [13]. The most common gases used for diagnostics are given in Table 1.

In the goal to obtain each gas concentration separately we collect it from high-vacuum, then we use the gas chromatography techniques to analyze them [22]. It is possible to diagnose existing defects in the power transformers by interpretation of the gas contents. The specialist literature presents several methods for interpreting these diagnosis results [3]. Several method of power transformers diagnostic by DGA has been developed, we can classify them by two main types, classical and hybrid methods; where the classical types generally are: Key gases, Doernenburg ratio, Duval triangle, Rogers ratio, pentagon and IEC methods [6, 15, 17, 22, 23]. However, the second type generally associate one or more of the classical methods with an artificial intelligent [4, 7-11], probabilistic approach [15, 16] or with optimization method [17, 18].

Key gas method. This method uses four individual gas levels (C_2H_4, CO, H_2, C_2H_2), they are often called «key gases» to detect four types of faults; this method

depends on the amount of fault gas emitted in the power transformer by the insulating oil under the effect of the varying temperatures at the chemical structure breaks [12, 13, 22]. Unfortunately, this methodology suffers from its findings or it may be incorrect or inconclusive; it can reach 50 % if it is automatically implemented with software, this error can be reduced to 30 % if it is applied manually by experienced DGA users [12].

Ratios methods. There are several types of ratios method [3, 12, 22] where each method assigns some combination of codes individually to a particular form of fault [22]. These methods are based on comparing the current gas ratios to the preset ratio intervals.

The principle of fault detection is simple and is as follows once a combination of codes matches the code pattern of the fault the fault is detected [13, 22]. As a result of the amount of doable code combination is larger than the amount of fault sorts, the typical result of Ratio' strategies such as Doernenburg ratios, Rogers ratios and IEC ratios is generally «no decision» [13], this is one of their important limitations, several of their limitations are described in [12], these limitations either no decision or false detection were verified in our study as shown at the end of this article in Table 15.

Other details like the variability of dissolved-gas data, loading and environmental conditions effects on these data are typically often taken into account in a real power transformer diagnostic process [24].

ANN can identify the hidden relations between the types of faults and dissolved gases in the power transformer [3] therefore, the ANN approach can be applied more carefully to solve this issue.

Gas ratio methods. The major benefits of using Ratios techniques in monitoring the health of the power transformer are that the problem of oil volume does not arise. Because this technique needs to compute the Gases Ratios to detect a fault, and its independent of its absolute values [3]. The Ratios techniques applied in this research are the Rogers Ratio and the IEC techniques.

Rogers ratio method. Four ratios are applied in this assessment: methane/hydrogen, ethane/methane, ethylene/ethane, and acetylene/ethylene. The fault diagnosis process of power transformer is achieved through a simple coding scheme based on ratio ranges. Four states of power transformer condition can be identified i.e. normal ageing, PD with or without tracking, thermal fault and electrical fault of various degrees of severity, the Table 2 give the Roger's ratio codes [3, 25]

Table 2

Roger's ratio codes

Ratios	Range	Code
Methane / Hydrogen	≤ 0.1	5
	$0.1 < ... < 1$	0
	$1 \leq ... < 3$	1
	$3 \leq$	2
Ethane / Methane	< 1	0
	$1 \leq$	1
Ethylene / Ethane	< 1	0
	$1 \leq ... < 3$	1
	$3 \leq$	2
Acetylene / Ethylene	< 0.5	0
	$0.5 \leq ... < 3$	1
	$3 \leq$	2

Table 3 gives the Roger's fault diagnosis table [25].

Table 3

Roger's fault diagnosis table

N	Code				Diagnosis
1	0	0	0	0	Normal (N)
2	5	0	0	0	Partial discharge of low energy
3	1.2	0	0	0	Overheating < 150 °C
4	1.2	1	0	0	Overheating 150 -200 °C
5	5	1	0	0	Overheating 200-300 °C
6	0	0	1	0	Conductor Overheating
7	1	0	1	0	Overheating by winding circulating current
8	1	0	2	0	Overheating by core and tank circulating current
9	0	0	0	1	Arcing of low energy
10	0	0	1.2	1.2	Arcing of high energy
11	0	0	2	2	Continuous sparking to floating potential
12	5	0	0	1.2	Partial discharge with high energy

IEC method. The exclusion for the Ethane/Methane ratio was dropped from the diagnostic instructions suggested by IEC, as is indicate only a small decomposition temperature range, the IEC method is derived from the Rogers' technique. In the IEC process, three gas ratios are computed and we use it for the failure's interpretation, IEC can identify four types of faults as fellow: normal ageing, PD of low and high energy density, thermal faults and electrical faults of various degrees of severity [3, 26].

The codes for various gas ratios and their description for the IEC method are presented in Table 4 and 5. On the other hand, the downside to these Ratios approaches is that all data ranges are not covered and ratios fall beyond the reach of the tables very frequently [13]. In this work, an ANN technique was used to resolve the above limited ratios process limitation.

Table 4

IEC ratio codes

Defined range of the gas ratio	Codes of different gas ratio		
	C_2H_2/C_2H_4	CH_4/H_2	C_2H_4/C_2H_2
< 0.1	0	1	0
0.1-1	1	0	0
1-3	1	2	1
> 3	2	2	2

Table 5

IEC fault diagnosis table

N	Fault type	code		
1	No Fault	0	0	0
2	Partial discharge with low energy density	0	1	0
3	Partial discharge with high energy density	1	1	0
4	discharge of low energy	1.2	0	1.2
5	discharge of high energy	1	0	2
6	Overheating T< 150 °C	0	0	1
7	Overheating 150< T< 300 °C	0	2	1
8	Overheating 300≤ T≤ 700 °C	0	2	1
9	Overheating ≥ 700 °C	0	2	2

DGA practical diagnostic results for different region in Algeria. In this section we present a DGA practical diagnostic results in four different regions.

Case 1. Mobile station 220 kV, 40 MVA of El-Meghier (province has a hot desert climate, with very little precipitation). Through a periodic inspection,

a DGA pattern has revealed the existence of partial discharges symptoms from the critical amount extracted of H_2 and C_2H_2 (Table 6).

Table 6

DGA values of El-Meghier transformer

Gases (PPM)	Before treatment	After treatment	
	17 April 2001	6 May 2003	24 May 2005
H_2	111	27	41
CO_2	2188	1757	2737
CO	293	316	419
CH_4	26	1	< 1
C_2H_4	31	20	< 1
C_2H_6	9	14	< 1
C_2H_2	65	< 1	< 1

The advised maintenance action was then a physical treatment of the transformer via the oil purification. Several samplings were done after this operation and there was not any sign of the previous defect. Because the transformer was fitted by a forced oil flow system, we have thought about the existence of particles attracted on the surface of windings or in any region with high electric or magnetic field. These particles were removed by circulating the oil during the purification as shown in Fig. 1.

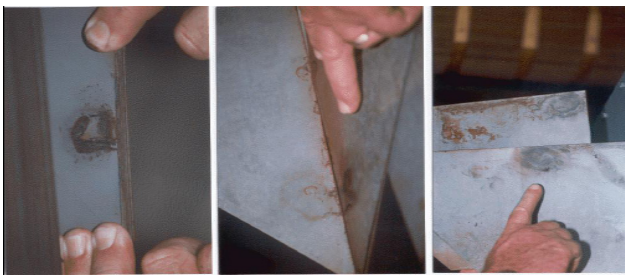

Fig. 1. Remove the particles by circulating the oil during the purification

The DGA practical measure results of El-Meghier transformer for three different years presented in Table 6 are graphically shows by Fig. 2.

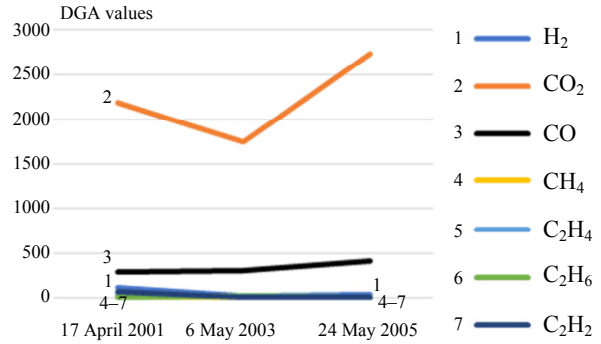

Fig. 2. DGA trends of El-Meghier transformer

Case 2. Mobile station 220 kV 40 MVA of Sidi-Aiche (town in middle northern Algeria with a moderate and humid climate). This transformer presented a high value of a dielectric losses factor of the oil (0.21) even though the water concentration was normal (11 ppm). The DGA revealed abnormal proportions of methane, ethane, CO and CO_2 concentrations giving an idea about the loading of the transformer. Furanic compounds analysis confirmed the existence of a 2-FAL (Table 7) in dangerous amount produced as result of an advanced aging process of the solid insulation. The elapsed life of the transformer was estimated at 80 %. It was then very necessary to check the reliability of our protections and to rate the transformer at a moderate loading until its inspection.

Table7

DGA values of Sidi-Aiche transformer

Gases (ppm)	Values	Dielectric parameters	Values
H_2	11	H_2O in ppm	11
CO_2	1944		
CO	597	tgδ	0.21
CH_4	101		
C_2H_4	< 1	2-Furfuraldehyd in PPM	5.79
C_2H_6	110		
C_2H_2	< 1		

Case 3. Power transformer 60 kV of Akbou (industrial town in northern Algeria with a moderate and humid climate). An excess of combustible gases concentration was registered through a DGA as shown in Table 8; a more dangerous one was the acetylene. A gases ratio confirmed a thermal overheating involving a solid insulation. Perhaps it touched the current flow system as LTC contacts, leads contacts, etc. This is the most critical case that may result in catastrophic failure. The main action was to stop the transformer for an internal inspection.

Table 8

Gases concentration of Akbou unit

Gases	Values (ppm)
H_2	1443
CO_2	13561
CO	934
CH_4	3899
C_2H_4	600
C_2H_6	1115
C_2H_2	113

A hot spot was found at the contacts level of one connection of the no load tap changer with apparent signs of tracking, cocking, erosion and overheating with the surrounded insulation as illustrated by Fig. 3.

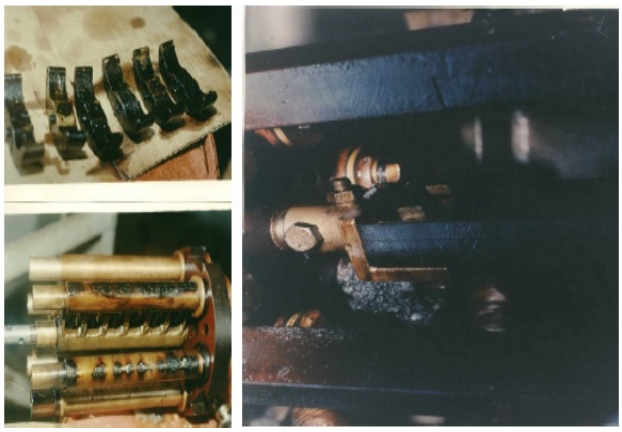

Fig. 3. Remove the particles by circulating the oil during the purification

Case 4. Autotransformer 220/150 kV of Darguina (town in northern Algeria with cold and very humid climate). This unit exhibited a high arcing in the oil

without involving the solid insulation. It has been treated several times but there was no improvement of the situation because successive Buckholz alarms have been registered after (Table 9). The power transformer was de-energized and submitted to further analysis and diagnostic tests.

Table 9

DGA history of Darguinas autotransformer

Gas (ppm)	17 April 2001	14 March 2003	23 May 2005
H_2	107	<1	645
CO_2	1414	434	2099
CO	–	40	217
CH_4	27	<1	45
C_2H_4	25	<1	51
C_2H_6	18	<1	<1
C_2H_2	65	7	326

Complementary electrical tests have been investigated in order to assess the integrity of the current circuit and the windings condition. The results were normal (Table 10 and Table 11) and the problem causing this generation of gases still not detectable.

- Insulation measure: Primary/Ground = 7 GΩ;
- Secondary/Ground = 5 GΩ.

Table 10

Winding resistance measurement with different tap position

	150 kV			220 kV		
Position	A/N	B/N	C/N	A/N	B/N	C/N
5	3.53	3.57	3.53	5.02	5.03	5.01
4	3.48	3.51	3.49	4.83	4.92	4.83
3	3.49	3.50	3.48	4.66	4.68	4.61
2	3.49	3.50	3..50	4.79	4.78	4.77
1	3.50	3.50	3.50	4.92	5.02	4.95

Table 11

Transformation ration

Position	AB/ab	AC/ac	BC/bc	Nameplate value
1	1.553	1.557	1.555	1.557
2	1.502	1.504	1.504	1.506
3	1.452	1.453	1.453	1.455
4	1.401	1.403	1.402	1.404
5	1.350	1.352	1.351	1.353

This mode of failure may be also created by the magnetic stray flux. The internal inspection revealed an overheating localized in the connection bolts of the core yoke caused by arcing of a formed closed loop. Fig. 4 illustrates a hotspot localized in power transformer.

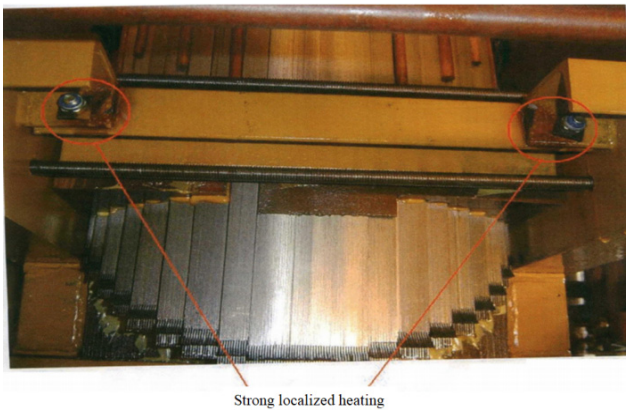

Fig. 4. Hotspot localized

Artificial Neural Networks. ANN has demonstrated their capacity in a varied engineering application such as, estimation, process control, diagnostics [27], it is ANN's ability and malleability to approximate functions, data meaning and classifications that have nominated it to be a proposed and promising solution that can be used in various types of complex issues. These properties are particularly very significant when the process or the state variables of the process model are nonlinear, poorly identified and uncertain, therefore hard to model by known traditional methods.

An ANN is a complex and dynamic system of different topology which is composed by weights linked together either complete or partial depending on the type of ANN, these weights are an element of complex data processing. We can summarize the principal advantages when we apply ANN in the diagnosis process of power transformer by dissolved gas as follow [28]:

- high learning capacity hence generalization of the developed tool;
- development of electronic circuits make the hardware implementation easier;
- a great capability for model a complex system based on their inputs and outputs without needing to know exactly the mathematical model;
- minimize the time required to give the final diagnosis results by eliminating the time required to conduct laboratory experiments

Several types of ANN are presented in the literature in terms of topology, backpropagations algorithm and learning mode, among these types Multi-Layer Perceptron (MLP) is the most widely used [27]. Fig 5 shows the structure of MLP, which is a type of ANN used in this research. The weight outputs are computed as follows [7]

$$S_j = f\left(\sum_{i=1}^{n} X_i W_{ij} + \theta_j\right), \quad (1)$$

where X_i are the network inputs will be described in the following section; W_{ij} translate the weight-connection between the input neuron i and the neighboring hidden neuron j; θ_j is the bias of the j-th hidden neuron; f is the transfer function or also called activation function.

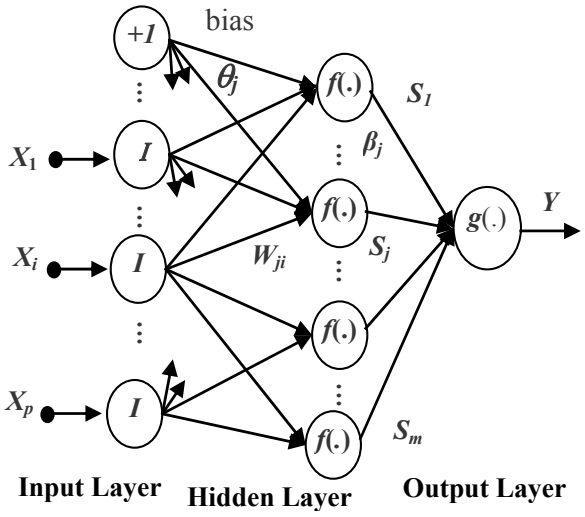

Fig. 5. ANN topology

Topology of ANN used. In this application, a MLP type ANNs with supervised training based on Levenberg-Marquardt Backpropagation (LMBP) algorithm is used. LMBP which remains until now the most widely applied. According to the literature related to this topic, LMBP has a good robustness, known for its high efficiency and relatively fast require much less iteration to converge compared to some methods, for this many researchers suggest to use it for power transformer diagnosis based on DGA.

The optimal size of the ANN that produces the best results is one of the most frequently phrased questions in the ANN computation framework. Even though numerous «hints and tips» such as suggestions have been highlighted so far by many researchers, but there is still no straightforward answer to this ANN issue [29].

We using Matlab/Simulink environment to design this ANN, we notice that each method has its self inputs and should be match the same as the number of neurons in the input layer, the same thing for the output layer the number of units should be the same outputs for each method.

In this application case, five main preliminary gases for a failure in power transformers: Acetylene (C_2H_2), Ethane (C_2H_6), Ethylene (C_2H_4), Hydrogen (H_2) and methane (CH_4) are elected as the inputs characteristics as illustrated by Fig. 6.

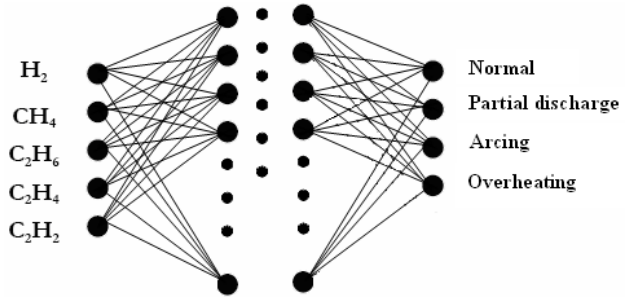

Fig. 6. Input and output of the neural network

Input layer. The ANN inputs are a vector contains the Rogers and IEC Ratios. Generally, the number of neurons is equal to the number of inputs and the activation function are linear. Each method has its inputs of the follow gases: Acetylene (C_2H_2), Ethane (C_2H_6), Hydrogen (H_2), Ethylene (C_2H_4) and Methane (CH_4) in ppm.

Output layer. Contains the desired outputs of the artificial neural network, in our case are the type of faults if exist or the power transformer is healthy as presented by Fig. 6. The outputs are: discharge of low energy and high energy, arcing, overheating, or normal case which means healthy state. Each method has a specific fault detection, the activate function generally are linear function.

Hidden layer. The wide majority of studies in classification problems use a single layer or at most two hidden layers. There is no law to determine exactly the number of neurons in the hidden layer and it is defined by trial in order to get the minimum error.

Transfer function. At the hidden layer, the activation function most widely used in the networks of neurons is sigmoid tangent (logsig), Fig. 7 show its curvature.

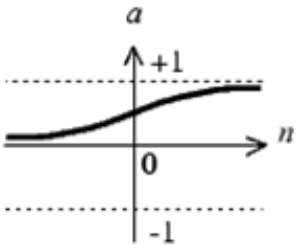

$a = \text{logsig}(n)$

Fig .7. Activation function

The optimized ANNs used in the process of power transformer diagnosis is carried out by adjusting the number of hidden layer and the number of units in each hidden layer of the MLP. Rogers Ratios and IEC Ratios methods are two Ratios approaches investigated in this study. We are using the cross-validation error method over multiple sets both for Rogers and IEC training data to find the best results.

Input data. The inputs data are the gas concentrations given by the chromatographic analysis tests of the oil samples, these samples are taken over the life of the transformer (training step), or suspected in the data set sample (net value under regular conditions of use). Table 12 displays the sample data set in concentrations of principal gases in ppm.

Table 12

Samples data

Samples	H_2	CH_4	CO	CO_2	C_2H_4	C_2H_6	C_2H_2	Known fault
1	17	15	292	6956	78	20	35	ARC
2	1046	2809	681	7820	321	675	7	PD
3	127	76	879	3471	23	32	49	ARC
4	11	101	597	1944	110	<1	<1	OH
5	107	27	–	1414	18	25	65	ARC
6	39	33	991	3280	9	7	2	Normal
7	72	278	53	610	176	289	<1	OH
8	1	39	361	4081	9	36	1	Normal
9	111	26	293	2188	31	9	65	PD
10	1443	3899	934	13561	600	1115	113	OH

The database of diagnostics was created at the power transformer park in the Sétif region, then has helped us to make sure for the sensitivity of our programs and the degree of its reproducibility; where several comparisons of the acquired results was making with the DELTA X software used in the Sonelgaz-GRTE laboratories or the shared data and others are considered to view the established convergences.

Application of ANN to DGA diagnosis using IEC method. The input vector

$$\boldsymbol{I} = [\boldsymbol{I}_1, \boldsymbol{I}_2, \boldsymbol{I}_3] = \left[code\left(\frac{Acetylene(C_2H_2)}{Ethylene(C_2H_4)} \right), \right.$$

$$\left. code\left(\frac{Ethylene(C_2H_4)}{Hydrogen(H_2)} \right), code\left(\frac{Ethylene(C_2H_4)}{Ethane(C_2H_6)} \right) \right],$$

these codes are extracted following the IEC method shown in Table 4.

The output vector $\boldsymbol{O}$ in IEC method has nine detectable defects as shown in Table 13, $\boldsymbol{O} = [\boldsymbol{O}_1, ..., \boldsymbol{O}_9]$.

Table 13

Database trained by IEC Ratios Method

Inputs			Outputs								
$\boldsymbol{I}_1$	$\boldsymbol{I}_2$	$\boldsymbol{I}_3$	$\boldsymbol{O}_1$	$\boldsymbol{O}_2$	$\boldsymbol{O}_3$	$\boldsymbol{O}_4$	$\boldsymbol{O}_5$	$\boldsymbol{O}_6$	$\boldsymbol{O}_7$	$\boldsymbol{O}_8$	$\boldsymbol{O}_9$
0	0	0	1	0	0	0	0	0	0	0	0
0	1	0	0	1	0	0	0	0	0	0	0
1	1	0	0	0	1	0	0	0	0	0	0
1,2	0	1,2	0	0	0	1	0	0	0	0	0
1	0	2	0	0	0	0	1	0	0	0	0
0	0	1	0	0	0	0	0	1	0	0	0
0	2	0	0	0	0	0	0	0	1	0	0
0	2	1	0	0	0	0	0	0	0	1	0
0	2	2	0	0	0	0	0	0	0	0	1

The neural network with the IEC method is composed by three unites in input layer, the hidden layers comprise a variable number of unites and the output layer has nine unites. The unites of the output layers generate a real number between 0 and 1 indicating the possibility of presence of a fault among the 9 faults designated by IEC instructions norms. The models of formation for the IEC technique are presented in Table 13.

Application of ANN to DGA diagnosis using Rogers method. The vector of inputs

$$\boldsymbol{I} = [\boldsymbol{I}_1, \boldsymbol{I}_2, \boldsymbol{I}_3, \boldsymbol{I}_4] = \left[\left(\frac{Methane}{Hydrogen}\right), \left(\frac{Ethane}{Methane}\right), \left(\frac{Ethylene}{Ethane}\right), \left(\frac{Acetylene}{Ethylene}\right)\right],$$

these codes are extracted following the Rogers method shown in Table 2.

The output vector $\boldsymbol{O}$ in Rogers method has 12 detectable defects as shown in Table 2, $\boldsymbol{O} = [\boldsymbol{O}_1, ..., \boldsymbol{O}_{12}]$.

The neural network with the Rogers method is composed by 4 unites in the input layer; the hidden layers contain a variable number of neurons and the output layers has twelve unites. The neurons of the output layers generate a real number between 0 and 1 giving the likelihood of the presence of a fault amongst the twelve faults designated by the Rogers' procedure. The models of formation for the Rogers technique are exposed by Table 14 below.

Figure 8 shows the ANN training performance step trained by LMBP algorithm based on IEC set.

Figure 9 shows the ANN training performance step trained by LMBP algorithm based on Rogers set.

Results and discussions. The two artificial neural networks elaborate previously needs to be checked after the training step is done. In order to test and verify the robustness and the best performance of the trained ANN, a data set pattern of known cause of power transformer faults was considered in 10 test samples given in Table 12.

Table 14

Data sets trained by Rogers Ratios technique

Inputs				Outputs											
$\boldsymbol{I}_1$	$\boldsymbol{I}_2$	$\boldsymbol{I}_3$	$\boldsymbol{I}_4$	$\boldsymbol{O}_1$	$\boldsymbol{O}_2$	$\boldsymbol{O}_3$	$\boldsymbol{O}_4$	$\boldsymbol{O}_5$	$\boldsymbol{O}_6$	$\boldsymbol{O}_7$	$\boldsymbol{O}_8$	$\boldsymbol{O}_9$	$\boldsymbol{O}_{10}$	$\boldsymbol{O}_{11}$	$\boldsymbol{O}_{12}$
0	0	0	0	1	0	0	0	0	0	0	0	0	0	0	0
5	0	0	0	0	1	0	0	0	0	0	0	0	0	0	0
1,2	0	0	0	0	0	1	0	0	0	0	0	0	0	0	0
1,2	1	0	0	0	0	0	1	0	0	0	0	0	0	0	0
0	1	0	0	0	0	0	0	1	0	0	0	0	0	0	0
0	0	1	0	0	0	0	0	0	1	0	0	0	0	0	0
1	0	1	0	0	0	0	0	0	0	1	0	0	0	0	0
1	0	2	0	0	0	0	0	0	0	0	1	0	0	0	0
0	0	0	1	0	0	0	0	0	0	0	0	1	0	0	0
0	0	1,2	1,2	0	0	0	0	0	0	0	0	0	1	0	0
0	0	2	2	0	0	0	0	0	0	0	0	0	0	1	0
5	0	0	1,2	0	0	0	0	0	0	0	0	0	0	0	1

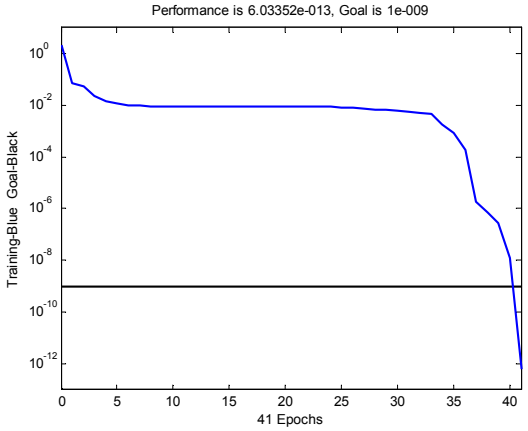

Fig. 8. Training performance using LMBP with IEC Ratios method

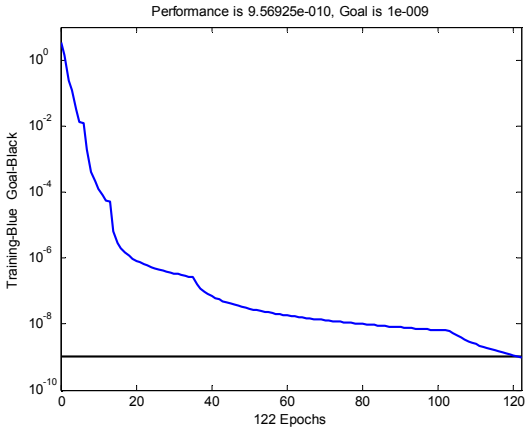

Fig. 9. Training phase performance using LMBP and Rogers Ratios method

Table 15 summarizes the findings obtained by the two ANN during testing. According to these results, ANN associates to Rogers Ratios methods was correctly diagnosed 8 faults out of 10 faults. However, ANN associated with IEC Ratios methods only detect 7 faults.

According to our results, the ANN solves all limitations of type no decision of the traditional methods

(IEC and Roger) and give a decision, for ANN based Roger ration method all these decisions are correct compared the experiment. However, for ANN based on IEC method the decision is wrong for the sample 2 and 8. In other hand, the improved IEC by ANN correct the diagnosis result of traditional IEC for the sample 1. As illustrated by Table 15 all traditional or ANN-based methods give wrong results for samples 2 and 8, and the work should be done by more efficient and robust methods as a deep learning.

Table 15

Comparison results between ANN DGA and traditional DGA based on Rogers and IEC

Samples	Actual fault	Fault from traditional IEC method	Fault from traditional Rogers method	Predicted fault from ANN	
				IEC Method	Rogers Method
1	ARC	PD	No decision	ARC	ARC
2	PD	No decision	OH	OH	OH
3	ARC	No decision	ARC	ARC	ARC
4	OH	OH	No decision	OH	OH
5	ARC	No decision	No decision	ARC	ARC
6	N	PD	OH	PD	Normal
7	OH	No decision	OH	OH	OH
8	N	No decision	OH	OH	OH
9	PD	PD	ARC	PD	OH
10	OH	No decision	OH	OH	OH

Conclusions.

The dissolved gas analysis has been acknowledged as an important instrument in the health-state monitoring and the diagnosis of faults of power transformer. The principal benefit of using ratios techniques is that only ratios of gases are needed in the computation process, therefore, the oil quantity that is participated in gas dissolution is not needed. On the other hand, the downside is that they struggle to cover all dissolved gas analysis data set ranges. Each traditional method has their own limitations generally no decision or false decision as found in this work.

Artificial neural network is proposed as a solution and is then used to solve this inconvenience and treat cases not identified by classical techniques in order to an almost reliable diagnosis. The majority of limitations has been removed and the diagnostic results has been improved, the findings obtained through artificial neural network are extremely reliable compared to the traditional methods, where for IEC method the accuracy has been increased for 20 % to 70 % and from 40 % to 70 % for Roger method. However, in some sample, all methods either based artificial neural network or traditional are misleading and give a false diagnosis, so, the health of power transformer is vulnerable. Finally, as conclusion this improved results need more performed by more effective method such as deep learning.

Conflict of interest. The authors declare that they have no conflicts of interest.

REFERENCES

1. Li Z., Jiao Z., He A. Knowledge-based artificial neural network for power transformer protection. *IET Generation, Transmission & Distribution*, 2020, vol. 14, no. 24, pp. 5782-5791. doi: https://doi.org/10.1049/iet-gtd.2020.0542.

2. Rozov V.Yu., Kundius K.D., Pelevin D.Ye. Active shielding of external magnetic field of built-in transformer substations. *Electrical Engineering & Electromechanics*, 2020, no. 3, pp. 24-30. doi: https://doi.org/10.20998/2074-272x.2020.3.04.

3. Bouchaoui L., Hemsas K.E., Benlahneche S.E. *Diagnostic des transformateurs de puissance*. France, Omniscriptum Publ., 2018. 210 p. (Fra).

4. Bondarenko V.E., Shutenko O.V. Development of fuzzy neural network for the interpretation of the results of dissolved in oil gases analysis. *Electrical Engineering & Electromechanics*, 2017, no. 2, pp. 49-56. doi: https://doi.org/10.20998/2074-272x.2017.2.08.

5. Nizhevskyi I.V., Nizhevskyi V.I. Calculation estimation of overvoltage on insulation of the equipment of a substation at the lightning strike in its lightning arrester. *Electrical Engineering & Electromechanics*, 2019, no.3, pp. 67-73. doi: https://doi.org/10.20998/2074-272x.2019.3.11.

6. Faiz J., Soleimani M. Dissolved gas analysis evaluation in electric power transformers using conventional methods a review. *IEEE Transactions on Dielectrics and Electrical Insulation*, 2017, vol. 24, no. 2, pp. 1239-1248. doi: https://doi.org/10.1109/tdei.2017.005959.

7. Castro A.R.G., Miranda V. An interpretation of neural networks as inference engines with application to transformer failure diagnosis. *International Journal of Electrical Power & Energy Systems*, 2005, vol. 27, no. 9-10, pp. 620-626. doi: https://doi.org/10.1016/j.ijepes.2005.08.002.

8. Wani S.A., Khan S.A., Prashal G., Gupta D. Smart diagnosis of incipient faults using dissolved gas analysis-based fault interpretation matrix (FIM). *Arabian Journal for Science and Engineering*, 2019, vol. 44, no. 8, pp. 6977-6985. doi: https://doi.org/10.1007/s13369-019-03739-4.

9. Faiz J., Soleimani M. Assessment of computational intelligence and conventional dissolved gas analysis methods for transformer fault diagnosis. *IEEE Transactions on Dielectrics and Electrical Insulation*, 2018, vol. 25, no. 5, pp. 1798-1806. doi: https://doi.org/10.1109/TDEI.2018.007191.

10. Kaur A., Brar Y.S., Leena G. Fault detection in power transformers using random neural networks. *International Journal of Electrical and Computer Engineering*, 2019, vol. 9, no. 1, pp. 78-84. doi: https://doi.org/10.11591/ijece.v9i1.pp78-84.

11. Zhang Y., Ding X., Liu Y., Griffin P.J. An artificial neural network approach to transformer fault diagnosis. *IEEE Transactions on Power Delivery*, 1996, vol. 11, no. 4, pp. 1836-1841. doi: https://doi.org/10.1109/61.544265.

12. IEEE Guide for the Interpretation of Gases Generated in Mineral Oil-Immersed Transformers. *IEEE Std C57.104-2019* (Revision of IEEE Std C57.104-2008), 2019, 98 p. doi: https://doi.org/10.1109/IEEESTD.2019.8890040.

13. Bouchaoui L. *Diagnostic des transformateurs de puissance par la méthode d'analyse des gas dissous : application des réseaux de neurones*. Algeria, Université Ferhat Abbas Sétif 1 Publ., 2010. 155 p. (Fra). Available at: https://mmagister.univ-setif.dz/images/facultes/TEC/2010/BOUCHAOUI%20Lahcene.pdf (accessed 20 July 2020).

14. Fofana I. *Power transformer diagnostics, monitoring and design features*. Switzerland, MDPI Publ., 2018. 254 p. Available at: https://www.mdpi.com/books/pdfview/book/1073 (accessed 20 July 2020).

15. Paul D., Sen P., Goswami A.K. A probabilistic approach of fault detection through dissolved gas analysis in transformer and reactor. *2020 IEEE International Conference on Power Electronics, Smart Grid and Renewable Energy (PESGRE2020)*, 2020, pp. 1-6. doi: https://doi.org/10.1109/pesgre45664.2020.9070495.

16. Taha I.B.M., Mansour D.-E.A., Ghoneim S.S.M., Elkalashy N.I. Conditional probability-based interpretation of dissolved gas analysis for transformer incipient faults. *IET Generation, Transmission & Distribution*, 2017, vol. 11, no. 4, pp. 943-951. doi: https://doi.org/10.1049/iet-gtd.2016.0886.

17. Illias H.A., Chai X.R., Abu Bakar A.H., Mokhlis H. Transformer incipient fault prediction using combined artificial neural network and various particle swarm optimisation techniques. *PLOS ONE*, 2015, vol. 10, no. 6, p. e0129363. doi: https://doi.org/10.1371/journal.pone.0129363.
18. Zhang W., Yang X., Deng Y., Li A. An inspired machine-learning algorithm with a hybrid whale optimization for power transformer PHM. *Energies*, 2020, vol. 13, no. 12, p. 3143. doi: https://doi.org/10.3390/en13123143.
19. Enriquez A.R.S., Lima S.L., Saavedra O.R. K-NN and mean-shift algorithm applied in fault diagnosis in power transformers by DGA. *2019 20th International Conference on Intelligent System Application to Power Systems (ISAP)*, 2019, pp. 1-6. doi: https://doi.org/10.1109/isap48318.2019.9065948.
20. Cover T., Hart P. Nearest neighbor pattern classification. *IEEE Transactions on Information Theory*, 1967, vol. 13, no. 1, pp. 21-27. doi: https://doi.org/10.1109/TIT.1967.1053964.
21. Seifeddine S., Khmais B., Abdelkader C. Power transformer fault diagnosis based on dissolved gas analysis by artificial neural network. *2012 First International Conference on Renewable Energies and Vehicular Technology*, 2012, pp. 230-236. doi: https://doi.org/10.1109/revet.2012.6195276.
22. Jasim S.Y., Shrivastava J. Dissolved gas analysis of power transformers. *International Journal of Electrical and Electronics Engineering Research (IJEEER)*, 2013, vol. 3, no. 5, pp. 1-10.
23. Taecharoen P., Kunagonniyomrattana P., Chotigo S. Development of Dissolved Gas Analysis Analyzing Program using Visual Studio Program. *2019 IEEE PES GTD Grand International Conference and Exposition Asia (GTD Asia)*, 2019, pp. 785-790. doi: https://doi.org/10.1109/gtdasia.2019.8715892.
24. Wang Z., Liu Y., Griffin P.J. A combined ANN and expert system tool for transformer fault diagnosis. *IEEE Transactions on Power Delivery*, 1998, vol. 13, no. 4, pp. 1224-1229. doi: https://doi.org/10.1109/61.714488.
25. Rogers R.R. IEEE and IEC Codes to Interpret Incipient Faults in Transformers, Using Gas in Oil Analysis. *IEEE Transactions on Electrical Insulation*, 1978, vol. EI-13, no. 5, pp. 349-354. doi: https://doi.org/10.1109/TEI.1978.298141.
26. *IEC 60599:2015. Mineral oil-filled electrical equipment in service – Guidance on the interpretation of dissolved and free gases analysis*. 2015. Available at: https://webstore.iec.ch/publication/23323 (accessed 20 July 2020).
27. Mellah H., Hemsas K.E., Taleb R., Cecati C. Estimation of speed, armature temperature and resistance in brushed DC machines using a CFNN based on BFGS BP. *Turkish Journal of Electrical Engineering & Computer Sciences*, 2018, vol. 26, no. 6, pp. 3181-3191. doi: https://doi.org/10.3906/elk-1711-330.
28. Da Silva I.N., de Souza A.N., Hossri R.M.C., Hossri J.H.C. Intelligent system applied in diagnosis of transformer oil. *2000 Eighth International Conference on Dielectric Materials, Measurements and Applications* (IEE Conf. Publ. No. 473), 2000, pp. 330-334. doi: https://doi.org/10.1049/cp:20000528.
29. Mellah, H., Hemsas, K., Taleb, R. Intelligent sensor based Bayesian neural network for combined parameters and states estimation of a brushed DC motor. *International Journal of Advanced Computer Science and Applications*, 2016, vol. 7, no. 7, pp. 230-235. doi: https://doi.org/10.14569/ijacsa.2016.070731.

Received 08.11.2020
Accepted 31.05.2021
Published 27.08.2021

Lahcene Bouchaoui [1], *PhD Student*,
Kamel Eddine Hemsas [1], *Full Professor*,
Hacene Mellah[2], *PhD*, *Associate Professor*,
Saadeddine Benlahneche [3], *Chief of Electricity Transmission*,
[1] Electrical Engineering Department,
University Ferhat Abbas Setif 1,
Setif, Algeria,
e-mail: bouchaoui.lahcene@gmail.com,
hemsas_ke_dz@univ-setif.dz,
[2] Electrical Engineering Department,
Bouira University,
Bouira, Algeria,
e-mail: has.mel@gmail.com (Corresponding author),
[3] GRTE /SONELGAZ,
Setif, Algeria,
e-mail: benlahneche.saadeddine@grte.dz

How to cite this article:
Bouchaoui L., Hemsas K.E., Mellah H., Benlahneche S. Power transformer faults diagnosis using undestructive methods (Roger and IEC) and artificial neural network for dissolved gas analysis applied on the functional transformer in the Algerian north-eastern: a comparative study. *Electrical Engineering & Electromechanics*, 2021, no. 4, pp. 3-11. doi: https://doi.org/10.20998/2074-272X.2021.4.01.

UDC 621.313: 621.92: 537.8 https://doi.org/10.20998/2074-272X.2021.4.02

V.I. Milykh, M.G. Tymin

A COMPARATIVE ANALYSIS OF THE PARAMETERS OF A ROTATING MAGNETIC FIELD INDUCTOR WHEN USING CONCENTRIC AND LOOP WINDINGS

Introduction. *Three-phase inductors of a rotating magnetic field are used in grinders, separators and stirrers for the technological processing of bulk and liquid substances. This occurs in a cylindrical working chamber under the influence of ferromagnetic elements in the form of pieces of iron wire, which move together with the field.* ***Problem.*** *By analogy with three-phase induction motors, for the stator of inductors a concentric winding is adopted, which is a diametric single-layer winding. When moving from such motors to an inductor, its operating conditions have changed due to the significantly increased non-magnetic space inside the inductor compared to the motor clearances. The difference in the frontal parts of the phase windings has become essential for the electromagnetic parameters and the structure of the magnetic field in the inductor working chamber. Therefore, a loop shortened stator winding, which is symmetrical, can be considered as an alternative to a concentric diametric winding.* ***Goal.*** *The aim of the work is to compare the dimensional and electromagnetic parameters of a rotating magnetic field inductor in two versions of its three-phase winding: concentric single-layer diametrical and loop shortened two-layer.* ***Methodology.*** *Comparison of the windings is carried out through a detailed analysis of the geometrical parameters of their frontal parts, as well as through numerical-field calculations of the electromagnetic parameters of the inductor as a whole and the distribution of the magnetic field in its working chamber.* ***Results.*** *A significant difference in the geometrical parameters of the frontal parts of the two windings under inductor conditions was revealed. The loop version of the winding makes it possible to reduce the length of the winding conductor, its active resistance, as well as the reactance of its frontal dissipation. At the same time the asymmetry of the phase windings is excluded and an increase in the homogeneity of the magnetic field in the inductor working chamber is provided.* ***Originality.*** *The scientific novelty of the work lies in the development of a method of comparative analysis of the windings under the conditions of the rotating magnetic field inductor and in revealing the advantages of a loop shortened winding compared to the used concentric diametric winding.* ***Practical value.*** *The loop shortened stator winding recommended for the inductor will eliminate the asymmetry of its electromagnetic system. Thereby, the quality of its work in the technological processing of different substances is significantly increased due to ensuring the homogeneity of the magnetic field in the working chamber. At the same time, the copper conductor of the winding is still saved, and the efficiency of the inductor is also increased by reducing the power of electrical losses.* References 12, tables 5, figures 12.

Key words: **rotating magnetic field inductor, stator winding versions, geometrical and electromagnetic parameters.**

Розглянутий трифазний індуктор обертового магнітного поля для технологічної обробки різних речовин. Виконаний аналіз переваг і недоліків петльової укороченої обмотки його статора, яка пропонується як альтернатива використовуваної концентричної діаметральної обмотки. Порівняння обмоток проводиться за допомогою детального аналізу геометричних параметром їх лобових частин, а також електромагнітних параметрів індуктора в цілому за допомогою чисельно-польових розрахунків. Виявлено, що петльовий варіант дозволяє зменшити активний і реактивний опори лобового розсіяння обмотки і, що найсуттєвіше, виключити несиметрію фазних обмоток, забезпечуючи підвищення однорідності магнітного поля в робочій камері індуктора. Бібл. 12, табл. 5, рис. 12.

Ключові слова: **індуктор обертового магнітного поля, варіанти обмотки статора, геометричні і електромагнітні параметри.**

Рассмотрен трехфазный индуктор вращающегося магнитного поля для технологической обработки разных веществ. Выполнен анализ преимуществ и недостатков петлевой укороченной обмотки его статора, которая предлагается как альтернатива используемой концентрической диаметральной обмотки. Сравнение обмоток проводится посредством детального анализа геометрических параметром их лобовых частей, а также электромагнитных параметров индуктора в целом посредством численно-полевых расчетов. Выявлено, что петлевой вариант позволяет уменьшить активное и реактивное сопротивления лобового рассеяния обмотки и, что наиболее существенно, исключить несимметрию фазных обмоток, обеспечивая повышение однородности магнитного поля в рабочей камере индуктора. Библ. 12, табл. 5, рис. 12.

Ключевые слова: **индуктор вращающегося магнитного поля, варианты обмотки статора, геометрические и электромагнитные параметры.**

Introduction. Technological processing of various materials in grinders, separators and mixers is carried out using a magnetic field [1-8]. Including bulk and liquid substances are processed in inductors of a rotating magnetic field (IRMF) – electromagnetic mills [3, 4, 6-8]. This occurs under the influence of ferromagnetic elements (FEs) in the form of pieces of iron wire in a cylindrical working chamber, through which in the axial direction the processed substance is passed. Such elements move with a magnetic field, creating a so-called «vortex layer» in the chamber.

Initially, the inductors had a ferromagnetic core with three explicit poles, which housed the coils of a three-phase AC system [1]. This inductor design was replaced by an implicit-pole electromagnetic system similar to the stator of three-phase induction motors (TIM).

The energy level and dimensions of the inductors which are developed and operated correspond to the TIM with power of the order of units and tens of kilowatts. Therefore, taking into account the experience of their creation and operation [9], for inductors a fairly simple three-phase concentric diametric single-layer winding is adopted.

However, during the transition from TIM to the inductor, the conditions of its operation have changed

significantly due to the fact that the non-magnetic space inside the inductor has increased by two orders of magnitude compared to the gaps of the motor. If earlier the voltage drop across the active resistance and reactive resistance of the frontal scattering of the phase windings were units of percent of the electromotive force (EMF) on the active length of the machine, then in the inductor they are already commensurate. Under such conditions, the asymmetry of the frontal parts of the phase windings, which is inherent in the specified concentric winding, becomes significant. Also unfavorable is the pronounced «stepwise» distribution of the magnetomotive force (MMF) of the three-phase diametrical winding along the line of the boring circle of the stator core.

The theory of electric machines shows that a three-phase loop shortened winding, which is two-layer is deprived of these shortcomings [9]. However, for technological reasons, such a winding is considered acceptable in TIMs only as their power and dimensions increase.

The feasibility of using a loop winding in the IRMF instead of concentric one can be identified by comparing them in its conditions. The adequacy of this comparison has recently increased due to the development of methods for calculating electromagnetic parameters and characteristics of the inductor based on numerical calculations of magnetic fields [10, 11].

The goal of this work is to compare the dimensional and electromagnetic parameters of the inductor of a rotating magnetic field with two variants of its three-phase winding: concentric single-layer diametrical and loop shortened two-layer.

Object of study. The three-phase inductor is bipolar. Its electromagnetic system is given by its cross section in Fig. 1. The geometric parameters of the inductor are due to given for technological reasons the active length l_a = 250 mm and the radius of the inner surface r_{ki} = 47 mm of the working chamber at the average value of the magnetic flux density in it B_{av} = 0.12 T. This is due to the axial length of the stator core l_s, which is equal to l_a, the radii of its boring r_{si} = 0.06 m and the outer surface r_{si} = 0.109 m.

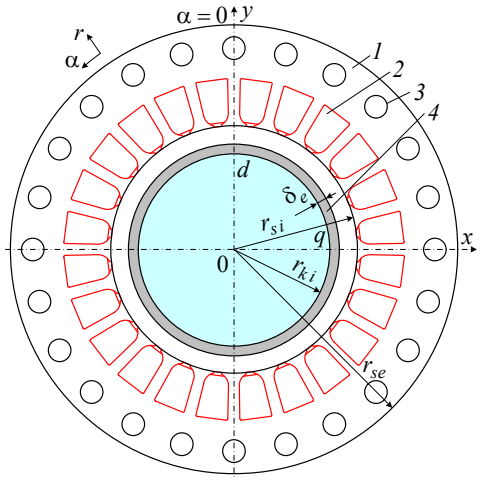

Fig. 1. Cross section of the IRMF electromagnetic system: *1* – laminated ferromagnetic core; *2* – slots with winding; *3* – ventilation ducts; *4* – shell of the working chamber

The core is made of electrical steel grade 2212 with thickness of 0.5 mm and has filling factor K_{Fe} = 0.95. The connection scheme of the winding is «star», and its phase has N_s = 72 turns. The shell of the chamber is δ_e = 5 mm thick and is made of non-magnetic stainless steel.

The inductor with the listed parameters was investigated in [11], where the calculation revealed the rated phase voltage of the stator winding U_{sN} = 100 V at frequency f_s = 50 Hz, but there another problem has been considered.

The structures of the compared variants of the winding – concentric diametric and loop shortened are given in Fig. 2, 3, where τ_p is the pole step. And for the second of them the coefficient of relative shortening β_s = 10/12 is chosen.

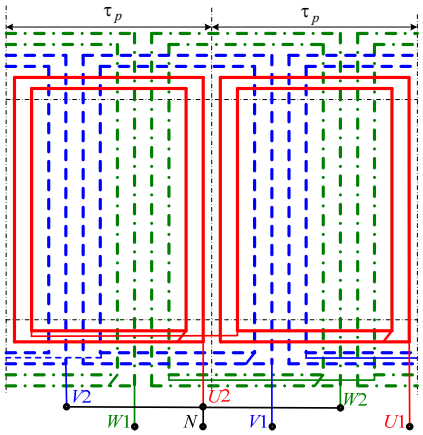

Fig. 2. Three-phase two-pole concentric single-layer stator winding

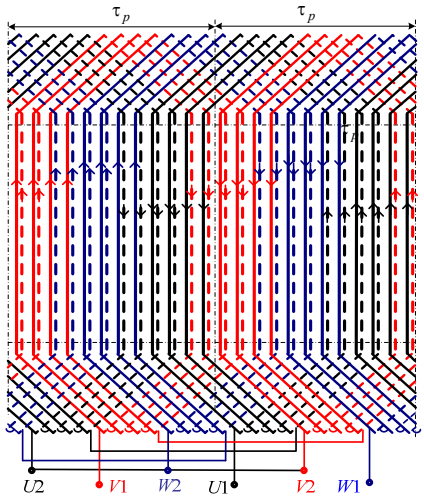

Fig. 3. Three-phase two-pole loop two-layer with shortened step stator winding

The distribution of phase windings in the slots of the stator is shown in Fig. 4, 5 in cross section of the electromagnetic system of the inductor.

In the example in Fig. 4 in the working chamber there are no FEs, and this corresponds to the ideal idle (II). In Fig. 5 the chamber is filled with FEs, which are oriented along the *y*-axis, and the magnetic field is rotated by the angle Θ, which is, as considered in [10], the load angle in the corresponding mode of operation of the inductor.

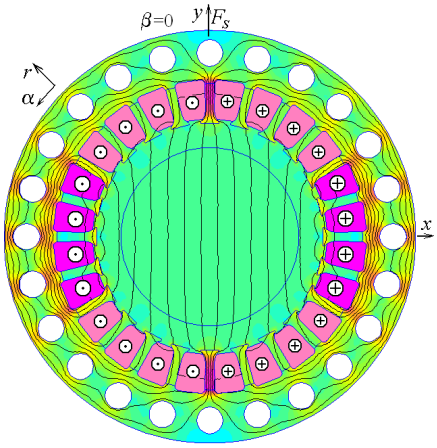

Fig. 4. Structure of the single-layer diametric winding and the magnetic field in the ideal idle mode

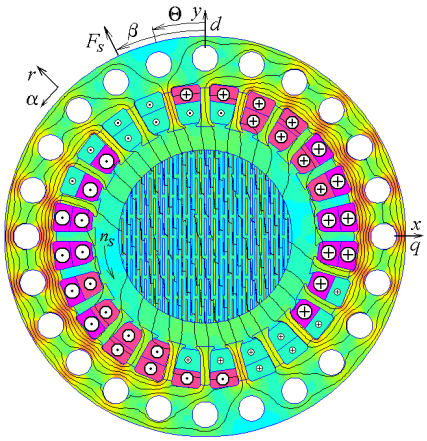

Fig. 5. Structure of the two-layer shortened winding and the magnetic field in rated load mode

The structure shown with a uniform distribution of FEs in the working chamber is idealized, as in [1, 10, 11], and it is required for an accessible organization of calculations. The real structure of the elements is usually less ordered.

FEs are made of steel St3. Their sizes and intervals between them are taken as in [11], which can be understood in Fig. 5, where everything is depicted on a single scale. An important parameter is the fill factor of the chamber with them in the *xy*-plane K_{Fes}, which is 0.32. The same coefficient is taken in the *yz*-plane: then the volume fill factor K_{Fev} has a value of 0.1.

For the winding options considered in Fig. 4, 5, the operating modes can be changed, but in general the pictures of the magnetic field are almost preserved.

In the cross section of the IRMF (see Fig. 1), the magnetic field is considered plane-parallel [10]. Therefore round sections of FEs are replaced by square ones with the corresponding recalculations of the sizes.

Fundamentals of numerical field calculations. The source of the rotating magnetic field in the inductor is a three-phase system of currents of the phase windings:

$$\begin{aligned} i_A &= I_m\cos(\omega_s t+\beta);\\ i_B &= I_m\cos(\omega_s t-2\pi/3+\beta);\\ i_C &= I_m\cos(\omega_s t+2\pi/3+\beta), \end{aligned} \qquad (1)$$

where t is the time; I_m is the current amplitude; ω_s is the angular frequency; β is the initial phase of the currents, which sets the required for a particular mode of calculation angular displacement of the direction of the MMF of the stator winding F_s directed by the *y*-axis.

An example of this is shown in Fig. 5, where β=26.7°. Figure 4 shows the directions of currents in the phase windings in the II mode, in which β=0, and therefore the vector of the MMF F_s is directed along the *y*-axis.

The magnetic field of the inductor in its central cross section is described by the well-known 2D differential equation [10, 12]:

$$\mathrm{rot}[\mu_a^{-1}\mathrm{rot}(\vec{k}A_z)] = \vec{k}J_z\,, \qquad (2)$$

where μ_a is the absolute magnetic permeability; $\vec{k}$ is the unit vector along the axial *z*-axis; A_z, J_z are the components of the magnetic vector potential and current density.

The propagation of the magnetic field is limited by the Dirichlet boundary condition A_z = 0 on the outer surface of the core. The effect of the camera shell on the magnetic field is considered insignificant.

The provided research tools are numerical calculations of the magnetic field by the Finite Element Method according to the FEMM computer code [12] with control by the created Lua script. In general, the method of calculating the magnetic fields of the inductor and its electromagnetic parameters, as well as the rationale for the accepted assumptions are described in detail in [10, 11], so in this work this is not repeated.

The voltage equilibrium in the phase winding of the stator corresponds to the complex equation [10]:

$$\underline{U}_s = -\underline{E}_a + jX_v\underline{I}_s + (R_s + R_{mag})\underline{I}_s\,, \qquad (3)$$

where the complexes of its current $\underline{I}_s$ and EMF $\underline{E}_a$, which is created on the active length of the winding, are presented.

Formula (3) also includes the active resistance R_s and the reactive resistance of the frontal scattering X_v of the phase winding, as well as the active resistance R_{mag}, which reflects the power of the magnetic losses and is determined during the iterative calculation of the magnetic field [10].

Comparative calculations of geometric parameters of winding variants in the inductor. Figures 4, 5 already show the accepted shape of the semi-closed slot of the inductor, which is trapezoidal with rounding, which is characteristic of induction motors of the same size.

Figure 6 shows the structure of the insulation of the slot, which for the two-layer winding is supplemented by a jumper. Detailed calculations show that in the case of a single-layer winding, the useful cross-sectional area of the slot remaining for the conductors, S_{sn}=274 mm^2, and in the case of a two-layer winding, it decreased by 4 mm^2 or 1.5 %.

For clarity of further illustrations for the winding, the adopted diameter of the uninsulated effective conductor d_{sc} = 3 mm, and of the insulated one is d_{scis} = 3.46 mm, and in the slot their number is z_{Qs} = 18. For technological reasons, the effective conductor can be divided into elementary conductors of smaller diameter.

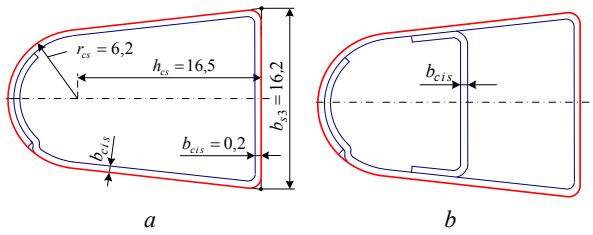

Fig. 6. Estimated model of the slot with insulation (b_{cis} – insulation thickness): *a* – with a single-layer winding, *b* – with a two-layer winding (dimensions in mm)

The main difference between the given variants of a winding consists in their frontal parts, and here the careful calculation analysis is applied.

The design of the frontal parts of the single-layer concentric winding is shown in Fig. 7 – in the longitudinal section of the inductor, as well as in Fig. 8 as a view of the ends of these parts.

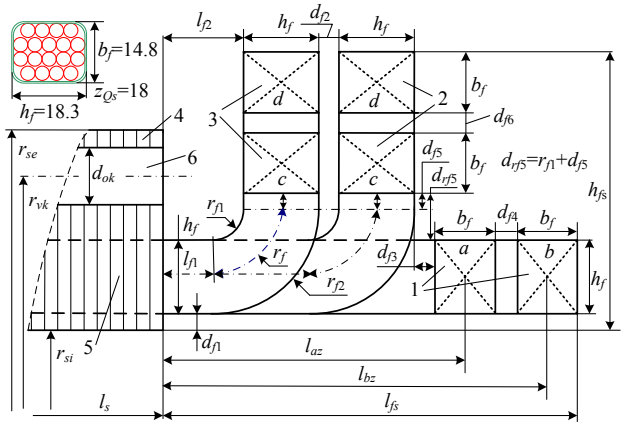

Fig. 7. Frontal part of the concentric winding in the meridian section: 1, 2, 3 – phase windings; 4 – surface of the core; 5 – slot with the winding rod; 6 – axial ventilation channel

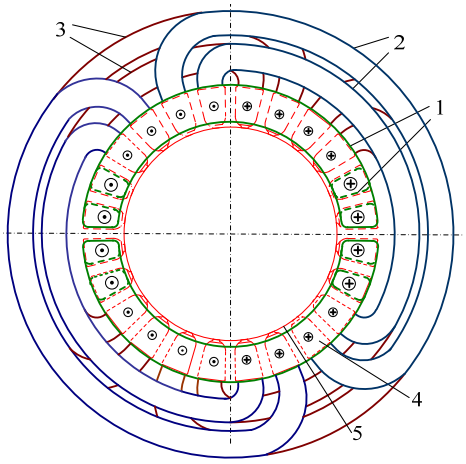

Fig. 8. Frontal part of the concentric winding (end view): 1, 2, 3 – phase windings; 4 – slot with the winding rod; 5 – core boring surface

The whole structure depends on the size of the «harness» of the conductors, which is formed in a rectangular section, and Fig. 7 shows its dimensions h_f and b_f (in mm) together with the surface insulation. The figure is shown in proportion, and all dimensions are marked on it without providing a number of values just to reveal the degree of detail of the calculations.

The design of the frontal parts of the two-layer loop winding is given in Fig. 9, where two sections are left from a flat scan (see Fig. 3), as well as a view in longitudinal section of the inductor (right). Here, one harness contains half the number z_{Qs}, i.e. 9 conductors, and its dimensions h_f and b_f together with the insulation were 11 mm. In Fig. 9, as in Fig. 7 the proportions of the sizes are saved, but all set of their designations is shown for display of a measure of detailing of calculations.

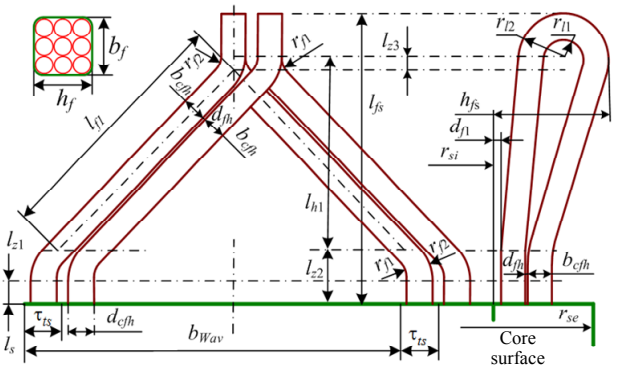

Fig. 9. Calculation model of the frontal part of the loop two-layer winding with indication of the size of its elements

The frontal parts of the windings are sparse, gaps are provided between them. This is necessary in conditions of high current density in the winding and a complicated cooling and ventilation system in the inductor compared to induction motors. Facilitation of cooling and ventilation is achieved by the introduction of axial ventilation ducts in the stator core, which is not practiced in induction motors of appropriate dimensions. However, the study of this issue is beyond the scope of this article and will be considered separately.

On the basis of calculation models of frontal parts of windings, detailed calculations of their sizes are carried out that allows to carry out their comparative analysis. First of all, Table 1 shows the basic geometrical parameters of two variants of the inductor winding (hereinafter 1*sl* – single-layer concentric diametrical; 2*sl* – two-layer shortened loop).

Table 1

Lengths of the elements of single- and double-layer windings

Version	h_{fs}	l_{fs}	l_{fhav}	l_{Wav}	l_{csav}
	mm	mm	mm	mm	m
1*sl*	70	103	460	1420	102
2*sl*	58	145	379	1259	91

The dimensions indicated in Table 1: h_{fs} – the farthest deviation of the winding from the boring core; l_{fs} – the outreach of the frontal part of the winding; l_{fhav} and l_{Wav} – the length of the wire of the frontal part and the coil of the average coil; l_{csav} – the length of the wire of the average phase winding.

The average length of the coil is the sum of the lengths of the rectilinear slot l_s and the curved frontal parts l_{fhaw} of the winding:

$$l_{Wav} = 2(l_s + l_{fhav}). \quad (4)$$

The total length of the conductors of the phase winding

$$l_{cs} = l_{Wav} N_s. \quad (5)$$

According to the indicators h_{fs} and l_{fs} (Fig. 7, 9), which affect the dimensions of the inductor, the windings have both advantages and disadvantages, but in terms of the volume $h_{fs}\times l_{fs}$ the double-layer winding loses by 17 %, although in the total volume of the inductor it will have a much smaller share. But the gain in diameter through h_{fs} has priority over the loss in axial length through l_{fs}.

The structure of the sections of the loop winding (see Fig. 3) is always symmetrical. The concentric winding has six different variants of the coils (Fig. 2), and their asymmetry (see Fig. 7) occurs due to different lengths of the wire of the frontal parts l_{favh}. But for comparison in Table 1 the lengths l_{fhav} and l_{Wav} of the average coil are taken. As a result, the loop winding has the advantage of a shorter wire length l_{cs} of the phase winding by 12 %. In addition to saving copper, this helps to reduce the active and reactive resistance of this winding.

However, the disadvantages of the concentric winding are manifested not only in this, but also in the asymmetry of the phase windings as a whole due to the difference of their individual coils, which is explained in Table 2. Here the calculated dimensions of the elements of this winding are indicated: l_{fhawk}, l_{Wavk} – the average lengths of the frontal parts and individual coils; l_{Wavf}, l_{csf} – the average lengths of turns and all wire of phase windings, and the made designations of versions of coils correspond to Fig. 7: 1, 2, 3 – the number of phase winding; *a*, *b*, *c*, *d* – the version of its coil.

Table 2

Lengths of the elements of the concentric winding

Version	1*a*	1*b*	2*c*	2*d*	3*c*	3*d*
l_{fhawk}, mm	324	402	429	635	382	589
l_{Wavk}, mm	1149	1305	1357	1770	1264	1677
l_{Wavf}, m	1227		1564		1471	
l_{csf}, m	88		113		106	

Manifestation of asymmetry is the difference of the largest and smallest sizes: l_{fhawk} by 96 %, l_{Wavk} by 54 %, l_{Wavf} and l_{csf} by 28 %, and the reason for this is the frontal parts of the phase windings.

For low and medium power machines for practical calculations empirical formulas that take into account the main features of the design forms of the coils are used [9]. For the coil of the bulk concentric winding of the stator, the following winding lengths are obtained: l_{cs} = 80.3 m; l_{Wav} = 1115 mm; l_{fh} = 307 mm; l_{fs} = 75.2 mm. It is seen that the classical technique, in comparison with the developed method, gives significantly underestimated parameters of the windings l_{cs} and l_{Wav} – by 21 %; l_{fh} – by 33 %; l_{fs} – by 27 %. That is, the classical approximate technique does not take into account the features of the stator winding of this inductor.

For a two-layer loop shortened winding the classical technique according to the corresponding formulas gives lengths: l_{fh} = 302 mm, l_{fs} = 97.5 mm, l_{Wav} = 1104 mm, l_{cs} = 79.5 m, which differs from the developed refined method by 20.3 %, 32.8 %, 12.6 % and 12.3 %, respectively.

Stator phase winding resistances. The calculated geometric parameters of the windings allow to determine their active resistances and reactive resistances of the frontal scattering included in (3). Reactive scattering resistances on the active length of the winding are automatically taken into account in the EMF E_a, which is determined by calculating the magnetic field at this length.

Active electrical resistance of the phase winding, reduced to the accepted operating temperature T_w = 115 °C:

$$R_s = k_r\, k_{T\,Cu}\,\frac{\rho_{Cu\,Tb}\; l_{cs}}{S_{s\,c}}, \qquad (6)$$

where S_{cs} is the cross section of the effective conductor, m^2; ρ_{Tb} = 1.75 10^{-8} Ω·m is the resistivity of copper winding at base temperature T_b = 20 °C; $k_{TbCu} = 1+\alpha_T\cdot(T_w - T_b)$ is the temperature coefficient of resistance (k_{TbCu}=1,38); α_T = 0.004 °C^{-1} is the specific temperature coefficient of resistance of copper; k_r is the coefficient of increase of resistance due to current displacement (following [9], k_r = 1).

Inductive resistance of the frontal scattering of the phase winding of the stator is determined by the classical method [9], which is common to given types of winding:

$$X_v = 1{,}58\cdot\frac{f_s\, l_s\, N_s^2\, \lambda_{\sigma\, fh}}{p\; q_s\, 10^8}, \qquad (7)$$

where the scattering conductivity factor of the frontal parts of the stator winding

$$\lambda_{s\,fh} = 0{,}34\,\frac{q_s}{l_s}\left(l_{fh} - 0{,}64\beta_s\,\tau_p\right); \qquad (8)$$

where q_s is the number of slots per pole and phase.

Comparison of resistances (p.u.) of single-layer (1*sl*) and double-layer (2*sl*) windings are given in Table 3. The advantage of the second of them in terms of resistance is obvious: active resistance is 11 % lower, reactive resistance of frontal scattering is lower by 18 %. When calculating for a concentric winding, its parameters are taken as average, accordingly, the parameters in Table 3 are averaged.

Table 3

Electrical parameters of windings

Version	R_s	$\lambda_{s\,fh}$	X_v	I_s	E_a	U_v	U_R
	Ω	p.u.	Ω	A	V	V	V
1*sl*	0,349	1,847	0,473	59,9	69,4	28,3	21,6
2*sl*	0,310	1,516	0,378	66,5	72,0	25,1	21,4

The conditional active resistance R_{mag} included in (3) depends on the load level of the inductor and is in the range 0.01–0.014 Ω.

Analysis of the electromagnetic parameters of the inductor in the ideal idle mode. The initial calculations of the electromagnetic parameters of the inductor are performed in the II mode, the essence of which is the absence of ferromagnetic elements in the working chamber. It is for this mode that the required value of the magnetic flux density B_{av} in this chamber is set, and it is the most intense in terms of the stator winding current that given in [11].

At rated voltage U_{sN}, the effective values of current I_s, EMF E_a and voltage drops $U_v = X_v I_s$ and $U_R = (R_s+R_{mag})I_s$ have the values shown in Table 3. There is a significant effect on the equilibrium of voltages of their drops, which leave for the main EMF about 70 % of

the input voltage, while, for example, in induction motors it reaches more than 95 %.

Electrical and energy parameters of the inductor for the two versions of the winding in the II mode are given in Table 4, where P_{els}, P_{mags} – the power of electric and magnetic losses; J_{sc} – the current density in the conductor; A_s – the linear current load on the core boring.

Table 4

Comparison of electrical and energy inductor parameters when using different windings

Version	P_{els}	P_{mags}	B_{av}	J_{sc}	A_s
	W	W	T	A/mm^2	A/cm
1*sl*	3760	43	0,117	8,48	687
2*sl*	4100	41	0,125	9,40	761

Graphs of distribution of the module of the magnetic flux density B in the core of the inductor are given in Fig. 10, 11. They correspond to the II for a symmetric current system with the values in Table 3 (for a concentric winding it is conditional with averaging of phase windings).

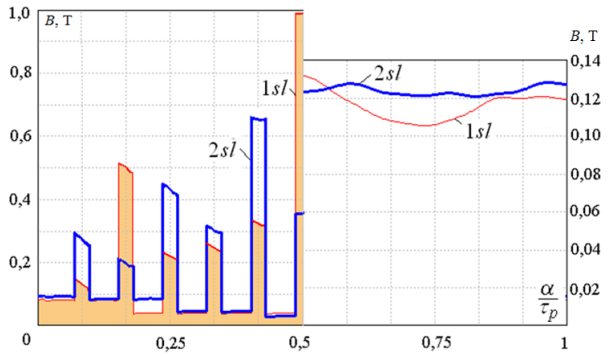

Fig. 10. Distribution of the magnetic flux density along the pole arc (left – on the average radius along the height of the tooth, right – on the surface of the working chamber)

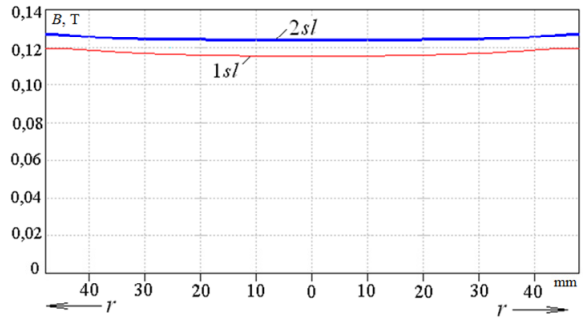

Fig. 11. Distribution of the magnetic flux density along the horizontal central axis within the working chamber

The graphs show that from the point of view of uniformity of distribution of the magnetic flux density the loop shortened winding has an advantage, besides it gives slightly more value of the magnetic flux density in the working chamber. And the nonuniform distribution in both cases is caused by the discrete structure of the stator winding.

If we consider the individual phase windings, then in its loop version, symmetry is its essence. Consequently, in the case of a concentric winding, due to differences in the parameters of the phase windings (see Table 2), there is a significant asymmetry of the phase currents and other electrical quantities. And this leads to known problems, the basis of the analysis of which is the following approximate method.

The reactive resistance of the slot part of the winding $X_a = E_a/I_s$ is introduced, which was 1.159 Ω and essentially takes into account the mutual inductive resistances of all phases, because the phase EMF E_a was determined by the magnetic field of the entire three-phase winding.

The difference in the parameters of the three windings arose due to the different lengths of their frontal parts, given in Table. 5. Therefore, there are active R_s and reactive X_v resistance, which are shown in the same table.

Table 5

Comparison of inductor phase parameters for concentric winding

Phase winding	l_{fh}	X_v	R_s	Z_s	I_s
	mm	Ω	Ω	Ω	A
1	363	0,473	0,275	1,529	65,30
2	532	0,573	0,403	1,776	56,16
3	486	0,508	0,368	1,708	58,55
av	460	0,473	0,349	1,671	59,85

To eliminate the «skew» of the phase voltages, the concentric winding is fed by a «star» circuit with a neutral wire N (Fig. 2). Then the separate impedance for each phase

$$Z_s = \sqrt{(R_s + R_{mag})^2 + (X_a + X_v)^2} \qquad (9)$$

and the phase current $I_s = U_s/Z_s$ are calculated.

The obtained asymmetric current system is given in Table 5. In addition to the parameters of the numbered phase windings 1, 2, 3, it also presents the parameters of the averaged winding *av*.

The obtained effective values of phase currents are substituted in (1), and a number of calculations of the magnetic field when changing β from 0 to 180° with a step of 2° is carried out, which provided a simulation of the rotation of the magnetic field.

At each calculation point, the values of the magnetic flux density were determined at fixed points of the working chamber: 1 – in the center; 2, 3 – in the upper and right boundary points.

The results of calculations for the asymmetric concentric winding are given in Fig. 12 compared to similar graphs for a symmetrical loop winding. The graphs show the advantage of a loop winding, which provides almost stable magnetic flux density. With a concentric winding, there are significant pulsations of the magnetic flux density, because the asymmetric current system gives an elliptical magnetic field.

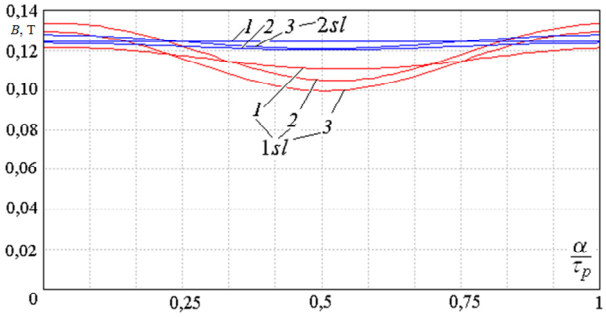

Fig. 12. Changes in the magnetic flux density at fixed points of the working chamber during the rotation of the magnetic field: 1 – in the center; 2, 3 – on the surface at the top and right

Conclusions.

1. The developed technique allows on the basis of a single approach to calculate the geometric parameters of the frontal parts of concentric and loop windings taking into account their detailed structure and size of all components, which gives much more accurate results compared to classical methods of designing electric machines.

2. In the conditions of the inductor of a magnetic field the role of frontal parts of windings appears much more essential, than in the conditions of classical AC machines. This is manifested in an increase of 5-6 times the relative contribution to the equation of equilibrium of the EMF and the voltage drops on the reactance of the frontal scattering, as well as on the active resistance of the windings.

3. An important advantage of the loop shortened winding compared to the concentric diametric winding is the shorter length of the frontal part conductor, which reduces the active resistance of the winding as a whole by 11 % and the reactance of the frontal scattering by 18 %.

4. The loop three-phase winding is symmetrical, while the concentric winding has a pronounced asymmetry due to differences in the parameters of its frontal parts, which leads to a significant deterioration of the electromagnetic parameters of the inductor as a whole.

5. Due to the peculiarities of the discrete phase structure of the concentric diametric winding and the asymmetry of its phase currents, the magnetic field in the working chamber of the inductor is unstable and less homogeneous compared to the loop shortened winding.

6. The advantages of the concentric winding include a slightly smaller particle size of the inductor in the area of its frontal parts, as well as less complex technology of manufacturing and laying in the slots of the core.

7. Further development of research should be the development of technology for the manufacture of loop shortened two-layer winding in the inductor conditions, the implementation of its relevant experimental studies, as well as improving the parameters of this winding by optimizing it.

Conflict of interest. The authors declare that they have no conflicts of interest.

REFERENCES

1. Logvinenko D.D., Sheljakov O.P. *Intensifikacija tehnologicheskih processov v apparatah s vihrevym sloem* [Intensification of technological processes in apparatus with a vortex layer]. Kiev, Tehnika Publ., 1976. 144 p. (Rus).

2. Belounis A., Mehasni R., Ouil M., Feliachi M., El-Hadi Latreche M. Design with optimization of a magnetic separator for turbulent flowing liquid purifying applications. *IEEE Transactions on Magnetics*, 2015, vol. 51, no. 8, pp. 1-8. doi: https://doi.org/10.1109/tmag.2015.2424401.

3. *Company GlobeCore. Vortex Layer Machine ABC-100.* Available at: https://avs.globecore.ru/products/avs-100.html (accessed 30 September 2017). (Rus).

4. Ogonowski S., Wołosiewicz-Głąb M., Ogonowski Z., Foszcz D., Pawełczyk M. Comparison of wet and dry grinding in electromagnetic mill. *Minerals*, 2018, vol. 8, no. 4, p. 138. doi: https://doi.org/10.3390/min8040138.

5. Wolosiewicz-Glab M., Ogonowski S., Foszcz D., Gawenda T. Assessment of classification with variable air flow for inertial classifier in dry grinding circuit with electromagnetic mill using partition curves. *Physicochemical Problems of Mineral Processing*, 2018, vol. 54, no. 2, pp. 440-447. doi: http://dx.doi.org/10.5277/ppmp1867.

6. Całus D., Makarchuk O. Analysis of interaction of forces of working elements in electromagnetic mill. *Przegląd Elektrotechniczny*, 2019, no. 12, pp. 64-69. doi: https://doi.org/10.15199/48.2019.12.12.

7. Shvedchykova I., Melkonova I., Romanchenko J. Research of magnetic field distribution in the working area of disk separator, taking into account an influence of materials of permanent magnets. *EUREKA: Physics and Engineering*, 2020, vol. 1, pp. 87-95. doi: https://doi.org/10.21303/2461-4262.2020.001106.

8. Makarchuk O., Calus D., Moroz V. Mathematical model to calculate the trajectories of electromagnetic mill operating elements. *Technical Electrodynamics*, 2021, no. 2, pp. 26-34. doi: https://doi.org/10.15407/techned2021.02.026.

9. Kopylov I.P., Klokov B.K., Morozkin V.P., Tokarev B.F. *Proektirovanie elektricheskih mashin* [The design of electrical machines]. Moscow, Yurait Publ., 2011. 767 p. (Rus). Available at: https://em.fea.kpi.ua/images/doc_stud/distsiplini/oapem2/kopilov_proektirovanie_em_2011.pdf (accessed 10 May 2021).

10. Milykh V.I., Shilkova L.V. Characteristics of a cylindrical inductor of a rotating magnetic field for technological purposes when it is powered from the mains at a given voltage. *Electrical Engineering & Electromechanics*, 2020, no. 2, pp. 13-19. doi: https://doi.org/10.20998/2074-272x.2020.2.02.

11. Milykh V.I., Shilkova L.V. Control current method of the concentration of ferromagnetic elements in the working chamber of the technological inductor of magnetic field during its operation. *Electrical Engineering & Electromechanics*, 2020, no. 5, pp. 12-17. doi: https://doi.org/10.20998/2074-272x.2020.5.02.

12. *Finite Element Method Magnetics: OldVersions.* FEMM 4.2 11Oct2010 Self-Installing Executable. Available at: http://www.femm.info/wiki/OldVersions (accessed 15 May 2021).

Received 15.05.2021
Accepted 20.06.2021
Published 27.08.2021

V.I. Milykh[1], *Doctor of Technical Science, Professor,*
M.G. Tymin[1], *Postgraduate Student,*
[1] National Technical University «Kharkiv Polytechnic Institute», 2, Kyrpychova Str., Kharkiv, 61002, Ukraine,
e-mail: mvikemkpi@gmail.com (Corresponding author),
gunter_odim@ukr.net

How to cite this article:
Milykh V.I., Tymin M.G. A comparative analysis of the parameters of a rotating magnetic field inductor when using concentric and loop windings. *Electrical Engineering & Electromechanics*, 2021, no. 4, pp. 12-18. doi: https://doi.org/10.20998/2074-272X.2021.4.02.

UDC 621.313.322 https://doi.org/10.20998/2074-272X.2021.4.03

V.V. Shevchenko, A.N. Minko, M. Dimov

IMPROVEMENT OF TURBOGENERATORS AS A TECHNICAL BASIS FOR ENSURING THE ENERGY INDEPENDENCE OF UKRAINE

The paper defines the directions of improving turbogenerators as the basis for ensuring the energy independence of Ukraine. The analysis of the state, problems and prospects for the development of modern electric power industry. ***Goal of the work*** *is to identify promising directions for sustainable development of the national electric power industry in order to ensure energy security of Ukraine, to conduct a comparative analysis of electricity sources, to confirm the need to improve the main sources – turbogenerators.* ***Methodology****. During the research, an analytical analysis of the electricity sources, which are installed at power plants in Ukraine and the world, was carried out, taking into account the growth of the planet's population and its energy activity. Cyclic theory was chosen as the theoretical basis for forecasting. On the basis of this theory, global development trends, advantages and disadvantages of currently used sources of electricity - thermal (including nuclear) power plants and stations that operate from renewable energy sources - have been established. A review of literary sources on the methods of the energy sector forecasting the development, including the development of the energy sector in Ukraine, has been carried out.* ***Originality****. It has been established that due to the active growth of the planet's population, with the increase in its energy activity, obtaining electricity from renewable energy sources is not enough, that for the next 20-30 years nuclear power plants will be the main sources of electricity. The internal and external threats to the energy security of Ukraine, directions of development of turbogenerator construction, ways to improve turbogenerators, to increase their energy efficiency, power per unit of performance, to increase the readiness and maneuverability factors, and overload capacity have been identified.* ***Practical significance****. The need to continue the modernization and improvement of the turbogenerators of nuclear power plant units, as the main sources of electricity, has been proved. The directions of their improvement are established: increasing the power in the established sizes, making changes to the design of the turbogenerators inactive elements, replacing the cooling agent to keep Ukrainian turbogenerators at the world level, improving auxiliary systems, improving and increasing the reliability of the excitation system, introduction of automatic systems for monitoring the state turbogenerators. Possible limits of use, advantages, disadvantages and problems of using renewable energy sources for Ukraine have been established.* References 43, tables 3, figures 5.

Key words: **electric power industry, energy independence, turbogenerator, energy saving, ecology, technical diagnostics, weight and size indicators, power increase, renewable energy sources.**

У статті проведено аналіз стану, проблем та перспектив розвитку сучасної електроенергетики. Визначено напрямки її розвитку з урахуванням вибору техніко-економічного сценарію розвитку, супутніх факторів і їх взаємного впливу. Метою роботи було визначення перспективних напрямків сталого розвитку національної електроенергетики щодо забезпечення енергетичної безпеки України, проведення порівняльного аналізу джерел електроенергії, підтвердження необхідності вдосконалення основних джерел – турбогенераторів. Визначено внутрішні та зовнішні загрози енергетичній безпеці України. Встановлено переваги і недоліки, світові тенденції подальшого використання сучасних джерел електроенергії - теплових (включаючи атомні) електростанцій і станцій від поновлюваних джерел енергії. Встановлено, що в зв'язку з активним ростом населення планети і зі збільшенням його енергетичної активності електроенергії від поновлюваних джерел енергії буде недостатньо, що найближчі 20-30 років основними джерелами електроенергії будуть атомні електростанції і це підтверджує необхідність проведення робіт по вдосконаленню турбогенераторів. Встановлені напрями вдосконалення конструкцій турбогенераторів і систем охолодження. Зазначено, що вдосконалення турбогенераторів вимагає одночасного підвищення ефективності і систем, що забезпечують їх роботу: систем постачання газом, водою і маслом, системи збудження. Показана необхідність повного впровадження автоматичного контролю стану турбогенераторів, використання прийомів сучасної технічної діагностики найбільш напружених вузлів і елементів як в режимі online, так і при проведенні планових і аварійних ремонтів. Підтвердження необхідності проведення робіт по вдосконаленню вітчизняних турбогенераторів викликано появою в загальній енергосистемі України нових типів електроенергетичних джерел, які користуються активною державною підтримкою. Відзначена перспективність використання поновлюваних джерел енергії з точки зору зниження екологічних проблем, але лише для індивідуальних споживачів. Проаналізовані переваги, недоліки і проблеми використання поновлюваних джерел енергії, які найбільш прийнятні для України. Бібл. 43, табл. 3, рис. 5.

Ключові слова: **електроенергетика, енергетична незалежність, турбогенератор, енергозбереження, екологія, технічна діагностика, масогабаритні показники, підвищення потужності, поновлювані джерела енергії.**

В статье проведен анализ состояния, проблем и перспектив развития современной электроэнергетики. Определены направления ее развития с учетом выбора технико-экономического сценария развития, сопутствующих факторов и их взаимного влияния. Целью работы являлось определение перспективных направлений устойчивого развития национальной электроэнергетики с целью обеспечения энергобезопасности Украины, проведение сравнительного анализа источников электроэнергии, подтверждение необходимости совершенствования основных источников – турбогенераторов. Установлены достоинства и недостатки, мировые тенденции дальнейшего использования современных источников электроэнергии – тепловых (включая атомные) электростанций и станций от возобновляемых источников энергии. Определены внутренние и внешние угрозы энергетической безопасности Украины. Установлено, что в связи с активным ростом населения планеты и с увеличением его энергетической активности электроэнергии от возобновляемых источников энергии будет недостаточно, что ближайшие 20-30 лет основными источниками электроэнергии будут атомные электростанции и это подтверждает необходимость проведения работ по совершенствованию турбогенераторов. Установлены направления совершенствования конструкций турбогенераторов и систем охлаждения.

Отмечено, что совершенствование турбогенераторов требует одновременного повышения эффективности и систем, обеспечивающих их работу: систем снабжения газом, водой и маслом, системы возбуждения. Показана необходимость полного внедрения автоматического контроля состояния турбогенераторов, использования приемов современной технической диагностики наиболее напряженных узлов и элементов как в режиме online, так и при проведении плановых и аварийных ремонтов. Подтверждение необходимости проведения работ по совершенствованию отечественных турбогенераторов вызвано появлением в общей энергосистеме Украины новых типов электроэнергетических источников, которые пользуются активной государственной поддержкой. Отмечена перспективность использования возобновляемых источников энергии с точки зрения снижения экологических проблем, но только для индивидуальных потребителей. Проанализированы преимущества, недостатки и проблемы использования возобновляемых источников энергии, которые наиболее приемлемы для Украины. Библ. 43, табл. 3, рис. 5.
Ключевые слова: **электроэнергетика, энергетическая независимость, турбогенератор, энергосбережение, экология, техническая диагностика, массогабаритные показатели, повышение мощности, возобновляемые источники энергии**

The following abbreviations are used in the work: **TG** – turbogenerator; **NPP** – nuclear power plant; **TPP** – thermal power plant; **CHP** – combined heat and power plant; **HPP** – hydroelectric power plant; **RES** – renewable energy sources; **WPP** – wind power plant; **OECD** – Member Countries of the Organization for Economic Co-operation and Development; **HTSC** – high-temperature superconductor; **LTSC** – low-temperature superconductor.

Introduction. In most countries of the world, the electric power industry is considered the most important sector of the national economy. Therefore, **the goal of this work** is to identify promising directions for sustainable development of the national electric power industry in order to ensure the energy security of Ukraine, conduct a comparative analysis of electricity sources and confirm the need to improve the main sources – turbogeneratots. Here, the main issue, one of the most serious problems for any national manufacturer, is energy saving [1-4]. The solution to the problem of energy saving is especially important for Ukraine, where at present the production of a unit of GDP on average consumes almost 3 times more energy resources than in European countries [1, 3, 5]. Energy saving is one of the most important factors contributing to an increase in the level of energy security, which is one of the most important elements of sustainable economic development for both exporting and importing countries of energy resources. Obviously, it is difficult to solve the problem of ensuring the energy security of the country if the energy supply is fully or largely dependent on external suppliers [3, 5]. For Ukraine, as well as for all countries, the main requirement when choosing directions for the development of the electric power industry is reliable and efficient energy supply to industry and the population, obligatory taking into account the requirements of environmental safety and social stability. The promising tasks of the energy sector are the same for all countries: it is the search for new sources and technologies for generating electricity, a continuous increase in generation volumes, an increase in efficiency in transmission and distribution, and a reduction in losses at all these stages [6-8].

When choosing directions for the development of the electric power industry, it is necessary to take into account the whole complex of factors and their mutual influence: the technical condition of electrical equipment, national directions and priorities for the joint development of the economy and industry; political, environmental, demographic problems; technological and resource capabilities not only of the electrical engineering industry, but also of related industries: turbine construction, enterprises for the creation of controlled reactors, mining and processing of uranium [5, 8].

At the present time it is necessary to choose: to continue the development of different directions or to develop one, specific direction; to improve and develop mono-energy with globalization on a national scale or to give priority to the development of poly-energy (mini- and micro-hydroelectric power plants, solar and wind energy, mini-CHP, etc.).

Since the end of the 90s of the 20th century in all countries, special attention (and government material support) has been paid to energy from RES, «green energy» [2, 5]. This is an important area, but it will not meet the growing needs of the world's population for electricity, which are constantly increasing, especially taking into account the continuous increase in specific energy consumption in all countries of the world (Fig. 1, Fig. 2, Table 1) [3, 9, 10].

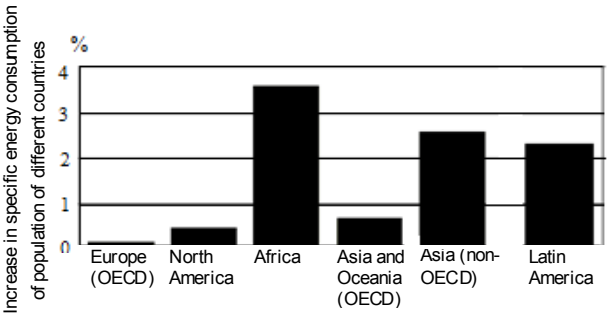

Fig. 1. Forecast of annual growth in electricity demand (specific energy consumption), 2010-2040

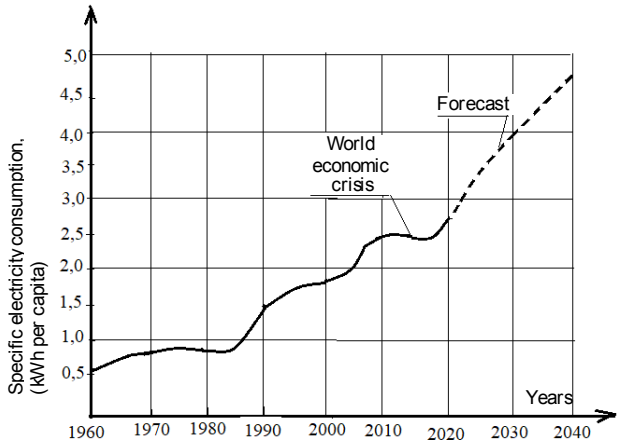

Fig. 2. Global growth in specific electricity consumption (kWh per capita)

Table 1

Existing and prospective population growth and demand for basic energy in 2030

No,	Indicator	World rates of population growth and demand for main types of energy, % to the level of 1970		
		1970-1990	1990-2010	2010-2030 (forecast)
1	Population	+1,8	+1,4	+1,0
2	GDP	+3,5	+3,2	+4,0
3	Electricity	+2,6	+3,2	+3,9
4	Electricity per capita	+0,5	+0,5	+0,7
5	Energy intensity of GDP	–0,9	–1,4	–2,0

Analysis of possible scenarios and directions for the development of world energy sector and energy sector in Ukraine. In the chosen model of technical and economic development of the state, different scenarios are possible: unfavorable (pessimistic), favorable (moderate), maximally favorable (optimistic) [8-10]. The most acceptable for Ukraine, given the existing internal and external factors, is, in our opinion, a moderate scenario, but its implementation also requires significant structural reforms. In the long term, the development of the domestic economy and energy sector will be determined by a combination of three principles – static, cyclical and dynamic [9, 11-14]. According to these principles, inertia of economic and energy development will prevail in Ukraine until 2050, followed by cyclical repetition at a higher level, and the dynamic principle makes us expect an acute complex crisis in the future, which will most likely be resolved by a complete change in the direction of energy sector development. Over the past 100 years, three such crises can be noted: the early 1930s, early 1970s, and the crisis of the late 2010s [9, 11].

The crisis of the early 1930s led to accelerated industrialization and a sharp increase in the demand for electricity and petroleum products for industry. The crisis of the early 70s was caused by the transition of the United States and Western Europe to the model of post-industrial development and the end of the Cold War. Here, private entrepreneurship became more active, the acceleration of the development of nuclear energy was noted, the demand for gas as the main fuel for the energy sector increased, etc. During the crisis, the growth rates of world energy consumption decline and may even become negative, but after the crisis, there is always a steady growth (Fig. 3) [9].

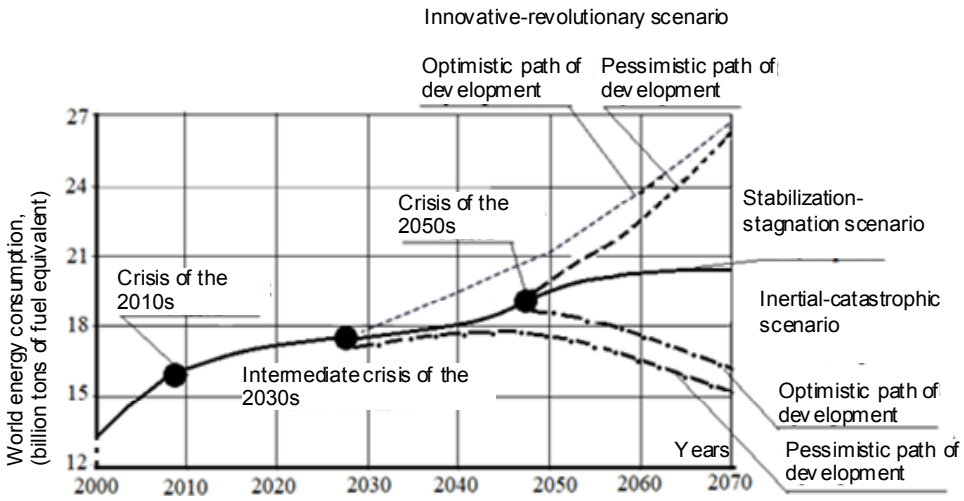

Fig. 3. Changes in electricity consumption under various scenarios for the development of the electric power industry

The crisis of the late 2010s caused the need to reevaluate and forecast new directions for energy sector development. The theory of cyclical development (N. Kondratyev theory of «long waves») was chosen as the theoretical basis for forecasting, which reduces forecasting errors, takes into account economic crises, energy saving and environmental safety requirements, increases the accuracy of identifying strategic problems and the volume of sufficient investments. According to this theory, the cycles of development of the economy, industry and energy sector have a duration of 50-55 years and are determined [9, 11] by:

1) accidental and temporarily acting factors (natural disasters, wars, accidents);

2) constantly acting non-cyclical factors (scientific and technological progress, demography, presence and availability of natural resources);

3) constantly acting cyclic factors (for TG these are electromagnetic and thermal effects, vibration, «aging»).

Analysis of the dynamics of energy sector development, taking into account the existing cyclicality, allows to expect the next crisis in the world economy and energy sector by 2040-2050, which will lead to new

qualitative, intellectual, energy-informational levels in the energy sector [9, 14-16].

After overcoming the next crisis, each state should choose scenarios for the development of national energy sector from three possible options:

1) inertial-catastrophic;
2) stabilization-stagnation;
3) innovative-revolutionary.

Each scenario has its own characteristics and ways of resolving contradictions, its own scale of demand for energy resources, features of the development of technologies for the production of primary energy resources and their consumption (see Fig. 3). Each scenario is characterized by the presence of two stages: the first one, which retains a certain inertia of the previous scenario, and the second one, in which the inertia is exhausted, a period of stagnation begins with signs of a latent or explicit energy crisis, and then the energy sector goes into a qualitatively new state. At the last stage, innovations are introduced into science and technology, there is a maximum rise in industry, new issues are formed that must be addressed at the next stage (cycle) and which will determine further development [11, 12, 16].

The most progressive in terms of energy sector development is the innovative-revolutionary scenario. It assumes qualitative changes in modern directions by 2020-2030 by improving the technology for generating electricity, its transmission and final consumption. In this scenario, the key trends in the development of world energy sector will be an increase in investment activity, the development and implementation of new technologies, an increase in the share of electricity in the total amount of energy used, a radical reduction in energy consumption [4, 9, 14-16]. The innovative-revolutionary scenario presupposes the formation of a new type of energy sector in developed and developing countries; growth in the volume of electricity in total global final energy consumption from 21.7 % (2010) to 28.6 % (2030) and up to 36.8 % in 2050.

It can be expected that by 2050 developing countries will reach the modern energy consumption standard of the countries of Europe and the USA, equal to 5 MWh per capita per year. Quantitative differences will decrease, but qualitative differences will increase, because it can be assumed that after 2030 in developed countries the formation of new generation energy systems based on smart grid technologies will begin. And, despite the unpopularity, the role of nuclear energy can be expected to increase: almost twice by 2030 and four times by 2050, since only NPPs, as sources of electricity, will be able to provide its required volume [6, 8, 10, 14, 17]. It is expected that in this case the development will receive: «thermal» reactors of 3-4 generations; fast reactors; reactor plants B-392, which use new solutions to increase the design life of the reactor pressure vessel up to 60 years; «small nuclear energy» which will somewhat reduce the consumption of uranium («uranium problem») and problems of storage and processing of spent nuclear fuel. It can be considered that the next 20-30 years nuclear power industry – highly productive, with a low level of emissions of substances that pollute the atmosphere, and with practically unlimited reserves of fuel – will be the main source of electricity [16, 18, 19].

At the same time, for Ukraine, the innovative-revolutionary scenario for the development of energy sector, economy and industry is unattainable in terms of technical, economic and political indicators. According to macroeconomic indicators, Ukraine is one of the poorest European countries with low incomes, which leads to the absence of a social and economic foundation for sustainable development. According to the International Finance Corporation [12, 17], the energy intensity of the gross domestic product (GDP) per USD 1 in our country is approximately 2-3 times higher than in developed European countries. Therefore, it can be argued that a stabilization-stagnation scenario of development is most likely for Ukraine [9, 18]. Here, while there are no new sources of electricity and sustainable systems for its storage, nuclear energy should be continued to develop and thermal energy (TPPs, CHPs) should be maintained in working order with the obligatory compliance of the national environmental policy with world requirements: the Kyoto Protocol (2005) and the Climate Conference in Paris (Paris Agreement, 12 Dec. 2015) [18-20].

It should be noted that there are threats to the energy security of Ukraine, both internal and external. Morally and physically obsolete electrical equipment of the power complex, outdated technological lines for the manufacture of new equipment, dependence on the export of both equipment and fuel resources, deficiencies in maintenance, diagnostics and repair have led to the fact that the power system of Ukraine has one of the largest losses of electricity in the «generation – transmission – distribution – consumption» cycle, that raises the question of the country's energy security. For example, energy losses in distribution networks reach 25 % [5, 21].

Internal factors include:

- excessive energy intensity of GDP, which has grown by 1.5 times in recent years. Energy costs for the manufacture of the main types of electrical products in Ukraine are 3.5-9 times higher than in the developed countries of the world [4, 16, 22];
- depreciation of fixed assets of the fuel and energy complex [16];
- insufficient investment in the electric power industry, including in the development of electrical engineering and in the renewal of equipment for power plants, in scientific research, in the improvement of technological processes at industrial enterprises and in the education system [4, 23];
- imperfection of the regulatory framework for the industry in market conditions, the crisis of payments at all levels [4, 13].

External factors include a high level of monopolization in the electric power sector, unregulated

by state supplies of imported fuel and energy resources and electrical equipment [16, 24], as well as the dependence of nuclear energy, the main supplier of electricity in Ukraine, on imports of nuclear fuel and equipment, and existing storage problems of spent nuclear fuel and nuclear waste [8, 16, 24]. More distant problems of nuclear power should also be noted: the decommissioning of NPPs units that have worked out the service life (taking into account the possible extension of this period), and the tasks of their subsequent maintenance. This is a common problem that is being addressed all over the world.

It can be concluded that the direction of development of the electric power industry is clearly national in nature, but it is obvious that in any scenario of development and any technical and economic state of the country, work should be continuously carried out to improve the TGs – the main sources of electricity for a very long time [16]. For the electric power industry of Ukraine, during the construction of new units and the modernization of the operating ones, it is necessary to use TGs of a larger unit power, to continue work on their improvement. This will provide the country with a sufficient amount of electricity, i.e. will ensure its energy independence, as well as TGs will become an item of export to many countries of the world, which will preserve the importance of Ukrainian products in the world market [16, 25].

Such an assessment of the future of the nuclear power industry may raise questions and objections against the background of the general enthusiasm for «green» energy. But already in 2018, the IAEA revised its forecasts for the development of nuclear power. The IAEA predicts an increase in energy production at NPPs until 2050: under the optimistic scenario – 3969 TWh in 2030 (11.5 % of the total world electricity production) and 6028 TWh in 2050 (11.7 %). Under the pessimistic scenario, these figures will amount to 2732 TWh in 2030 (10.3 % of the global electricity generation) and 2869 TWh in 2050 (5.6 %) [8, 10, 13, 26].

Today there are 450 operating NPP power units in the world. According to experts, the expansion of power at the present time, as well as the near and long-term growth prospects, are characteristic mainly for Asia. Of the 34 reactors under construction, 19 are located in Asia, and 28 of 39 recently commissioned reactors, which were connected to power grids, are located there [26]. Most of the power units are operated in the USA (100), France (58), Japan (43), Russia (36) and China (36). The total generating power of the NPPs is over 392 GW. Since 2018, the commissioning of new power has amounted to 302 GW, 117 GW have been decommissioned, as a result, the net increase in installed NPPs power is 185 GW [10, 24]. According to forecasts, by 2030, the total power of nuclear installations (with innovative-revolutionary scenario of development) will increase by 88 % [24].

The disasters at the Chernobyl nuclear power plant (1986) and at the Fukushima-1 nuclear power plant (2011) led to a rethinking of the idea that nuclear generation is a safe way to generate electricity. As a result, the Japanese authorities decided to work on the closure of all nuclear reactors in the country. Germany, which before the disaster was one of the largest consumers of nuclear energy, has now closed 8 of 17 reactors. Other European countries have also scaled back their plans to develop nuclear power. However, this did not force some countries to abandon plans to build NPPs in addition to existing HPPs and TPPs (coal and gas). In a number of countries where hydrocarbon resources are scarce, nuclear power is perceived as an efficient and economical way to generate electricity. The World Nuclear Association (WNA) states that more than 45 countries are actively striving to develop nuclear programs [10, 18, 24, 26].

One of the additional factors confirming the need to build new NPP units is the inadmissibility of the construction of TPP units, because it is the TPP emissions that determine the main threat to the environment. It should be noted that for countries with developed nuclear power, technologies for the disposal of radioactive waste are less expensive than technologies for the disposal of waste from TPPs, aimed at reducing harmful emissions to the required levels [18, 27].

Generating electricity from renewable energy sources (RES) can be considered a promising alternative. According to the forecast of the World Energy Council (WEC), the share of energy from RES by 2025 will account for 1150-1450 million tons of standard fuel (5.6-5.8 % of total energy consumption) [8, 13]. It is expected that the share of certain kinds will be: biomass – 35 %, solar energy – 13 %, hydropower – 16 %, wind energy – 18 %, geothermal energy – 12 %, ocean energy – 6 %. It was planned that by 2030 alternative sources could provide up to 40-50 % of the energy of the current level of its consumption, that the largest increase in electricity production until 2040 will be determined by the developing countries of Asia (up to 45 % of world electricity generation [15]) and that by 2040, global electricity production from RES will exceed 50 %. It is assumed that in European countries the share of RES (including hydropower) will reach 68-72 %, and only RES (excluding hydropower) will provide 51-56 %. So. Europe will become the second region after Central and Latin America, in which by 2040 more than half of the electricity is expected to come from non-fossil fuels (all types of RES including hydro resources) [12]. At the same time, according to the forecast, coal is expected to remain the dominant source of generation in developing countries in Asia by 2040; in North America, the Middle East and Africa – gas TPPs; in South and Central America, the first place will remain for the generation of electricity at hydroelectric power plants, and only in Europe, RES can become the main ones. Therefore, the assertion that mankind has no future without alternative energy sources to nuclear energy is, in our opinion, too categorical, but this only once again emphasizes the need to search, research and introduce new sources of

electricity, for example, hydrogen energy or controlled thermonuclear fusion energy.

The main disadvantages of RES should be considered the low specific density and inconstancy of electricity generation, dependence on weather conditions, time of year and day, low efficiency (with the exception of hydroelectric power plants), high cost with low unit power of power plants. The inconstancy of primary energy resources (wind, sun), up to a complete absence, makes it necessary to install and maintain additional energy accumulators and/or backup sources. As a result, the cost of the generated energy turns out to be high even in the absence of a fuel component in the final price of electricity.

The low specific power of RES requires an increase in the number of power units. For example, the average annual value of the specific power of solar panels for the sunniest regions of the world (taking into account seasonal and weather fluctuations) does not exceed 250 W/m^2, and in Ukraine, the average density of solar radiation on the earth's surface at noon on a clear day is about 120 W/ m^2. In our latitudes, even in cloudless weather, solar panels rarely operate at full capacity, on average this figure is 50-60 % in summer and 10-15 % in winter, i.e. a 275 W panel will generate about 140-145 Wh on a summer day. On average, in Ukraine, a solar panel with power of 1 kW in a year generates 1100 kWh of electricity (Fig. 4) [2, 16, 28]. Similarly, wind energy has a low specific power: the average specific energy density of the wind flow, as a rule, does not exceed several hundred W/ m^2. At a wind speed of 10 m/s, the specific energy density will be about 500 W/ m^2.

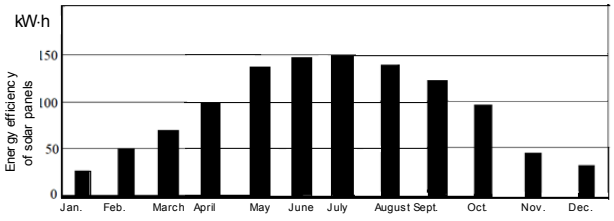

Fig. 4. Average electricity generation by solar panels in Ukraine per 1 kW of installed power

In Ukraine, only in some regions (4 % of the territory) a steady wind speed («wind rose») is 4-4.5 m/s, so the specific energy density is insignificant, up to 100 W/m^2. For comparison, the energy density of a water flow with speed of 1 m/s is about 500 W/ m^2, and the density of the heat flow, which «presses» on the walls of steam boilers at TPPs and NPPs, reaches several hundred kW/ m^2 [16, 29, 30].

The COVID-19 pandemic (2020-2021) has changed the forecasts for the development of the electric power industry, caused more disruptions in the energy sector than any other event, and its consequences can be expected to be felt for years to come. Currently it is difficult to assess how the current crisis will affect the development of the electric power industry: whether it will accelerate or slow down the creation of a safe and sustainable energy system. The pandemic is not over yet, which introduces uncertainty in energy consumption issues, and it is probably too early to predict important decisions in the field of energy policy. In addition, the economic crisis is causing significant changes in the strategic orientation of energy companies and investors, in the activity of energy consumers. The World Energy Prospects Program [3, 12, 21] contains two possible scenarios: optimistic (The Stated Policies Scenario, STEPS – a forward-looking policy scenario) and pessimistic (Delayed Recovery Scenario, DRS). According to STEPS forecast, global energy demand will recover to the level of the beginning of the pandemic by early 2023, but in the event of a protracted pandemic, an even larger decline is expected (according to DRS) and demand will only recover by 2025.

Before the epidemic, a forecast was made that electricity consumption for the period 2019-2030 will grow by 12 %. The growth forecast has now changed to 9 % (STEPS) or 4 % (DRS). And this growth will mainly be driven by developing countries (China, India). In countries with developed economies, the demand for electricity is decreasing, investments in the energy sector and in the production of new equipment are decreasing, and the volume of construction work is decreasing [24]. But under any scenarios and features of the current period, all researchers predict an increase in energy consumption. Therefore, it can be argued that for the next 20-30 years, with all the understanding of the problems of nuclear energy, the daily, sustainable supply of electricity to the population of the planet will be provided by NPPs, i.e. by TGs installed on units [8, 13, 19, 24].

The main directions and problems of creating modern TGs. In world practice, since the middle of the last century, the unit power of the TGs has increased by 7-7.5 times, from 200 to 1500 MW, and if we count from 1898, when Charles Brown (since 1971 Abegg and Rauhut) produced the first 6-pole TG with power of 100 kVA, the power increased by 15000 time. At the same time, the dimensions and weight of the TGs increased, which at a certain moment created the problem of their creation and transportation by rail and determined the task of minimizing the volume and weight with increasing power. Until 2000, the insufficient power of the electric networks also limited the power of the TGs, since in the event of an emergency shutdown of a powerful generator, problems arose with the stability of the network. At present, the total power of electric grids has become higher, they have become more resistant to sudden switching off of generating units, and an increase in the power of TGs has become possible. The prospect of increasing power is also confirmed by international practice (Siemens, ABB Alstom Power, Hitachi, General Electric, Westinghouse): in Great Britain and the USA they are designing 2000 MW TGs, in France two TGs with

power of 1550 MW are already operating, General Electric is developing two TGs with power of 1750 MW for Chinese NPPs. It should be emphasized that all world Companies are oriented on 4-pole generators [16, 30-33].

To increase the power, it would be logical to increase the dimensions and weight of the machines, but, as indicated, this complicates their manufacture and transportation, and increases the cost. Therefore, the increase in power is currently being considered without changing the dimensions. The design takes into account the technological capabilities of related industries: the capabilities of metallurgical enterprises, turbine-building enterprises, enterprises for the creation of controlled nuclear reactors, the possibility of transporting TGs to the consumer [34-36]. The increase in power is also expedient from the point of view of economic indicators. For example, the total mass, cost and losses of several TGs are always greater than the mass, cost and losses of one machine of the same power. It is calculated that when using one TG instead of several, the power of which is equal to the power of one TG, the mass, cost and losses decrease approximately $\sqrt[4]{m}$ in comparison with the same indicators m of TGs of lower power. On the example of TGV-300-2 turbogenerator, the possibility of increasing the power from 300 MW to 500 MW by changing the electromagnetic and geometric parameters of the structure (within acceptable limits) with practically the same dimensions is shown [16].

Hundreds of TGs operate at the power plants of each power system, i.e. any TG on the unit operates in parallel with other generators in the power system. For stable operation, all of them must generate consistent voltage, otherwise equalizing currents will arise between machines operating in parallel on the same electrical network. For this, the rotors of all generators must rotate at synchronous speed and at each moment of time occupy a certain angular position. In case of loss of stability, there is a massive shutdown of generators, the power system «falls apart». It is because of this that a major accident occurred in the United States in 1965 [37]. 7 states with a population of about 30 million people were left without electricity, the damage exceeded USD 100 million. The only part of the power system that was not affected is the area of Fort Erie near Buffalo, Ontario, which was powered by old generators with frequency of 25 Hz. For 5 minutes, chaos reigned in the power distribution system in the northeastern United States, as due to overloads that cascaded throughout the network, the TGs were disconnected by the protection system.

Unfortunately, the higher the power of the TG, the less «stable» it is in parallel operation. This is because with the growth of the unit power of the TGs, they try not to change their mass and dimensions. In powerful TGs, the rotors become relatively lighter, less inertial and, therefore, less stable in emergency modes (Table 2). With each new step in increasing the TG power, the problem of reducing stability becomes more and more urgent and requires additional research.

Table 2

Data of the TGs of power 63-1200 MW

ТГ	Power, MW	Rotor mass, t	TG mass, t	Ratio of the rotor mass to the total mass of the TG, %	Manufacturer
TVF-63-2	63	25,4	123,6	20,6	JSC «Electrosila»
TVF-110-2E	110	28,9	151	19,1	
TVF-120-2	120	30,8	179	17,2	
TVF-200-2	200	41,8	265	15.8	
TGV-200-2	200	48,7	321	15,2	SE «Plant «Electrotyazhmash»
TGV-200-2M	200	48,1	256	18,1	
TGV-300-2	300	55,8	364	15,3	
TVM-300-2	300	50,4	333	15,1	JSC «Electrosila»
TVV-320-2	320	55,1	340	16,2	
TVV-500-2	500	65	444	14,6	
TVV-800-2	800	84,0	615	13,7	
TVV-1000-2	1000	86,5	641	13,5	
TVV-1200-2	1200	96	670	14,3	

Figure 5 shows the tendency of change in the relative rotor mass (the ratio of the rotor mass to the total mass of the TG, %) with a change in the TG power.

The decrease in the stability of the system due to the relative decrease in the mass of the rotors of the generators is compensated by the use of high-speed thyristor excitation control systems and automatic voltage regulators: with smaller mass of the rotor, its inertia decreases and during transients (or at a short circuit) the rotor of the TG begins to «swing», i.e. the stability of its parallel operation with the electric network decreases, but the automatic excitation control system increases the excitation current. Here, electromagnetic forces increase in the generator, which, as it were, connect it with other TGs, which protects the power system from collapse.

To maintain the characteristics of domestic TGs at the world level, in addition to the above tasks, additional research is needed to ensure trouble-free operation of TGs

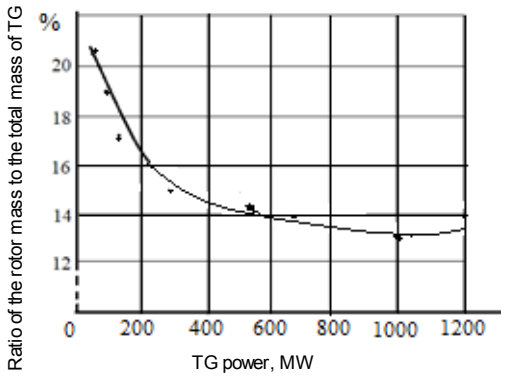

Fig. 5. Dependence of the ratio of the rotor mass to the total mass of the TG, depending on the power

in transient modes associated with «peaks» and «dips» of power consumption, operation in modes of reactive power consumption, it is necessary to reduce maintenance and repairs costs to ensure the reliability and durability of individual units and parts. Increasing the efficiency of the TGs also requires improving the supply systems (gas, water and oil supply systems), improving and increasing the reliability of the excitation system, introducing automatic systems for monitoring the state of the TG, using the methods of modern technical diagnostics of the most stressed joints and elements both in online mode, and during scheduled and emergency repairs.

The current stage is characterized by the emergence of new types of TGs, steel grades and insulating materials, the development of new methods of extending the service life of TGs installed at TPP and NPP units [23, 36]. To establish the pre-emergency state of the TG, identify defects, and exclude long-term downtime due to emergency shutdowns, it is necessary to introduce complex diagnostic systems [25, 30]. Work continues to further increase the power per unit of performance due to the introduction of new electrical insulating materials, forgings with higher strength characteristics, electrical steels with lower specific losses, to intensify the cooling of windings and cores [30-32].

Also, when creating modern TGs, it is necessary to comprehensively solve scientific problems related both directly to TGs and to systems of excitation, regulation, control and protection [16, 31]. When developing new designs, it is necessary to take into account the peculiarities of the power system operation and, accordingly, the operation of the TG in non-nominal modes: with «peaks» and «dips» of the load, operation with the condition of ensuring the balance of active and reactive energy in the network, etc. The TGs installed at power plants are not designed for such operating conditions: they are not maneuverable enough and are limited in solving the issue of reactive power regulation; have terms of operation exceeding the terms established by the manufacturer. The latter causes additional problems: «aging» of insulation and wear of structural materials, decrease in mechanical reliability and integrity of laminated stator cores, fasteners, etc. [16, 36]. Therefore, when designing a TG, additional requirements should be established:

- ensuring increased maneuverability of the TG with the possibility of at least short-term consumption of reactive energy from the network. The consumption of reactive energy should be limited only by the stability of the generator operation in the power system, and not by thermal and mechanical processes in the machine;
- ensuring high controllability, the possibility of regulating the TG rotation frequency (up to short-term asynchronous modes) while maintaining power, ensuring their stable connection with the grid in order to increase the economic and operational performance of the power plant [27, 31];
- ensuring the possibility, when carrying out repairs and modernization of TGs, to increase their power in the established size, improve the cooling system, make the necessary changes in the design of inactive elements of the TG using modern calculations, technologies and new materials.

Developers of modern TGs should:

- to maintain constant technical indicators when changing operating modes of the power system, to know the permissible limits of TG participation in maintaining the balance of active and reactive power;
- when increasing the power of the TG in the process of their modernization, to achieve the preservation of dimensions for the use of existing foundations and supporting systems;
- to improve the TG cooling system, carry out work on the replacement of cooling agents, in particular, in TGs with power of 300 MW and more, to replace explosive and fire hazardous hydrogen with air [30];
- to ensure the competitiveness of TGs, continue work to reduce their specific weight (kg/kW) by improving the design of the inactive zone [7, 36];
- to improve the programs for assessing the technical condition of TGs to determine the possibility of extending their service life, establishing the necessary and sufficient amount of repair work;
- to continue researching the prospects of installing asynchronized TGs at TPP units in parallel with operating synchronous TGs to increase the reliability and stability of their operation and the operation of the system [16];
- to improve the system of targeted training and retraining of specialists of all levels (skilled workers, engineers), solve the issues of ensuring the economic interest of power plant workers to keep them in the national electric power industry [23].

It should be noted that the creation of modern TGs is necessary not only for TPPs and NPPs. The creation of new types of TG is also necessary for modern wind power. Increasing the power of WPPs requires an increase in the power of generators. This increases the weight of the machine, which must be installed at an ever greater height. For example, a 12 MW WPP tower (Haliade X, General Electric) has height of 260 m [28, 40]. For such installations, the issue of reducing the weight of

each element and, first of all, the generator is one of the main tasks.

The use of TGs with magnetoelectric excitation (with excitation from permanent magnets) instead of electromagnetic excitation does not solve this problem. A promising solution can be considered the use of generators with HTSC windings, which will reduce the weight and dimensions of superconducting generators by 3-4 times in comparison with conventional generators of the same power. A generator with HTSC windings for a WPP with power of 8 MW will have diameter of 3 m and weight of 120 tons, while a conventional («warm») TG of the same power will have diameter of 9 m and weight of 450 tons, i.e. the weight of the TG with HTSC windings will be 3 times less. Besides, the cost of the WPP will also decrease from 6.7 to 3.2 million USD. According to the studies carried out, the weight of additional cryogenic equipment for different designs of the HTSC generator is less than 4 % of the total weight of the generators, i.e. the additive is insignificant [38, 39].

Also, when TGs with superconducting windings are used for WPPs, the production areas required for their installation will decrease, which are usually very significant. Thus, an offshore WPP SG 14-222 DD (power 14 MW, working diameter 222 m, length of one blade 108 m) requires the area of $39 \cdot 10^3$ m^2 [21, 28, 40]. (For comparison, the area of one NPP power unit with a 1000 MW generator and with a VVER-1000 reactor is about $9.1 \cdot 10^3$ m^2). Some parameters of WPPs with a TG with power of 10 MW with different types of superconducting windings are given in Table 3.

Table 3

Parameters of WPPs with different types of TGs with power of 10 MW with superconducting windings

Parameter	TG with windings of LTSC conductors Nb_3Ti (General Electric)	TG with windings of HTSC conductors (AMSC – American Superconductor)	TG with windings of LTSC conductors MgB_2 (Kalsi Engineering)
Rotational speed of WPP blades, rpm	10	10	10
Rated voltage of the generator stator winding, kV	3,3	0,69	4,5
Rated current, A	1750	–	1360
Cooling medium operating temperature, K	4	80	30
Mass of the generator with additional cryogenic equipment, t	143	150	52,5
Outer diameter of the generator, m	4,0	4,5-5	5
WPP diameter, m	160	190	150
Cost (as for 2018), thousand USD	4963	–	3168,0

For the NPPS, such disadvantages as the problems of storage and disposal of spent nuclear fuel are known. But RES also have similar problems – the issue of recycling spent installations and their individual elements. Utilization of large WPPs, especially their blades, is a difficult task. The blades are designed to withstand extreme weather conditions: frost, heat, hurricane winds. According to the Bloomberg New Energy Finance research Company, starting from 2022, in Europe alone, it will be necessary to dispose of approximately 3800 wind turbine blades annually [28, 42].

Researchers note that dismantling and disposal of small onshore WPPs is a difficult, but to some extent already worked out procedure, but dismantling of large offshore WPPs has yet to be mastered. In UK they calculated the costs of dismantling out-of-date offshore wind farms (located offshore). According to the optimistic forecast, it will be necessary to spend 1.85 billion USD, according to the pessimistic one – more than 5.2 billion USD.

It can also be expected that the appearance of large areas of wind farms can affect the natural movement of air masses, will facilitate the process of mixing warm and cold air. And solar panels will reduce the reflectivity of the Earth's surface. All this will lead to climate change and new environmental problems.

Since 2009, the EPR (European Pattern Recognition) project has been operating in Europe under the name «PV Cycle». Under this program, since 2014, self-disposal of solar panels has become mandatory for all manufacturers (EU Directive 2012/19/EU Waste Electrical and Electronic Equipment, WEEE) [41, 43]. Centers for the collection of «solar» waste were established. Some panels are considered hazardous due to lead or cadmium, and because it is impossible to determine the degree of danger, experts advise to consider all solar panels dangerous. Since 2020, all solar panel manufacturers that trade in the US markets must participate in the solar energy waste collection program (EPR project). Therefore, the main problem for the use of solar panels is to ensure that the costs of production and disposal are commensurate.

The disadvantages of renewable energy should also include the features of the operation of generators from RES on the overall energy system, the impact on its stability. Due to the instability of generating electricity from RES, the number of different types of power plants with renewable sources should be limited. This, in particular, concerns ensuring the stability of dynamic processes in power supply systems and, accordingly, changes in the organization of dispatch control. The general energy system cannot use large RES without

increasing the number of maneuverable powers. A significant introduction of RES, if it is not accompanied by the installation of additional sources of energy storage, requires additional power control systems to balance the constant fluctuations in energy production and consumption. Also, an increase in the number of power plants from RES in the power system will lead to a reduction in the contribution to the energy supply of traditional power plants, which is good, but will complicate the ability to regulate the frequency and voltage in the event of loss of generation or load [2, 40]. Balancing electricity consumption and maintaining the voltage frequency in the grid are the main technical problems in power systems with significant installed RES power. In Ukraine, according to the calculations of Ukrenergo, the maximum installed power of solar and wind power plants, which the unified energy system can accept without deviations in operation, is 3 GW [2, 3, 21].

Conclusions.

For the sustainable development of the Ukrainian electric power industry and ensuring its energy security, it is necessary:

1. When choosing technical and economic solutions for the development of the electric power industry, one should focus on the stabilization-stagnation scenario with an increase in investments in the implementation of environmental programs.

2. To carry out work on the construction of new units and on the improvement of electrical equipment of operating nuclear power plants, as the main sources of electricity for the next 20-30 years. During the construction of new nuclear power plant units, it is necessary to introduce new types of reactors, more advanced equipment, new technologies for generating, transforming, transmitting and distributing electricity.

3. To continue work to improve the turbogenerators: increase their power (up to 1500 MW and more), use new designs of excitation systems, introduce modern cooling systems, etc. For the installed turbogenerators, expand the service and post-repair tests program, carry out modernization using modern technologies and materials in order to extend the service life, use a comprehensive online monitoring of the technical condition of the turbogenerators.

4. To maintain in working order, modernize the electrical equipment of thermal power plant units to ensure sustainable energy supply to consumers until the launch of new nuclear power plant units and the creation of industrially significant plants from renewable energy sources. The construction of new thermal power plant units is impractical due to the significant impact on the environment.

5. To continue work on the development of the electric power industry from renewable energy sources. For power plants from renewable energy sources that operate on the unified energy system, install sources of flexible powers, which will ensure stable operation in transient modes, and improve the dispatch control system. It is necessary to continue work on solving environmental problems that may arise when using renewable energy sources, in particular, on the issue of recycling elements of installations that have worked out the established service life. To supply energy to individual consumers in Ukraine, it is advisable to develop solar and wind energy (with power of up to 100 kW).

6. To resume investigations on the use of high-temperature superconductors to create electrical equipment (turbogenerators and other elements of the power system) with superconducting windings.

Conflict of interest. The authors declare that they have no conflicts of interest.

REFERENCES

1. Zvorykin A., Pioro I., Panchal R. Study on Current Status and Future Developments in Nuclear-Power Industry of Ukraine. *Proceedings of the 2016 24th International Conference on Nuclear Engineering. Volume 5: Student Paper Competition*. Charlotte, North Carolina, USA. June 26-30, 2016. V005T15A020. ASME. doi: https://doi.org/10.1115/icone24-60336.

2. *Renewables in Ukraine 2019. KPMG in Ukraine*. July 2019. 20 p. Available at: https://assets.kpmg/content/dam/kpmg/ua/pdf/2019/07/Renewables-in-Ukraine-2019.pdf (accessed 12.03.2021).

3. *Energy strategy of Ukraine for the period up to 2035 «Security, energy efficiency, competitiveness»*. Ukraine Ministry of Energy. (Ukr). Available at: http://mpe.kmu.gov.ua/minugol/control/uk/doccatalog/list?currDir=50358 (accessed 12.03.2021).

4. Loiko V.V., Loiko D.M. Dynamics of Ukraine industry development as an integrated provision of economic security of national economy. *Scientific Notes of «KROK» University*, 2019, no. 4 (56), pp. 176-184. (Ukr). doi: https://doi.org/10.31732/2663-2209-2019-56-176-184.

5. *Energy of Ukraine. Ukraine: annual electricity losses in worn-out networks are estimated at UAH 20 billion*. (Rus). Available at: https://ukrenergy.dp.ua/2020/11/21/ukraina-ezhegodnye-poteri-elektroenergii-v-iznoshennyh-setyah-oczenivayutsya-v-20-mlrd-grn.html (accessed 12.03.2021).

6. Lindh P.M., Petrov I., Semken R.S., Niemela M., Pyrhonen J.J., Aarniovuori L., Vaimann T., Kallaste A. Direct liquid cooling in low-power electrical machines: proof-of-concept. *IEEE Transactions on Energy Conversion*, 2016, vol. 31, no. 4, pp. 1257-1266. doi: https://doi.org/10.1109/tec.2016.2597059.

7. Abegg K. The Growth of Turbogenerators. *Philosophical Transactions of the Royal Society of London. Series A, Mathematical and Physical Sciences*, 1973, vol. 275, no. 1248, pp. 51-67. Available at: www.jstor.org/stable/74298 (accessed 12.03.2021).

8. Cho R. *Energy. The State of nuclear energy today – and what lies ahead*. Available at: https://news.climate.columbia.edu/2020/11/23/nuclear-power-today-future/ (accessed 12.03.2021).

9. Shevchenko V.V., Lutai S.N. The role of crises in the world energy development dynamics and the theory of cyclical development. *Scientific papers of Donetsk National Technical University. Series: Electrical and Power Engineering*, 2013, no. 2 (15), pp. 266-272. (Rus). doi: https://doi.org/10.5281/zenodo.2549796.

10. IAEA. Country Nuclear Power Profiles. Ukraine, 2020. Available at:

https://cnpp.iaea.org/countryprofiles/Ukraine/Ukraine.htm (accessed 12.03.2021).
11. Marshall M. Theories of long waves: from Kondratieff to Mandel. *Long Waves of Regional Development. Critical Human Geography*, 1987. Palgrave, London. doi: https://doi.org/10.1007/978-1-349-18539-9_2.
12. U.S. Chamber of Commerce's Global Energy Institute, 2020. *International Index of Energy Security Risk. Assessing Risk in a Global Energy Market*. Available at: https://www.globalenergyinstitute.org/sites/default/files/IESRI-Report_2020_4_20_20.pdf (accessed 12.03.2021).
13. World Energy Council, 2020. *World Energy Trilemma Index*. Available at: https://www.worldenergy.org/publications/entry/world-energy-trilemma-index-2020 (accessed 12.03.2021).
14. OECD, 2019. *State-Owned Enterprise Reform in the Hydrocarbons Sector in Ukraine*. OECD Publishing, 2018. Norwegian Ministry of Foreign Affairs. 67 p. Available at: http://www.oecd.org/corporate/SOE-Reform-in-the-Hydrocarbons-Sector-in-Ukraine-ENG.pdf (accessed 12.03.2021).
15. Price L., Wang X., Yun J. The challenge of reducing energy consumption of the Top-1000 largest industrial enterprises in China. *Energy Policy*, 2010, vol. 38, no. 11, pp. 6485-6498. doi: https://doi.org/10.1016/j.enpol.2009.02.036.
16. Shevchenko V.V. *Prospects for the creation of competitive turbogenerators for TPP and NPP*. Saarbrücken, LAP Lambert Academic Publishing, 2016. 144 p. (Rus).
17. Benkovskyi L. *Nuclear Energy System of Ukraine for near and medium term (2030-2035) and International Collaboration in developing sustainable NES of Ukraine.* National Nuclear Energy Generating Company of Ukraine «Energoatom» INPRO Dialogue Forum 11 «Roadmaps for a Transition to Globally Sustain-able NES», 2015, IAEA, Vienna, Austria. Available at: https://nucleus.iaea.org/sites/INPRO/df11/Presentations/day3/session4/(benkovskyi)_for_df-11_last.pdf (accessed 12.03.2021).
18. *The future of the global electric power industry. Preparing for new opportunities and threats*. Available at: https://www2.deloitte.com/content/dam/Deloitte/ru/Documents/energy-resources/ru_The_future_of_global_power_sector_RUS.pdf (accessed 12.03.2021).
19. *Nuclear Power in Ukraine (Updated January 2021)*. Available at: https://www.world-nuclear.org/information-library/country-profiles/countries-t-z/ukraine.aspx (accessed 12.03.2021).
20. *Paris Agreement. EU Action*. Available at: https://ec.europa.eu/clima/policies/international/negotiations/paris_en (accessed 12.03.2021).
21. Zvorykin A., Pioro I., Fialko N. Electricity generation in the world and Ukraine: Current status and future developments. *Mechanics and Advanced Technologies*, 2017, no. 2 (80), pp. 5-24. doi: https://doi.org/10.20535/2521-1943.2017.80.113757.
22. *RG-N Series (Generators for Nuclear Power Plants)*. Available at: https://power.mhi.com/products/generators/lineup/rg-n (accessed 12.03.2021).
23. Shevchenko V.V. The reform of the higher education of Ukraine in the conditions of the military-political crisis. *International Journal of Educational Development*, 2019, vol. 65, pp. 237-253. doi: https://doi.org/10.1016/j.ijedudev.2018.08.009.
24. *IAEA Releases New Projections for Nuclear Power Through 2050*. Vienna, Austria. Available at: https://www.iaea.org/newscenter/pressreleases/iaea-releases-new-projections-for-nuclear-power-through-2050 (accessed 12.03.2021).
25. Shevchenko V.V., Maslennikov A.M. The scheme to reduce turbo-generator mass and dimensions. *Reporter of the Priazovskyi State Technical University. Section: Technical sciences*, 2015, no. 30, vol. 2, pp. 137-144. (Rus). Available at: http://journals.uran.ua/vestnikpgtu_tech/article/view/52736 (accessed 12.03.2021).
26. *Nuclear power: 7 candidates for the «Nuclear Club»*. (Rus). Available at: https://www.skc.ru/press/news/item/4227408 (accessed 12.03.2021).
27. Shevchenko V.V. To issue of ensuring of competitiveness of domestic turbogenerators. *Electrotechnic and Computer Systems*, 2016, no. 22 (98), pp. 226-231. (Rus). Available at: https://eltecs.op.edu.ua/index.php/journal/article/view/1398 (accessed 12.03.2021).
28. *7 Types of Renewable Energy: The Future of Energy*. Available at: https://justenergy.com/blog/7-types-renewable-energy-future-of-energy (accessed 12.03.2021).
29. Milykh V.I., Polyakova N.V. Automated calculations of the dynamics of turbogenerator electromagnetic processes in software environment FEMM. *Electrical Engineering & Electromechanics*, 2015, no. 6, pp. 24-30. (Rus). doi: https://doi.org/10.20998/2074-272x.2015.6.04.
30. Minko A.N., Shevchenko V.V. Improving heat exchange systems of turbogenerators for increase of their efficiency. *Problemele Energeticii Regionale*, 2019, no. 1 (39), pp. 80-89. (Rus). doi: http://doi.org/10.5281/zenodo.2650425.
31. Satake Y., Takahashi K., Waki T., Onoda M., Tanaka T. Development of large capacity turbine generators for thermal power plants. *Mitsubishi Heavy Industries Technical Review*, June 2015, vol. 52, no. 2, pp. 47-54. Available at: https://power.mhi.com/randd/technical-review/pdf/index_14e.pdf (accessed 12.03.2021).
32. Shevchenko V.V. Influence of manufacturing quality of laminated core on a turbogenerator exploitation term. *Electrical Engineering & Electromechanics*, 2016, no. 4, pp. 28-33. doi: https://doi.org/10.20998/2074-272x.2016.4.04.
33. Vaskovskyi Yu.M., Melnyk A.M. The electromagnetic vibration disturbing forces of turbogenerator in maneuverable operating conditions. *Technical Electrodynamics*, 2016, no. 2, pp. 35-41. (Ukr). doi: https://doi.org/10.15407/techned2016.02.035.
34. Revuelta P.S., Litrán S.P., Thomas J.P. *Active power line conditioners: design, simulation and implementation for improving power quality*. Elsevier Inc., Academic Press, 2016. 436 p. doi: https://doi.org/10.1016/C2014-0-02915-2.
35. Milykh V.I., Polyakova N.V. Determination of electromagnetic parameters and phase relations in turbo-generators by the automated calculation of the magnetic field in the software environment FEMM. *Electrical Engineering & Electromechanics*, 2016, no. 1, pp. 26-32. doi: https://doi.org/10.20998/2074-272x.2016.1.05.
36. Shevchenko V.V., Minko A.N., Strokous A.V. Analysis of electromagnetic vibration forces in the elements of the turbogenerator stator fastening to the case in non-nominal operation modes. *Electrical Engineering & Electromechanics*, 2018, no. 5, pp. 29-33. doi: https://doi.org/10.20998/2074-272x.2018.5.05.
37. *Northeast blackout of 1965*. Available at: https://en.wikipedia.org/wiki/Northeast_blackout_of_1965 (accessed 12.03.2021).
38. Terao Y., Seta A., Ohsaki H., Oyori H., Morioka N. Lightweight design of fully superconducting motors for

electrical aircraft propulsion systems. *IEEE Transactions on Applied Superconductivity*, 2019, vol. 29, no. 5, pp. 1-5, art. no. 5202305. doi: https://doi.org/10.1109/tasc.2019.2902323.

39. Terao Y., Sekino M., Ohsaki H. Comparison of conventional and superconducting generator concepts for offshore wind turbines. *IEEE Transactions on Applied Superconductivity*, 2013, vol. 23, no. 3, art. no. 5200904. doi: https://doi.org/10.1109/TASC.2012.2237223.

40. Shevchenko V.V., Shayda V.P., Pototsky D.V. Theoretical and practical directions for the turbogenerators creation, taking into account the electric power industry development. *Proceedings of the 9th International scientific and practical conference «Fundamental and applied research in the modern world»* (USA, Boston, April 14-16, 2021). USA, BoScience Publisher, 2021, pp. 110-118. doi: https://doi.org/10.5281/zenodo.4818355.

41. Chowdhury M.S., Rahman K.S., Chowdhury T., Nuthammachot N., Techato K., Akhtaruzzaman M., Tiong S.K., Sopian K., Amin N. An overview of solar photovoltaic panels' end-of-life material recycling. *Energy Strategy Reviews*, 2020, vol. 27, art. no. 100431. doi: https://doi.org/10.1016/j.esr.2019.100431.

42. *Energy. What materials are used to make wind turbines?* Available at: https://www.usgs.gov/faqs/what-materials-are-used-make-wind-turbines?qt-news_science_products=0#qt-news_science_products (accessed 12.03.2021).

43. *Understanding your solar panel payback period*. 31 August, 2020. Available at: https://moxiesolar.com/2020/08/31/https-moxiesolar-com-blog-understanding-your-solar-panel-payback-period (accessed 12.03.2021).

Received 19.03.2021
Accepted 15.05.2021
Published 27.08.2021

V.V. Shevchenko[1]*, Doctor of Technical Science, Associate Professor,*
A.N. Minko[2]*, PhD,*
M. Dimov[3]*, PhD,*
[1] National Technical University «Kharkiv Polytechnic Institute», 2, Kyrpychova Str., Kharkiv, 61002, Ukraine,
e-mail: zurbagan8454@gmail.com (Corresponding author)
[2] Research and Production Company with Limited Liability «Ecopolymer»,
42-a, Tobolska Str., Kharkiv, 61072, Ukraine,
e-mail: alexandr.minko@i.ua
[3] Trakia University,
8600 Yambol, Bulgaria.
e-mail: milendimov@protonmail.ch

How to cite this article:
Shevchenko V.V., Minko A.N., Dimov M. Improvement of turbogenerators as a technical basis for ensuring the energy independence of Ukraine. *Electrical Engineering & Electromechanics*, 2021, no. 4, pp. 19-30. doi: https://doi.org/10.20998/2074-272X.2021.4.03.

UDC 621.3 https://doi.org/10.20998/2074-272X.2021.4.04

H. Benbouhenni, A. Driss, S. Lamdani

INDIRECT ACTIVE AND REACTIVE POWERS CONTROL OF DOUBLY FED INDUCTION GENERATOR FED BY THREE-LEVEL ADAPTIVE-NETWORK-BASED FUZZY INFERENCE SYSTEM – PULSE WIDTH MODULATION CONVERTER WITH A ROBUST METHOD BASED ON SUPER TWISTING ALGORITHMS

Aim. *This paper presents the minimization of reactive and active power ripples of doubly fed induction generators using super twisting algorithms and pulse width modulation based on neuro-fuzzy algorithms.* ***Method.*** *The main role of the indirect active and reactive power control is to regulate and control the reactive and active powers of doubly fed induction generators for variable speed dual-rotor wind power systems. The indirect field-oriented control is a classical control scheme and simple structure. Pulse width modulation based on an adaptive-network-based fuzzy inference system is a new modulation technique; characterized by a simple algorithm, which gives a good harmonic distortion compared to other techniques.* ***Novelty.*** *adaptive-network-based fuzzy inference system-pulse width modulation is proposed. Proposed modulation technique construction is based on traditional pulse width modulation and adaptive-network-based fuzzy inference system to obtain a robust modulation technique and reduces the harmonic distortion of stator current. We use in our study a 1.5 MW doubly-fed induction generator integrated into a dual-rotor wind power system to reduce the torque, current, active power, and reactive power ripples.* ***Results.*** *As shown in the results figures using adaptive-network-based fuzzy inference system-pulse width modulation technique ameliorate effectiveness especially reduces the reactive power, torque, stator current, active power ripples, and minimizes harmonic distortion of current (0.08 %) compared to classical control.* References 22, tables 4, figures 30.

Key words: **doubly fed induction generators, pulse width modulation, neuro-fuzzy algorithms, indirect field-oriented control.**

Мета *У статті представлено мінімізацію пульсацій реактивної та активної потужності асинхронних генераторів подвійного живлення з використанням алгоритмів суперскрутки та широтно-імпульсної модуляції на основі нейро-нечітких алгоритмів.* ***Метод****. Основна роль непрямого управління активною та реактивною потужністю полягає у керуванні та регулюванні реактивної та активної потужностей асинхронних генераторів з подвійним живленням для вітроенергетичних систем з подвійним ротором змінної швидкості. Непряме керування, орієнтоване на поле, - це класична схема керування та проста структура. Широтно-імпульсна модуляція, заснована на системі нечітких висновків на основі адаптивної мережі, є новим методом модуляції; характеризується простим алгоритмом, який дає гарні гармонічні спотворення порівняно з іншими методами.* ***Новизна****. Пропонується адаптивна мережа на основі нечіткого висновку із широтно-імпульсною модуляцією. Запропонована побудова методу модуляції базується на традиційній широтно-імпульсній модуляції та системі нечітких висновків на основі адаптивних мереж для отримання надійного методу модуляції та зменшення гармонічних спотворень струму статора. У нашому дослідженні ми використовуємо асинхронний генератор з подвійним живленням потужністю 1,5 МВт, інтегрований у вітроенергетичну систему з подвійним ротором, щоб зменшити пульсації крутного моменту, струму, активної потужності та реактивної потужності.* ***Результати****. Як показано на рисунках з результатами, використання методу широтно-імпульсної модуляції на основі нечітких висновків системи адаптивних мереж покращує ефективність, особливо зменшує реактивну потужність, крутний момент, струм статора, пульсації активної потужності, та мінімізує гармонійне спотворення струму (0,08 %) порівняно з класичним керуванням.* Бібл. 22, табл. 4, рис. 30.

Ключові слова: **асинхронні генератори з подвійним живленням, широтно-імпульсна модуляція, нейро-нечіткі алгоритми, непряме керування, орієнтоване на поле.**

Introduction. In recent years, the traditional pulse width modulation (PWM) technique has drawn much attention from industry and research groups. The main advantages of the traditional PWM technique are its ease of implementation and simple algorithm compared to space vector modulation (SVM). But, this strategy gives more harmonic distortion of voltage and electromagnetic torque ripples. To overcome the drawbacks of the traditional PWM technique, a fuzzy PWM strategy has been presented [1, 2]. In the fuzzy PWM strategy, the hysteresis comparators are replaced by the fuzzy controllers. This proposed strategy minimized the harmonic distortion of voltage compared to the classical PWM technique. In [3], the authors proposed the use of a PWM technique with a neural algorithm applied to the doubly fed induction generators (DFIG) drive, where the hysteresis comparators are replaced by neural algorithms. The simulation results show that the neural PWM technique is better than the classical PWM strategy in terms of reducing the harmonic distortion of voltage and torque ripples. In [4, 5], the fuzzy PWM strategy reduced the harmonic distortion of voltage compared to SVM and neural SVM techniques.

Recently, the Indirect Active and Reactive Powers Control (IARPC) method has been widely used for the control of AC machines. IARPC, based on classical PI controllers, has attracted a lot of research control machines for the last two decades. The IARPC method is one of the most used control techniques for wind power. This technique is simple algorithms. This technique is similar to field-oriented control (FOC). In [6], the authors proposed the use of an IARPC method with the neural SVM technique. In [7], an IARPC command based on a two-level fuzzy SVM technique has been proposed. The simulation results show that the IARPC control with fuzzy SVM strategy is better than traditional IARPC with classical SVM strategy in terms of minimizing the torque and active power ripples. In [8], a modified IARPC control scheme was proposed based on neuro-fuzzy algorithms with SVM strategy, where PI regulators were replaced by four controllers based on neuro-fuzzy

algorithms. In [9], the IARPC control is the robust control compared to the direct active and reactive powers control (DARPC) of DFIG. IARPC control and three-level fuzzy SVM techniques are combined to reduce the torque, active and reactive power ripples of the DFIG [10].

The **aim** of this paper is the reduces the active and reactive power ripples and improve the effectiveness of the indirect active and reactive powers control using the proposed pulse width modulation technique and super twisting algorithms (STA) for doubly fed induction generators based dual-rotor wind turbine (DRWT) system under variable speed wind and also to minimize fluctuations in current, active power, torque, and reactive power.

In this work, the IARPC with STA controllers and three-level Adaptive-Network-based Fuzzy Inference System – Pulse Width Modulation (ANFIS-PWM) technique has been considered. The original contribution of this work is the application of the STA controllers and three-level ANFIS-PWM technique in the IARPC method with a DFIG-based DRWT system. The proposed method is compared with a classical IARPC control. The simulation results validate that the STA-IARPC with ANFIS-PWM technique reduced the torque, active and reactive powers ripples of the DFIG-based DRWT systems.

Three-level ANFIS-PWM technique. The classical PWM technique goal is to control the three-level inverter. In the three-level PWM technique, six hysteresis comparators were used. The PWM technique, which is designed to control the classical three-level converter, is shown in Fig. 1. PWM techniques are widely used as front-end converters in electronic drives. The advantage of a classical three-level PWM technique is a simple modulation scheme and easy to implement compared to the SVM strategy. Its application has been in electronic drives and controls. But this technique gives more harmonic distortion of voltage and electromagnetic torque of AC machine drive.

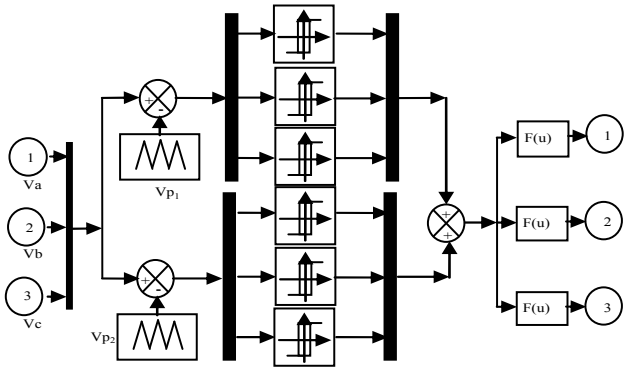

Fig. 1. The classical three-level PWM strategy

In order to improve the classical three-level PWM performances, complimentary use of the ANFIS algorithm is proposed. The principle of the three-level ANFIS-PWM technique is similar to the classical three-level PWM technique. The difference is using the ANFIS algorithm to replace the classical hysteresis comparators. Figure 2 shows the principle of the ANFIS-PWM strategy of a three-level inverter. Major advantages of proposed PWM techniques are as follows: minimized active and reactive powers ripples, a simple algorithm, and robust strategy. On the other hand, voltage space vectors generated by the three-level inverter in the coordinate system α-β are shown in Fig. 3, there are a totally of 27 vectors: 25 active vectors and three zero vectors in α-β coordinate systems. In this work, the modulation method with the use of 6 controllers from the same technique has been applied.

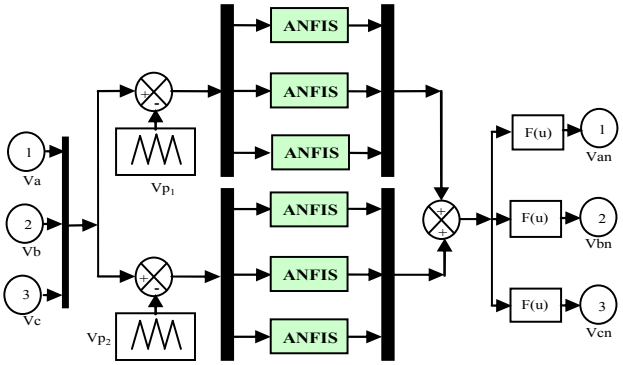

Fig. 2. The three-level ANFIS-PWM strategy

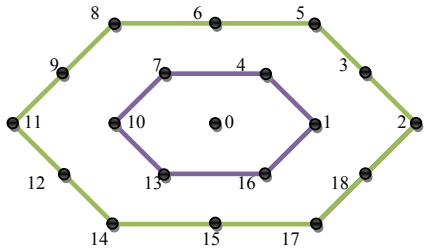

Fig. 3. Voltage space vectors generated by three-level inverter in the coordinate system α–β

The schematic diagram of the ANFIS regulator is given in Fig. 4. Membership functions in triangular shape are shown in Fig. 5. The rule base of the ANFIS is shown in Table 1.

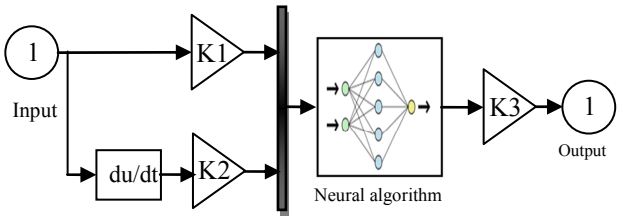

Fig. 4. Block diagram of the ANFIS algorithm

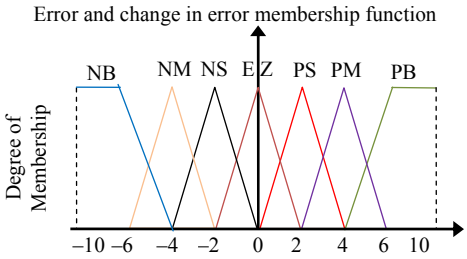

Fig. 5. Membership functions

Table 1

ANFIS rules of the hysteresis comparators

Δe \ e	NB	NM	NS	EZ	PS	PM	PB
NB	NB	NB	NB	NB	NM	NS	EZ
NM	NB	NB	NB	NM	NS	EZ	PS
NS	NB	NB	NM	NS	EZ	PS	PM
EZ	NB	NM	NS	EZ	PS	PM	PB
PS	NM	NS	EZ	PS	PM	PB	PB
PM	NS	EZ	PS	PM	PB	PB	PB
PB	EZ	PS	PM	PB	PB	PB	PB

ANFIS algorithms were originally introduced in 1993 [11], the advantage of an ANFIS algorithm is a simple method and robust. This regulator has combined the advantages of the fuzzy and neural controllers. In order to make the ANFIS algorithm, we used the conventional neural network with Conjugate Gradiant with Beale-Powell Restarts algorithm. In MATLAB software, traincgb is the word we use to accomplish this algorithm.

The schematic diagram of the neural regulator of the ANFIS algorithm is shown in Fig. 6.

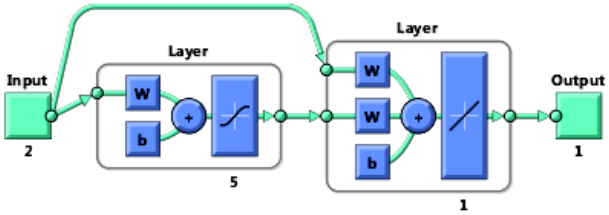

Fig. 6. Schematic diagram of the neural regulator

The neural controllers consist of an input layer, two hidden layers, and an output layer. The parameters of the neural regulator for the ANFIS algorithms are shown in Table 2.

Table 2

Parameters of the neural regulator

Parameters	Values
Training	Conjugate Gradiant with Beale-Powell Restarts (traincgb)
TrainParam.Lr	0.05
TrainParam.goal	0
Performances	Mean Squard Error (mse)
TrainParam.mu	0.8
Number of input layer	1
Number of neurons for input layer	2
TrainParam.eposh	300
Number of output layer	1
Number of neurons for output layer	1
TrainParam.show	50
derivative	Default (default deriv)
Number of hidden layer	1
Number of neurons for hidden layer	5
Coeff of acceleration of convergence (mc)	0.8
Functions of activation	Tensing, Purling, traincgb

Figure 7 shows the neural network training performance of the ANFIS algorithm of the PWM technique by using the conjugate gradiant with the Beale-Powell restarts algorithm.

IARPC strategy. The IARPC algorithm was originally introduced in the 1970s [12]. The IARPC strategy goal is to control the reactive and active powers of the DFIG-based DRWT systems (Fig. 8)

$$\psi_{qs} = 0, \quad \psi_{ds} = \psi_s, \tag{1}$$

$$V_{qs} = 0, \quad V_{ds} = \omega_s \psi_s. \tag{2}$$

$$\begin{cases} I_{ds} = -\dfrac{M}{L_s} I_{dr} + \dfrac{\psi_s}{L_s}; \\ I_{qs} = -\dfrac{M}{L_s} I_{qr}. \end{cases} \tag{3}$$

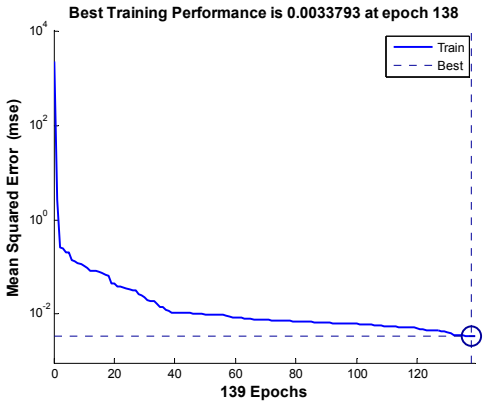

Fig. 7. Training performance

The expression of the rotor voltages are:

$$\begin{cases} V_{dr} = R_r \cdot I_{dr} - w_r \cdot (L_r - \dfrac{M^2}{L_s}) \cdot I_{qr}; \\ V_{qr} = R_r \cdot I_{qr} + w_r \cdot (L_r - \dfrac{M^2}{L_s}) \cdot I_{dr} + g \cdot \dfrac{M \cdot V_s}{L_s}. \end{cases} \tag{4}$$

The expression of the rotor fluxes and powers becomes:

$$\begin{cases} \Psi_{dr} = (L_r - \dfrac{M^2}{L_s}) I_{dr} + \dfrac{M.V_s}{L_s \cdot w_s}; \\ \Psi_{qr} = (L_r - \dfrac{M^2}{L_s}) I_{qr}. \end{cases} \tag{5}$$

$$\begin{cases} P_s = -\dfrac{3}{2} \dfrac{\omega_s \psi_s M}{L_s} I_{qr}; \\ Q_s = -\dfrac{3}{2} \left(\dfrac{\omega_s \psi_s M}{L_s} I_{dr} - \dfrac{\omega_s {\psi_s}^2}{L_s} \right). \end{cases} \tag{6}$$

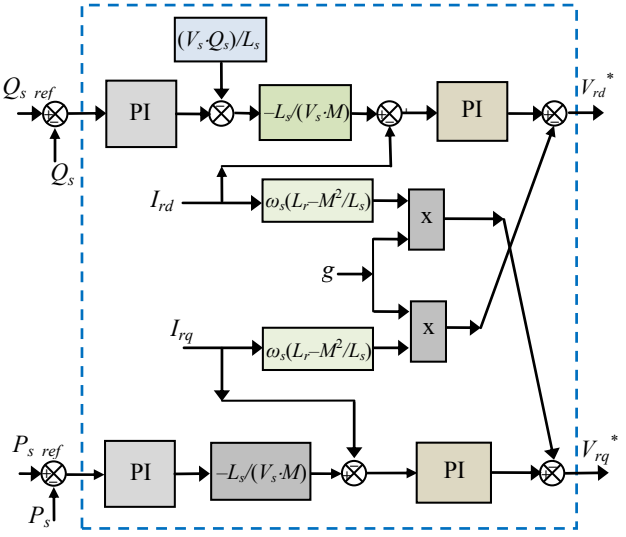

Fig. 8. Structure of the IARPC strategy

The IARPC strategy of a three-phase DFIG-based DRWT system with PWM technique is shown in Fig. 9.

STA-IARPC method with ANFIS-PWM technique. The main objective of using the STA- IARPC method is to develop a robust control of active and reactive powers of the DFIG-based DRWT system. In our

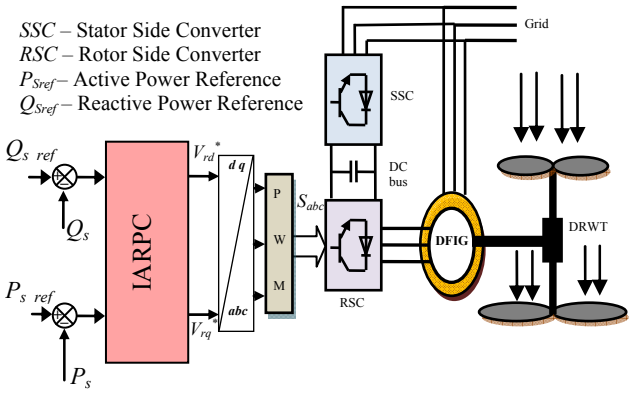

Fig. 9. IARPC strategy of the DFIG

system, the reactive and active powers are respectively controlled by V_{dr} and V_{qr}.

In the aim to design an advanced IARPC method with very small active and reactive powers undulations and without harmonic distortion of current, in our work, we suggest employing a new IARPC method based on a three-level ANFIS-PWM technique and STA algorithms for a DFIG-based DRWT system. This is for essential objects, including minimizing torque ripple and improving active and reactive power quality provided to the grid.

Since the STA algorithm generalizes the basic second-order sliding mode control design by integrating second-order derivatives of the sliding variable. This strategy is proposed by Levant in 1993 [13]. The STA algorithms have gained importance in the recent past due to their fast response and superior control characteristics. The STA algorithm maintains the advantages of the classical sliding mode control. This algorithm eliminated the phenomena of chattering compared to the classical sliding mode control strategy. In [14], the authors suggest the use of a direct torque and flux control (DTFC) with the STA algorithm employed to DFIG drive. A neural STA regulator was designed to improve the DTFC control of DFIG [15]. Fuzzy controller and STA algorithm are combined to reduce the torque ripple of DFIG controlled by DTFC control [16]. ANFIS-STA algorithm is proposed to reduce the harmonic distortion and electromagnetic torque ripple of DFIG [17]. In [18], direct field-oriented control (DFOC) was proposed based on the STA algorithm with the SVM strategy. The experimental results show that the DFOC with the STA algorithm is the robust control compared to the classical DFOC strategy. In [19], direct reactive and active power control (DRAPC) strategy based on the STA algorithm has been proposed. In [20], a modified DRAPC strategy was proposed based on the neural STA algorithm with a two-level SVM technique, where the PI regulators are replaced by the neural STA algorithms. However, active and reactive power ripples are considered the main drawback of the conventional DRAPC method. In [21], the authors proposed the use of a DRAPC with an ANFIS-STA algorithm applied to the DFIG-based wind turbine.

The output signal from the STA regulator is comparable with the control signal obtained from linear PI regulators. The mathematical model of the STA regulator can be written as follows [22]:

$$\begin{cases} u = K_p |S|^r \operatorname{sgn}(S) + u_1; \\ \dfrac{du_1}{dt} = K_i \operatorname{sgn}(S). \end{cases} \quad (15)$$

where S is the switching function determined for the STA regulator; r is the exponent defined for the STA regulator; K_i and K_p are the coefficients of the integral and proportional parts of the STA regulator, respectively.

The schematic diagram of the STA regulator is presented in Fig. 10.

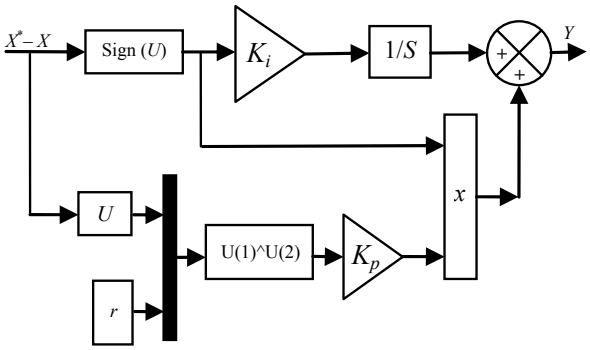

Fig. 10. Schematic diagram of the STA regulator

Compared with the traditional IARPC strategy, the STA-IVC with three-level ANFIS-PWM technique ensures diverse advantages such as the reduction of torque ripple, harmonic distortion of current/voltage, active power ripples. Furthermore, it keeps the robust control, a simple method of control with almost no changes in the basic structure of the IARPC strategy. The IARPC strategy of a three-phase DFIG-based DRWT system with the application of the classical STA regulators and ANFIS-PWM technique is shown in Fig. 11.

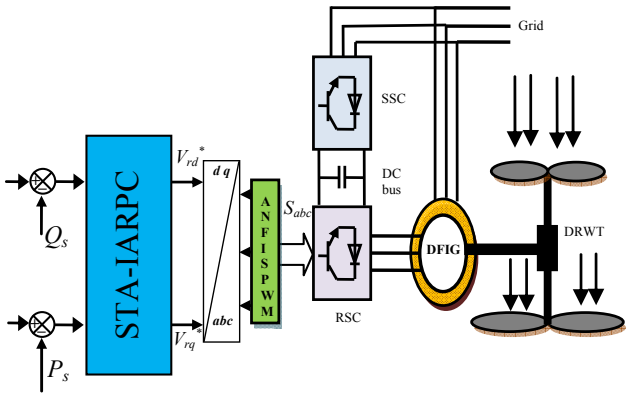

Fig. 11. IARPC strategy of the DFIG with the application of STA algorithm and ANFIS-PWM technique

In this control strategy, the reactive and active powers are controlled by the four STA regulators (Fig. 12).

Simulation results. The DFIG used in this work is a 1.5 MW, 380/690 V, 50 Hz, a machine whose nominal parameters are reported in Table 3. Both control schemes classical IARPC and proposed control are simulated and compared in terms of reference tracking, robustness against machine parameter variations, and current harmonics distortion. The simulations are lead with the MATLAB software.

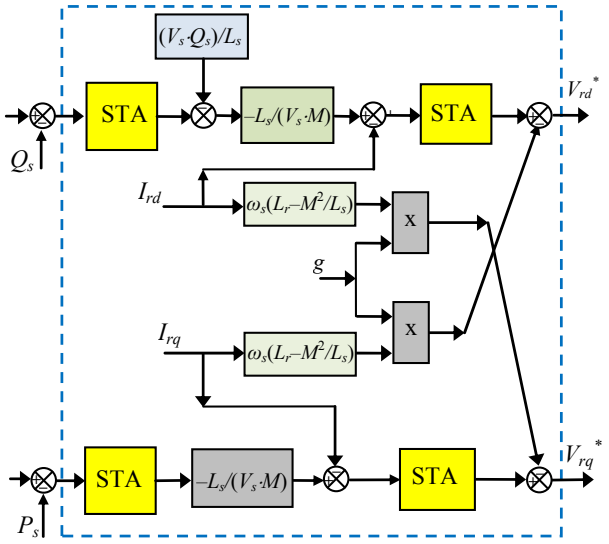

Fig. 12. Structure of the STA-IARPC strategy

Table 3

Parameters of the simulated DFIG

P_n, MW	1.5
V_n, V	380
p	2
R_s, Ω	0.012
R_r, Ω	0.021
L_s, H	0.0137
L_r, H	0.0136
L_m, H	0.0135
J, kg·m^2	1000
f_r, Nm·s/rad	0.0024
f, Hz	50

First test. The objective of this test is to study the behavior of both IARPC strategies while the DFIG's speed is considered maintained at its nominal value. Figures 15-18 show the obtained simulation results. The simulation waveforms of the reference and measured active power of the DFIG are shown in Fig. 15. To compare the performance of the proposed control with the performance of the classical IARPC command with the traditional PWM technique. At the load condition, the reactive power becomes identified as the load active power. On the other hand, these waveforms demonstrate that the analyzed STA algorithm allows obtaining control signal with the waveforms similar to the output signals from linear PI regulators. It can be seen that the active power is controlled properly at the given reference value.

The trajectory of the estimated of reactive power for the proposed control schemes is shown in Fig. 16. It can be stated that the reactive power is controlled properly at the nominal value.

The simulation waveform of all electromagnetic torque of the DFIG for the considered control system is shown in Fig. 17. The amplitude of the electromagnetic torque depend on the value of the load active power.

The simulation waveform of all stator phase currents of DFIG for the considered control system is shown in Fig. 18. The amplitude of the stator currents depends on the state of the drive system and the value of the load active and reactive powers. On the other hand, Fig. 13, 14 show the harmonic spectrum of the stator current of the DFIG-based DRWT system for the classical IARPC and proposed control strategy. It can be observed that the THD value is minimized for a proposed control (0.08 %) when compared to classical IARPC with a three-level PWM strategy (0.47 %).

The response time of the torque, reactive and active powers for both methods are shown in Table 4. It can be stated that the proposed control minimized more the response time of the electromagnetic torque, reactive and active powers compared to classical IARPC with a three-level PWM strategy.

Table 4

Comparative analysis of response time

	Response time		
	Active power	Torque	Reactive power
IARPC-PWM	0.135 s	0.135 s	0.122 s
Proposed control	3 ms	3 ms	3.7 ms

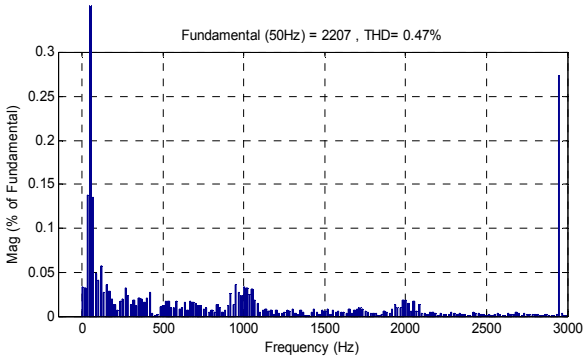

Fig. 13. THD of the IARPC control

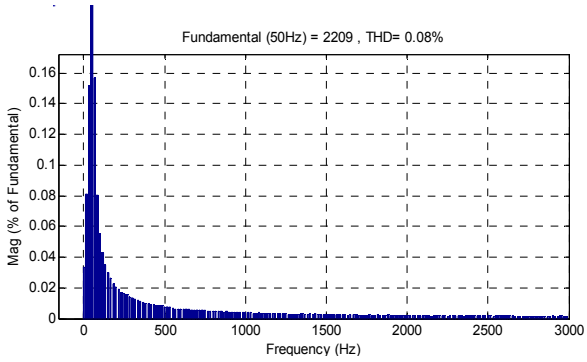

Fig. 14. THD of the STA-IARPC-ANFIS-PWM method

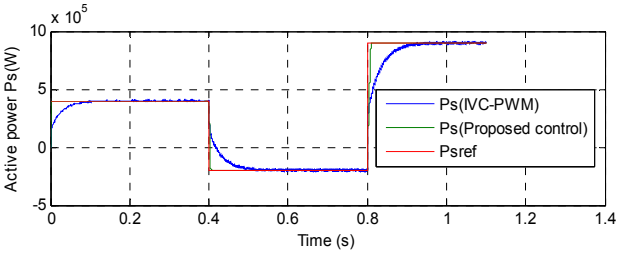

Fig. 15. Stator active power P_s

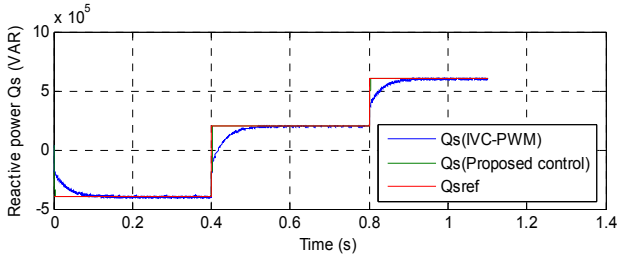

Fig. 16. Stator reactive power Q_s

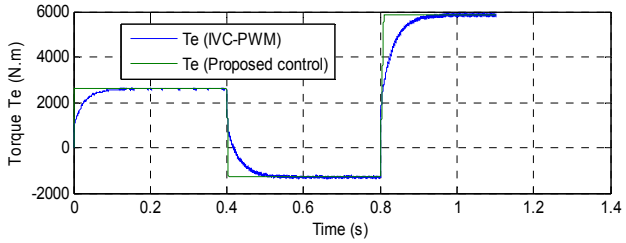

Fig. 17. Torque T_e

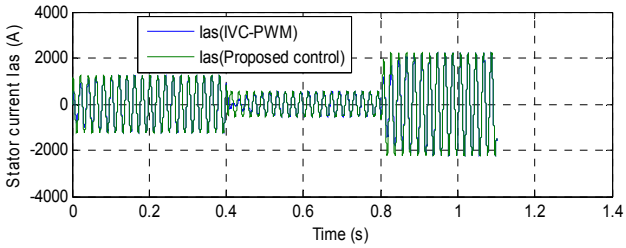

Fig. 18. Stator current I_{as}

The zoom of the active power, reactive power, torque, and stator current of the DFIG-based DRWT system is shown in Fig. 19-22, respectively. As can be seen, the proposed control minimized the ripples in torque, current, active and reactive powers compared to the classical IARPC control.

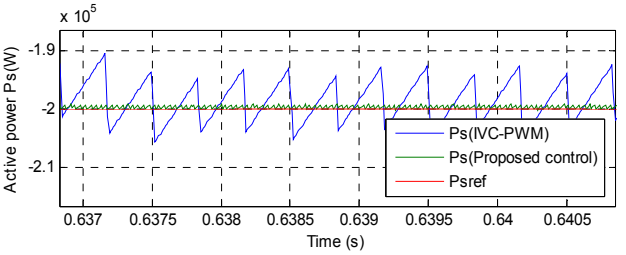

Fig. 19. Zoom in the active power P_s

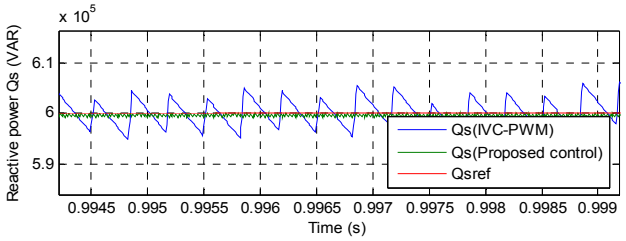

Fig. 20. Zoom in the reactive power Q_s

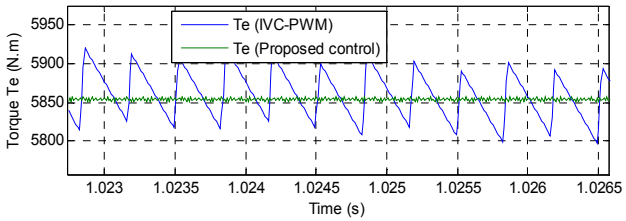

Fig. 21. Zoom in the torque T_e

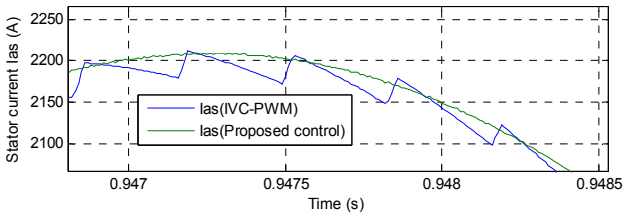

Fig. 22. Zoom in the current I_{as}

Second test. For analyzing the robustness of the used proposed strategy, the DFIG parameters have been intentionally changed such as the values of the stator and the rotor resistances R_s and R_r are doubled and the values of inductances L_s, L_r and M are divided by 2. The DFIG is running at its nominal speed. Simulation results are presented in Fig. 23-27. As shown by these Figures, we notice that parameter variations of the DFIG increase slightly the time-response of the proposed strategy. On the other, hand these results show these variations present a clear effect on the torque, reactive power, stator current, and active power curves and that the effect appears more important for the classical IARPC than that with the designed strategy (Fig. 28-30). According to the simulation results in Fig. 23, 24, the THD value of the output stator current is about 2.06 % and 0.11 % for classical IARPC and proposed strategy, respectively. Thus it can be concluded that the proposed strategy is more robust than the classical IARPC control.

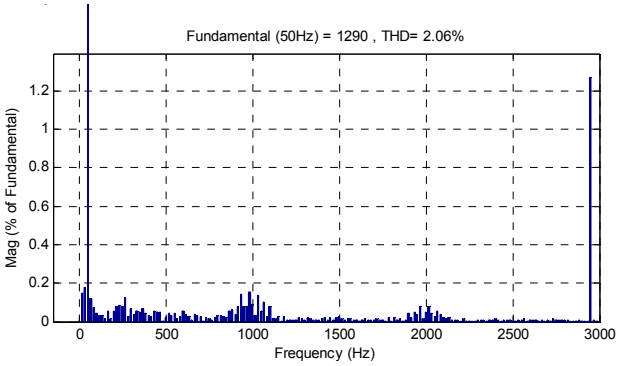

Fig. 23. THD of the IARPC control

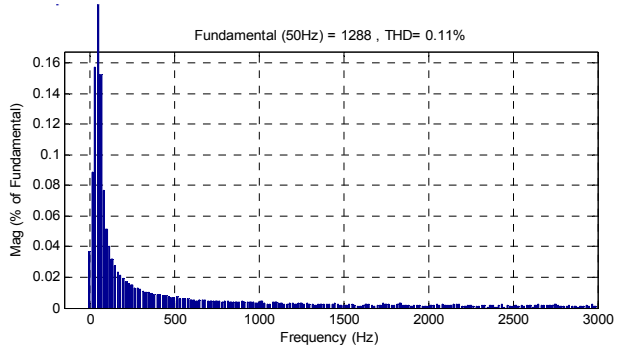

Fig. 24. THD of the STA-IARPC-ANFIS-PWM control

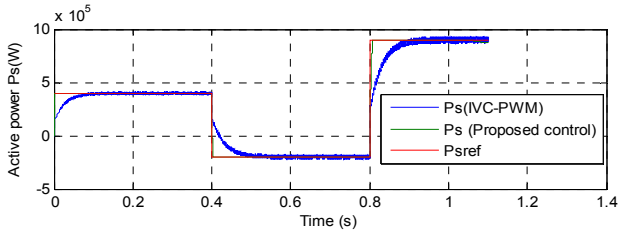

Fig. 25. Active power P_s

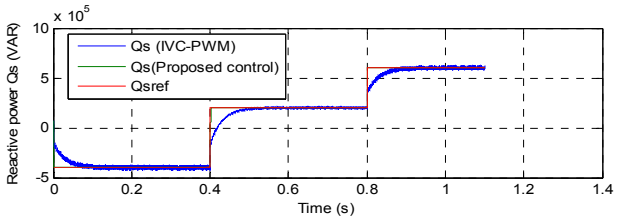

Fig. 26. Reactive power Q_s

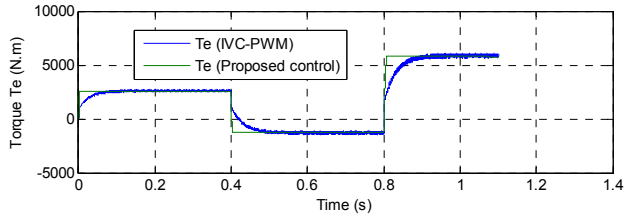

Fig. 27. Torque T_e

The zoom of the active power, reactive power, and torque of the DFIG-based DRWT system is shown in Fig. 28-30, respectively. As can be seen, the designed strategy minimized the ripples in torque, active and reactive powers compared to the traditional IARPC strategy.

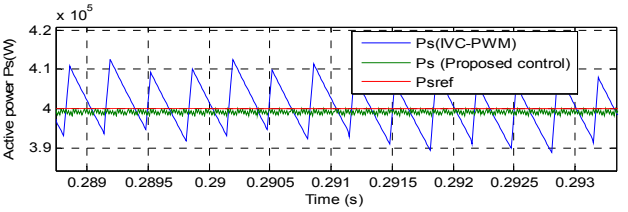

Fig. 28. Zoom in the active power

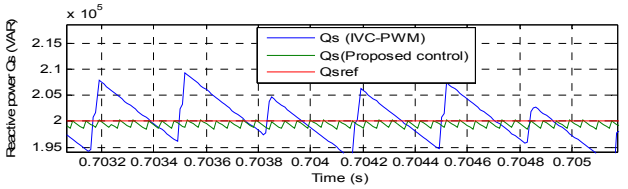

Fig. 29. Zoom in the reactive power Q_s

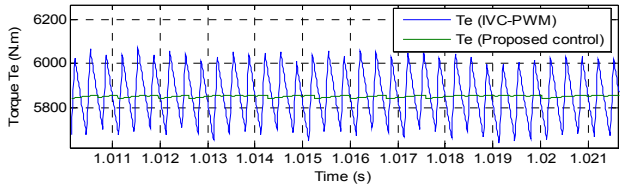

Fig. 30. Zoom in the torque T_e

Conclusion.

In this work, the super-twisting sliding mode called super twisting algorithms (STA) is developed and applied to three-phase doubly fed induction generators (DFIG) based dual-rotor wind turbine (DRWT) systems using three-level adaptive-network-based fuzzy inference system – pulse width modulation (ANFIS-PWM) techniques. The performance of the super twisting algorithms-the indirect active and reactive powers control (STA-IARPC) control with three-level ANFIS-PWM techniques is evaluated and compared with traditional IARPC and the regular STA-IARPC methods in the context of power control of the DFIG for linear loads. Simulation results show that the STA-IARPC with three-level ANFIS-PWM technique reduced the active and reactive powers ripples compared to the traditional IARPC strategy. Moreover, the STA-IARPC strategy with three-level ANFIS-PWM techniques has faster dynamic responses compared to the traditional IARPC strategy. Also, STA-IARPC with three-level ANFIS-PWM technique reduced the harmonic distortion of stator current compared to the classical IARPC strategy. Detailed simulation results using MATLAB software are presented. Basing on all these results it can be concluded that robust strategy as the STA-IARPC strategy with three-level ANFIS-PWM technique can be a very attractive solution for devices using DFIG such as DRWT systems.

Conflict of interest. The authors declare that they have no conflicts of interest.

REFERENCES

1. Benbouhenni H. FPWM technique based converter for IM drives. *Acta Electrotechnica et Informatica,* 2019, vol. 19, no. 1, pp. 32-41. doi: https://doi.org/10.15546/aeei-2019-0005.

2. Benbouhenni H., Boudjema Z., Belaidi A. DFIG-based WT system using FPWM inverter. *International Journal of Smart Grid*, 2018, vol. 2, no. 3, pp. 142-154. Available at: https://www.ijsmartgrid.org/index.php/ijsmartgridnew/article/view/16 (accessed 14 March 2021).

3. Benbouhenni H. Sliding mode with neural network regulator for DFIG using two-level NPWM strategy. *Iranian Journal of Electrical & Electronic Engineering*, 2019, vol. 15, no. 3, pp. 411-419. doi: http://dx.doi.org/10.22068/IJEEE.15.3.411.

4. Benbouhenni H. A comparison study between fuzzy PWM and SVM inverter in NSMC control of stator active and reactive power control of a DFIG based wind turbine systems. *International Journal of Applied Power Engineering*, 2019, vol. 8, no. 1, pp. 78-92. doi: https://doi.org/10.11591/ijape.v8.i1.pp78-92.

5. Benbouhenni H. Comparison study between FPWM and NSVM inverter in neuro-sliding mode control of reactive and active power control of a DFIG-based wind energy. *Majlesi Journal of Energy Management*, 2017, vol. 6, no. 4, pp. 15-23. Available at: http://journals.iaumajlesi.ac.ir/em/index/index.php/em/article/view/338 (accessed 14 March 2021).

6. Benbouhenni H., Boudjema Z., Belaidi A. A comparative study between four-level NSVM and three-level NSVM technique for a DFIG-based WECSs controlled by indirect vector control. *Carpathian Journal of Electronic and Computer Engineering*, 2018, vol. 11, no. 2, pp. 13-19. doi: https://doi.org/10.2478/cjece-2018-0012.

7. Benbouhenni H., Boudjema Z., Belaidi A. Indirect vector control of a DFIG supplied by a two-level FSVM inverter for wind turbine system. *Majlesi Journal of Electrical Engineering*, 2019, vol. 13, no. 1, pp. 45-54. Available at: http://mjee.iaumajlesi.ac.ir/index/index.php/ee/article/view/2693 (accessed 14 March 2021).

8. Amrane F., Chaiba A. A novel direct power control for grid-connected doubly fed induction generator based on hybrid artificial intelligent control with space vector modulation. *Revue Roumaine des sciences techniques. Série Électrotechnique et Énergétique*, 2016, vol. 61, no. 3, pp. 263-268. Available at: http://revue.elth.pub.ro/index.php?action=details&id=597 (accessed 12 May 2020).

9. Benbouhenni H. Comparative study between different vector control methods applied to DFIG wind turbines. *Majlesi Journal of Mechatronic Systems*, 2018, vol. 6, no. 4, pp. 15-23. Available at: http://journals.iaumajlesi.ac.ir/ms/index/index.php/ms/article/view/382 (accessed 14 March 2021).

10. Benbouhenni H., Boudjema Z., Belaidi A. Using three-level Fuzzy space vector modulation method to improve indirect vector control strategy of a DFIG based wind energy conversion systems. *International Journal of Smart Grid*, 2018, vol. 2, no. 3, pp. 155-171. Available at: https://www.ijsmartgrid.org/index.php/ijsmartgridnew/article/view/15 (accessed 14 March 2021).

11. Jang J.-S.R. ANFIS: adaptive-network-based fuzzy inference system. *IEEE Transactions on Systems, Man, and Cybernetics*, 1993, vol. 23, no. 3, pp. 665-685. doi: https://doi.org/10.1109/21.256541.

12. Benbouhenni H. Intelligence indirect vector control of a DFIG based wind turbines. *Majlesi Journal of Electrical*

Engineering, 2019, vol. 13, no. 3, pp. 27-35. Available at: http://mjee.iaumajlesi.ac.ir/index/index.php/ee/article/view/2972 (accessed 14 March 2021).
13. Levant A. Sliding order and sliding accuracy in sliding mode control. *International Journal of Control*, 1993, vol. 58, no. 6, pp. 1247-1263. https://doi.org/10.1080/00207179308923053.
14. Boudjema Z., Taleb R., Djerriri Y., Yahdou A. A novel direct torque control using second order continuous sliding mode of a doubly fed induction generator for a wind energy conversion system. *Turkish Journal of Electrical Engineering & Computer Sciences*, 2017, vol. 25, no.2, pp. 965-975. doi: https://doi.org/10.3906/elk-1510-89.
15. Benbouhenni H. Rotor flux and torque ripples minimization for direct torque control of DFIG by NSTSM algorithm. *Majlesi Journal of Energy Management*, 2018, vol. 7, no. 3, pp. 1-9. Available at: http://journals.iaumajlesi.ac.ir/em/index/index.php/em/article/view/369 (accessed 12 May 2020).
16. Benbouhenni H. Stator current and rotor flux ripples reduction of DTC DFIG drive using FSTSMC algorithm. *International Journal of Smart Grid*, 2019, vol. 3, no. 4, pp. 226-234. Available at: https://www.ijsmartgrid.org/index.php/ijsmartgridnew/article/view/82 (accessed 14 March 2021).
17. Benbouhenni H. Utilization of an ANFIS-STSM algorithm to minimize total harmonic distortion. *International Journal of Smart Grid*, 2020, vol. 4, no. 2, pp. 56-67. Available at: https://www.ijsmartgrid.org/index.php/ijsmartgridnew/article/view/98 (accessed 14 March 2021).
18. Listwan J. Application of super-twisting sliding mode controllers in direct field-oriented control system of six-phase induction motor: experimental studies. *Power Electronics and Drives*, 2018, vol. 3, no. 1, pp. 23-34. doi: https://doi.org/10.2478/pead-2018-0013.
19. Bouyekni A., Taleb R., Boudjema Z., Kahal H. A second-order continuous sliding mode based on DFIG for wind-turbine-driven DFIG. *Elektrotehniški vestnik*, 2018, vol. 85, no. 1-2, pp. 29-36. https://ev.fe.uni-lj.si/1-2-2018/Bouyekni.pdf.
20. Benbouhenni H., Boudjema Z., Belaidi A. Direct power control with NSTSM algorithm for DFIG using SVPWM technique. *Iranian Journal of Electrical & Electronic Engineering*, 2021, vol. 17, no. 1, pp. 1-11. doi: http://dx.doi.org/10.22068/IJEEE.17.1.1518.
21. Benbouhenni H., Boudjema Z., Belaidi A. DPC based on ANFIS super-twisting sliding mode algorithm of a doubly-fed induction generator for wind energy system. *Journal Européen des Systèmes Automatisés*, 2020, vol. 53, no. 1, pp. 69-80. doi: https://doi.org/10.18280/jesa.530109.
22. Tayebi-Haghighi S., Piltan F., Kim J.-M. Robust Composite High-Order Super-Twisting Sliding Mode Control of Robot Manipulators. *Robotics*, 2018, vol. 7, no. 1, p. 13. https://doi.org/10.3390/robotics7010013.

Received 22.04.2021
Accepted 31.05.2021
Published 27.08.2021

Habib Benbouhenni[1]*, Doctor of Electrical Engineering,*
Ahmed Driss[2]*, Doctor of Electrical Engineering,*
Soufiane Lemdani[3]*, Doctor of Electrical Engineering,*
[1] Department of Electrical & Electronics Engineering,
Nisantasi University, Istanbul, Turkey,
e-mail: habib.benbouenni@nisantasi.edu.tr (Corresponding author)
[2] Department of Electrical Engineering,
Ecole National Polytechnique School of Oran Maurice Audin,
LAAS Research Laboratory,
Oran, Algeria,
ENP-MA, Oran, Algeria,
e-mail: drisahmed82@yahoo.com
[3] Department of Electrical Engineering,
University of Science and Technology of Oran-Mohamed-Boudiaf, Oran, Algeria,
e-mail: lamdaniso@yahoo.fr

How to cite this article:
Benbouhenni H., Driss A., Lamdani S. Indirect active and reactive powers control of doubly fed induction generator fed by three-level adaptive-network-based fuzzy inference system – pulse width modulation converter with a robust method based on super twisting algorithms. *Electrical Engineering & Electromechanics*, 2021, no. 4, pp. 31-38. doi: https://doi.org/10.20998/2074-272X.2021.4.04.

UDC 629.374.7 https://doi.org/10.20998/2074-272X.2021.4.05

Y.O. Denisov, O.I. Denisov, O.O. Bursala

SYNTHESIS OF THE DIGITAL REGULATOR OF THE MAIN CONTOUR OF THE THREE-CIRCUIT SYSTEM OF THE LINEAR ELECTRIC DRIVE OF THE WORKING BODY OF THE MECHANISM OF ONBOARD AVIATION EQUIPMENT

Goal *The purpose of the article is to further develop analytical methods for calculating and synthesizing power electronics systems with deep pulse width modulation (PWM). A three-circuit linear electric drive system for positioning the working body of the mechanism of onboard aircraft equipment, in which the linear electric motor is controlled from a pulse width converter (PWC), is considered. The power converter is included in the current loop. It has a noticeable effect on the level of current ripple, travel speed and positioning accuracy of the operating mechanism of a linear electric drive.* ***Methodology****. To analyze the processes in the current loop, a discrete transfer function of a pulse-width converter for PWM in the final zone and «in the large» is obtained on the basis of the statistical linearization of the modulation characteristics of the multi-loop PWM model. The modulation characteristic of each circuit of the model is obtained as a result of the Fourier series expansion in Walsh functions of the output voltage of the PWM during the PWM process. Statistical linearization of modulation characteristics is performed based on Hermite polynomials.* ***Results.*** *During the analysis, discrete transfer functions of closed current loops, velocity and open loop position were obtained, for which a digital controller was synthesized in the form of a recursive filter.* ***Originality.*** *The parameters of the regulator links are found, which make it possible to complete the transient process in four PWC switching periods with an overshoot of no more than 6 %. The analysis of the speed-optimized positioning process of a linear electric drive based on the LED AT 605TU motor is carried out.* ***Practical significance****. The purpose of the analysis was to establish the relationship between the switching period of the PWM and the value of the uncompensated constant, at which the pulsations of the positioning process are minimal while ensuring the minimum overshoot and maximum speed. It was found that the specified requirements are satisfied by the ratio between the switching period, PWC and uncompensated constant in the range of one or two.* References 12, figures 4.
Key words: **linear electric drive, discrete transfer function, pulse width modulation, positioning error, optimal regulator.**

В триконтурній системі лінійного електроприводу, робочий орган якого реалізує поступальне переміщення при виконанні команди бортового комп'ютера літального апарату, врахований вплив пульсацій широтно-імпульсного перетворювача постійної напруги на процес позиціонування. З умови кінцевої тривалості процесу позиціонування синтезовано цифровий регулятор головного контуру системи і запропонована його реалізація у вигляді рекурсивного цифрового фільтру. Бібл. 12, рис. 4.
Ключові слова: **лінійний електропривод, дискретна передавальна функція, широтно-імпульсна модуляція, помилка позиціонування, оптимальний регулятор.**

В трехконтурной системе линейного электропривода, рабочий орган которого реализует поступательное перемещение при выполнении команды бортового компьютера летательного аппарата, учтено влияние пульсаций широтно-импульсного преобразователя постоянного напряжения на процесс позиционирования. Из условия конечной длительности процесса позиционирования синтезирован цифровой регулятор главного контура системы и предложена его реализация в виде рекурсивного цифрового фильтра. Библ. 12, рис. 4.
Ключевые слова: **линейный электропривод, дискретная передаточная функция, широтно-импульсная модуляция, ошибка позиционирования, оптимальный регулятор.**

Introduction. Problem definition in general. In the context of the problem of creating an electric aircraft [1] there is an important scientific and practical task – the replacement of onboard hydraulic and pneumatic drives that control the linear movement of the working bodies of the respective mechanisms, with their electrical counterparts based on linear or stepper motors. The main requirement for them is to ensure accurate positioning after the completion of the translational movement without hesitation.

The accuracy characteristics of a linear electric drive are affected by load changes and control discreteness, which causes ripples of the motor supply voltage.

At the stage of designing accurate positioning systems there is a problem of taking into account the influence of these factors on the dynamic characteristics: speed, over-regulation, stability, with their subsequent optimization.

Analysis of basic research and publications and problem definition. In [2] the general principles of construction of systems of the automated electric drive on the basis of usual and linear electric motors of a direct current are revealed. High requirements for the accuracy characteristics of linear electric drives for aviation, space technology, precise technological processes, due to the presence of a power converter with pulse width modulation (PWM) of the output voltage, complicate the procedure of analysis and synthesis of their dynamic characteristics with a given quality.

Therefore, in the known works devoted to the development of systems for these areas, the main attention is paid to their practical design based on the analysis of mechanical parts operation modes [3], programming of control controllers based on fuzzy logic [4-6] using experimental data. For example, the programming of the training controller for the positioning system of the machine feed with numerical control is performed on the basis of experimental amplitude-frequency characteristics [7]. Electronic modelling is widely used to study processes in linear electric drives with different types of loads [8-10].

It can be noted that the methods of theoretical analysis and synthesis of systems with deep PWM have not yet received their further development. They are based on the account of only a constant component, or taking into account the discreteness of regulation «in small», when systems with PWM are equivalent to systems with amplitude pulse modulation.

These methods do not allow to take into account the influence of pulsations of the supply voltage of a linear motor, which are a consequence of deep PWM, in the synthesis of dynamic characteristics of the positioning system with a given quality. There is an obvious problem that needs to be solved.

The goal of the work is to synthesize the digital regulator of the main circuit of the linear electric drive of the working body of the onboard aviation equipment mechanism, which provides a transient process of finite duration taking into account the effect of pulsation of the converter with PWM, which allows to increase positioning accuracy.

Presentation of the main material. Diagram shown in Fig. 1, consists of three circuits: current, speed, position.

The current circuit includes a current regulator, a link of current formation and a link of uncompensated time constant, which is determined by time constants of filters for smoothing current ripples. Their transfer functions, respectively:

$$K_{CC}(p) = K_{CS}\frac{1+p\cdot T_E}{p\cdot T_C};$$

$$K_{FC}(p) = \frac{1}{R_y\left(1+p\cdot T_E\right)};$$

$$K_{CT}(p) = \frac{1}{1+p\cdot\sigma},$$

where K_{CS} is the transfer coefficient of the proportional component; T_C is the integration constant of the current loop; T_E is the electric constant of the motor armature; R_y is the active resistance of the armature; σ is the uncompensated constant.

The source of current ripple is a pulse-width converter (PWC), which is powered by the onboard network of the aircraft. In Fig. 1 PWC is represented by a set of pulse element (PE) with gain K_{IE}, which is equal to one, and a forming element (FE), CS is a control system with gain K_{CK}. The influence of pulsations on the quality of the transient process of the positioning system in general can be taken into account using the transfer function of the PWC, which is a link in the current circuit.

In [11], as a result of the analysis of the voltage spectrum at the output of the PWC in the basis of orthogonal discrete Walsh functions, modulation characteristics were obtained that reflect the dependencies of the amplitudes of the spectral components on the duty cycle of regulation.

The transfer function of the PWC is found in the form of a vector. Its dimension is determined by the number of Walsh functions taken into account, which depends on the cutoff frequency of the system and the approximation error.

Component of the i-th vector of the transfer function of the link with PWM (forming element):

$$K^{i}{}_{pws}(q) = mK_i^{Wal}\frac{\exp\left(-\frac{i}{m}q\right)-\exp\left(-\frac{i+1}{m}\right)}{q}, \quad (1)$$

where m is the number of approximating functions; $K_i^{Wal} = 1$, if the pulse of the unit amplitude of a rectangular shape is modulated; $q = p\cdot T$, where T is the switching period of the PWC; $i = 0, 1, 2, \ldots m-1$ is the number of components of the vector of the transfer function with the range of change of duty cycle $i/m \le \gamma \le i+1/m$.

According to the results of statistical linearization of modulation characteristics based on Hermite polynomials, in [11] the transfer function of the PWM link for $0 \le \gamma \le 1$ was obtained, which, taking into account the four Walsh functions, has the following form:

$$K_{pws}(q) = \frac{K_{1C} - K_{kC}\sum_{k=2}^{5} e^{-0,25q(k-1)}}{q}, \quad (2)$$

where $K_{1C} = 1.086$; $K_{2C} = 0.114$; $K_{3C} = 0.280$; $K_{4C} = 0.246$; $K_{5C} = 0.446$ are the statistical linearization coefficients that correspond to the PWM of the pulse of a rectangular shape of unit amplitude on a unit period.

From (2) it is seen that due to the statistical linearization of the four modulation characteristics, the PWM «in large» is replaced by the equivalent amplitude-pulse modulation of the four-stage pulse. The amplitudes of the stages are determined by the corresponding coefficients of statistical linearization.

The speed circuit contains the link of formation of counter-EMF with transfer function

$$K_{FE}(p) = \frac{R}{p\cdot T_M},$$

where T_M is the electromechanical constant; and also the speed formation link with transmission factor $1/K_E$, where K_E is the coefficient of counter-EMF of the motor armature.

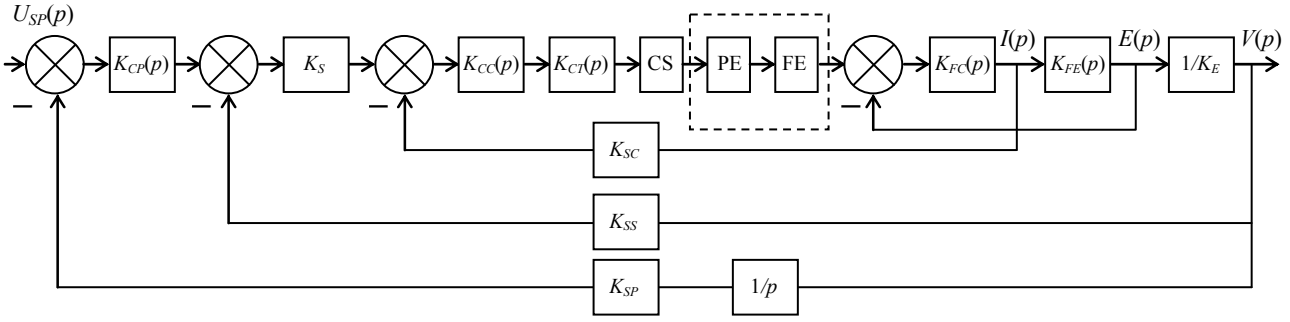

Fig. 1. Block diagram

The system circuits include sensors of: K_{SC} – current, K_{SS} – speed, K_{SP} – position, as well as the proportional regulator of the speed circuit with a gain K_S. Current and speed regulators are set to the modular optimum.

The structure and parameters of the digital controller of the main circuit (position) are subsequently obtained as a result of its optimization by the criterion of speed taking into account the ripples of the PWC.

Discrete transfer functions of positioning system circuits. Let's turn the bloc diagram (Fig. 1) into the diagram (Fig. 2) in which feedback on counter-EMF of the motor is not taken into account since $T_M >> T_C$ [11].

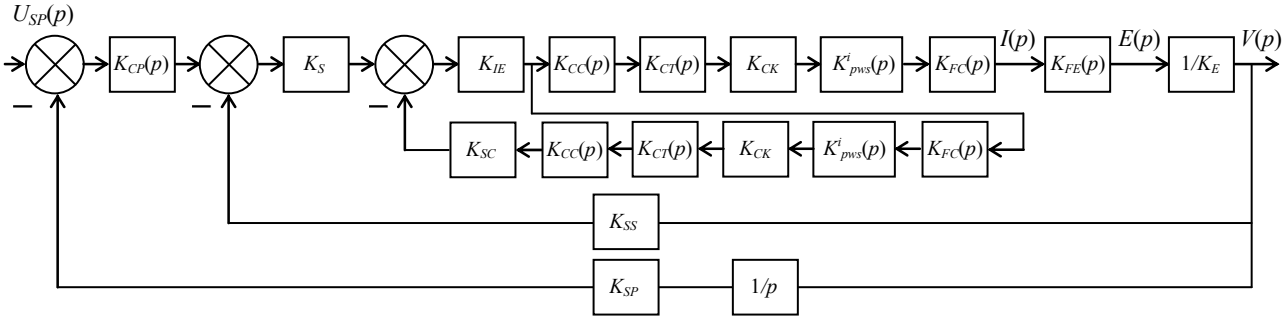

Fig. 2. Transformed diagram

a) Current circuit. Assume that the range of changes in the duty cycle of the regulation taking into account the four Walsh functions (m = 4) is in the zone i = 0, i.e. $0 \le \gamma \le 0.25$. Then, taking into account (1), the transfer function of the feedback circuit of the current loop is a modified z-transform:

$$W^*_{fb}(z,\varepsilon) = Z_M\left\{K_{sc}K_{cs}K_{CK}\frac{1+pT_E}{pT_C}\times \right.$$
$$\left.\times\frac{4\left(1-e^{-0,25pT}\right)}{p\left(1+p\,\sigma\right)}\frac{1}{R_y\left(1+pT_E\right)}\right\}.$$

As a result of the modified z-transform with the replacement of $p = q/T$, we obtain:

$$W^*_{fb}(z,\varepsilon) = K_{fb}\frac{F^*_{1c}(z,\varepsilon)}{\left(z-1\right)\left(z-e^{-\beta}\right)}, \qquad (3)$$

for range $0 \le \varepsilon \le 0.25$, where $K_{fb} = \dfrac{4K_{sc}K_{CK}T^2K_{cs}}{R_yT_C\sigma}$,

$$F^*_{1c}(z,\varepsilon) = A_1\left[\varepsilon\left(z-1\right)+0,25\right]\left(z-e^{-\beta}\right)+$$
$$+\left(z-1\right)\left[A_2\left(z-e^{-\beta}\right)+A_3e^{-\beta\varepsilon}\left(z-e^{-0,75\beta}\right)\right],$$
$$A_1=\frac{1}{\beta},\quad A_2=-\frac{1}{\beta^2},\quad A_3=\frac{1}{\beta^2},\quad \beta=\frac{T}{\sigma}.$$

For range $0.25 \le \varepsilon \le 1$

$$W^*_{fb}(z,\varepsilon) = K_{fb}\frac{F^*_{2c}(z,\varepsilon)}{\left(z-1\right)\left(z-e^{-\beta}\right)}, \qquad (4)$$

where

$$F^*_{2c}(z,\varepsilon) = z\left[0,25A_1\left(z-e^{-\beta}\right)+A_3e^{-\beta\varepsilon}\left(z-e^{0,25\beta}\right)\left(z-1\right)\right].$$

The left value of (4) is equal to the right value of the transfer function (3), i.e.:

$$W^*_{fb}(z,-0) = z^{-1}\lim_{\varepsilon\to 1}W^*_{fb}(z,\varepsilon) = W^*_{fb}(z,0) =$$
$$= K_{fb}\frac{0,25A_1\left(z-e^{-\beta}\right)+A_3e^{-\beta}\left(1-e^{0,25\beta}\right)\left(z-1\right)}{\left(z-1\right)\left(z-e^{-\beta}\right)}. \qquad (5)$$

This indicates that at the time of quantization, the transfer function does not contain jumps.

The transfer function of a closed current circuit for the diagram (Fig. 2)

$$W^*_{fbc}(z,0) = \frac{1}{1+W^*_{fb}(z,0)},$$

Taking into account (5) we have:

$$W^*_{fbc}(z,0) =$$
$$=\frac{\left(z-1\right)\left(z-e^{-\beta}\right)}{\left(z-1\right)\left(z-e^{-\beta}\right)+K_{fb}\left[0,25A_1\left(z-e^{-\beta}\right)+A_3e^{-\beta}\left(1-e^{0,25\beta}\right)\left(z-1\right)\right]}. \qquad (6)$$

b) Speed circuit. The transfer function of the part of the open speed circuit, which is obtained as a result of the transformation of the diagram (Fig. 1) into the diagram (Fig. 2), is obtained in the process of the following modified z-transform:

$$W^*_{cs}(z,\varepsilon) = Z_M\left\{K_{cs}\frac{1+pT_E}{pT_C}\cdot\frac{K_{CK}}{1+p\,\sigma}\times\right.$$
$$\left.\times\frac{4\left(1-e^{-0,25pT}\right)}{pK_ER_y\left(1+pT_E\right)}\frac{R_y}{pT_M}\right\}.$$

Let's make a replacement $p = q/T$ and obtain:

$$W^*_{cs}(z,\varepsilon) = Z_M\left\{K_{0s}\left(\frac{B_3}{q^3}+\frac{B_2}{q^2}+\frac{B_1}{q}+\frac{B_0}{q+\beta}\right)\times\right.$$
$$\left.\times\left(1-e^{-0,25q}\right)\right\},$$

where

$$K_{0s}=\frac{4K_{cs}K_{CK}T^3}{T_CK_ET_M\sigma},\ B_1=\frac{1}{\beta^3},\ B_2=-\frac{1}{\beta^2},\ B_3=\frac{1}{\beta},\ B_0=-\frac{1}{\beta^3}.$$

As a result of the modified z-transform for range $0 \le \varepsilon \le 0.25$ we have:

$$W^*_{cs1}(z,\varepsilon) = K_{0s}\frac{F^*_{ps1}(z,\varepsilon)}{2(z-1)^2\left(z-e^{-\beta}\right)}, \quad (7)$$

and for range $0.25 \le \varepsilon \le 1$ we have:

$$W^*_{cs2}(z,\varepsilon) = K_{0s}\frac{F^*_{ps2}(z,\varepsilon)}{2(z-1)^2\left(z-e^{-\beta}\right)}, \quad (8)$$

where

$$F^*_{ps1}(z,\varepsilon) = B_3\left[z^2\varepsilon^2 + z\left(0,44+0,5\varepsilon-2\varepsilon^2\right)-0,94\right]\times$$
$$\times\left(z-e^{-\beta}\right)+2B_2\left[z\varepsilon-\varepsilon-0,75\right](z-1)\left(z-e^{-\beta}\right)+$$
$$+2B_0e^{-\beta\varepsilon}\left(z-e^{-0,75\beta}\right)(z-1)^2+2B_1(z-1)^2\left(z-e^{-\beta}\right);$$

$$F^*_{ps2}(z,\varepsilon) = B_3\left[0,5z+z(z-1)(0,5\varepsilon-0,0625)\right]\times$$
$$\times\left(z-e^{-0,25\beta}\right)+B_2(z-1)\left(z-e^{-\beta}\right)z\cdot 0,5+$$
$$+2B_0ze^{-\beta\varepsilon}\left(1-e^{0,25\beta}\right)(z-1)^2.$$

From the transfer function (8) we have its left value:

$$W^*_{sc2}(z,-0) = z^{-1}\lim_{\varepsilon\to 1}W^*_{sc2}(z,\varepsilon) =$$
$$= K_{0s}\left[\frac{B_3(0,44z+0,22)\left(z-e^{-\beta}\right)}{2(z-1)^2\left(z-e^{-\beta}\right)}+\right. \quad (9)$$
$$\left.+\frac{B_2(z-1)\left(z-e^{-\beta}\right)+2B_0e^{-\beta}\left(1-e^{0,25\beta}\right)(z-1)^2}{2(z-1)^2\left(z-e^{-\beta}\right)}\right].$$

Open speed circuit transfer function for $0 \le \varepsilon \le 0.25$:

$$W^*_{ss1}(z,\varepsilon) = W^*_{fbc}(z,0)\cdot W^*_{cs1}(z,\varepsilon),$$

and for $0.25 \le \varepsilon \le 1$:

$$W^*_{ss2}(z,\varepsilon) = W^*_{fbc}(z,0)\cdot W^*_{cs2}(z,\varepsilon).$$

Closed circuit speed transfer function for $0 \le \varepsilon \le 0.25$:

$$W^*_{fbs1}(z,\varepsilon) = \frac{W^*_{ss1}(z,\varepsilon)}{1+W^*_{fbc}(z,0)\cdot W^*_{cs2}(z,-0)},$$

and for $0.25 \le \varepsilon \le 1$:

$$W^*_{fbs2}(z,\varepsilon) = \frac{W^*_{ss2}(z,\varepsilon)}{1+W^*_{fbc}(z,0)\cdot W^*_{cs2}(z,-0)}.$$

c) Position circuit. The transfer function of the open position circuit:

$$W^*_{fbp1}(z,\varepsilon) = W^*_{fbs1}(z,\varepsilon)\cdot\frac{K_{sp}z}{z-1}, \quad 0 \le \varepsilon \le 0.25;$$

$$W^*_{fbp2}(z,\varepsilon) = W^*_{fbs2}(z,\varepsilon)\cdot\frac{K_{sp}z}{z-1}, \quad 0.25 \le \varepsilon \le 1.$$

Taking into account (6)-(9) after the corresponding transformations we have the transfer functions of the position circuit in the open state:

$$W^*_{fbp1}(z,\varepsilon) = K_0\times$$
$$\times\frac{z^4a_{13}(\varepsilon)+z^3a_{12}(\varepsilon)+z^2a_{11}(\varepsilon)+za_{10}(\varepsilon)}{(z-1)\left[z^3b_3(1)+z^2b_2(1)+zb_1(1)+b_0(1)\right]}, \quad (10)$$

for $0 \le \varepsilon \le 0.25$;

$$W^*_{fbp2}(z,\varepsilon) = K_0\times$$
$$\times\frac{z^4a_{23}(\varepsilon)+z^3a_{22}(\varepsilon)+z^2a_{21}(\varepsilon)+za_{20}(\varepsilon)}{(z-1)\left[z^3b_3(1)+z^2b_2(1)+zb_1(1)+b_0(1)\right]}, \quad (11)$$

where $0,25 \le \varepsilon \le 1$,

$$K_0 = K_{0i}K_{sp};$$

$$a_{13}(\varepsilon) = B_3\varepsilon^2+2B_2\varepsilon+2B_1+2B_0e^{-\beta\varepsilon};$$

$$a_{12}(\varepsilon) = B_3\left(0,44+0,5\varepsilon-2\varepsilon^2-\varepsilon^2\cdot e^{-\beta}\right)+$$
$$+2B_2\left[0,25-\varepsilon-\varepsilon\left(1+e^{-\beta}\right)\right]-2B_1\left(2+e^{-\beta}\right)-$$
$$-2B_0\left(2+e^{-0,75\beta}\right)e^{-\beta\varepsilon};$$

$$a_{11}(\varepsilon) = B_3\left[0,06+\varepsilon^2-0,5\varepsilon-e^{-\beta}\left(0,44+0,5\varepsilon-2\varepsilon^2\right)\right]+$$
$$+2B_2\left[\varepsilon\left(1+e^{-\beta}\right)-0,25\left(1+e^{-\beta}\right)+\varepsilon\cdot e^{-\beta}\right]+$$
$$+2B_1\left(1+2e^{-\beta}\right)+2B_0\left(1+2e^{-0,75\beta}\right)e^{-\beta\varepsilon};$$

$$a_{10}(\varepsilon) = B_3\left[-e^{-\beta}\left(0,06+\varepsilon^2-0,5\varepsilon\right)\right]+$$
$$+2B_2\left(-\varepsilon e^{-\beta}+0,25e^{-\beta}\right)-2B_1e^{-\beta}-2B_0e^{-\beta(\varepsilon+0,75)};$$

$$b_3(1) = 2\left(1+K_{0c}A_3e^{-\beta}\right);$$

$$b_2(1) = K_{0c}\left(0,5A_1-6A_3e^{-\beta}\right)+K_{0s}\left(0,45B_3+B_2\right)-2e^{-\beta};$$

$$b_1(1) = 2\left(1+2e^{-\beta}\right)+$$
$$+K_{0s}\left[B_3\left(0,05-0,45e^{-\beta}\right)-B_2\left(1+e^{-\beta}\right)\right]+$$
$$+K_{0c}\left[6A_3e^{-\beta}-0,5A_1\left(1+e^{-\beta}\right)\right];$$

$$b_0(1) = K_{0c}\left(0,5A_1e^{-\beta}-2A_3e^{-\beta}\right)-$$
$$-K_{0s}\left(0,05B_3e^{-\beta}-B_2e^{-\beta}\right)-2e^{-\beta};$$

$$a_{23}(\varepsilon) = B_3\left(0,5\varepsilon-0,22\right)+2B_0e^{-\beta\varepsilon}\left(1-e^{-0,25\beta}\right)+B_2\cdot 0,5;$$

$$a_{22}(\varepsilon) = B_3\left[0,0625-0,5\left(1+e^{-\beta}\right)\varepsilon+0,0625e^{-\beta}\right]-$$
$$-B_2\left(1+e^{-\beta}\right)-4B_0e^{-\beta\varepsilon}\left(1-e^{0,25\beta}\right);$$

$$a_{21}(\varepsilon) = 2B_0e^{-\beta\varepsilon}\left(1-e^{-0,25\beta}\right)+$$
$$+0,5B_2e^{-\beta}-B_3\left(0,5625-0,5\varepsilon\right);$$

$$a_{20}(\varepsilon) = 0.$$

Synthesis of digital position circuit controller. The purpose of the synthesis is to ensure the final duration of the transient process in the positioning circuit with minimal over-regulation. To do this, we use the most general, the second polynomial equation of synthesis [11].

We present the transfer functions of the open position circuit as follows:

$$W^*_{fbp1}(z,\varepsilon)=\frac{P^*_1(z,\varepsilon)}{(z-1)Q^*_1(z)} \text{ for } 0\le\varepsilon\le 0.25;$$

$$W^*_{fbp2}(z,\varepsilon)=\frac{P^*_2(z,\varepsilon)}{(z-1)Q^*_1(z)} \text{ for } 0.25\le\varepsilon\le 1,$$

where

$$P^*_1(z,\varepsilon)=$$
$$=K_0\left[a_{13}(\varepsilon)z^4+a_{12}(\varepsilon)z^3+a_{11}(\varepsilon)z^2+a_{10}(\varepsilon)z\right], \quad (12)$$

$$P^*_2(z,\varepsilon)=K_0\left[a_{23}(\varepsilon)z^4+a_{22}(\varepsilon)z^3+a_{21}(\varepsilon)z^2\right], \quad (13)$$

$$Q^*_1(z)=z^3b_3(1)+z^2b_2(1)+zb_1(1)+b_0(1). \quad (14)$$

Minimum duration of the transient process:

$$S_{\min}=l_Q+r-r_0,$$

where l_Q are the degrees of denominators (10), (11), $r_0 = 1$ is the own astatism of the position circuit, $r = 1$ is its astatism according to the results of the synthesis procedure. Therefore, $S_{\min} = 4$.

For a stable continuous part of the positioning circuit at ranges $0 \le \varepsilon \le 0.25$ and $0.25 \le \varepsilon \le 1$ the following relation is true:

$$P^*(z,0)\cdot M^*(z,0)+(z-1)^r N^*(z,0)=z^4, \quad (15)$$

where $M^*(z,0)=C_0$ is the polynomial of the degree $l_M = r - 1=0$,

$$N^*(z,0)=d_4z^4+d_3z^3+d_2z^2+d_1z+d_0 \quad (16)$$

is the polynomial of the degree $l_N \ge l_P$, where $l_p = 4$ is the degree of $P_1^*,(z,e)$.

As a result (15) takes the form:

$$C_0K_0\left[a_{13}(0)z^4+a_{12}(0)z^3+a_{11}(0)z^2+a_{10}(0)z\right]+$$
$$+(z-1)\left(d_4z^4+d_3z^3+d_2z^2+d_1z+d_0\right)=z^4. \quad (17)$$

We equate the coefficients of the same degrees z, and from (17) obtain:

$$C_0=\frac{1}{K_0A_n(0)},$$

where

$$A_n(0)=\sum_0^3 a_{1n}(0), \quad d_0=0, \quad d_1=\frac{a_{10}(0)}{A_n(0)},$$

$$d_2=\frac{a_{10}(0)+a_{11}(0)}{A_n(0)}, \quad d_3=\frac{\sum_0^2 a_{1n}(0)}{A_n(0)}, \quad d_4=0.$$

As a result we have:

$$N^*(z,0)=z^3\frac{\sum_0^2 a_{1n}(0)}{A_n(0)}+z^2\frac{\sum_0^1 a_{1n}(0)}{A_n(0)}+z\frac{a_{10}(0)}{A_n(0)}. \quad (18)$$

The transfer function of the series-activated optimal controller:

$$K^*_{ocp}(z,0)=\frac{Q^*_1(z)\cdot M^*(z,0)}{(z-1)^{r-r_0}\cdot N^*(z,0)}.$$

Taking into account (14), (16), (18) we obtain:

$$K_{ocp}{}^*(z,0)=\frac{z^3b_3(1)+z^2b_2(1)+zb_1(1)+b_0(1)}{K_0\left[z^3\sum_0^2 a_{1n}(0)+z^2\sum_0^1 a_{1n}(0)+za_{10}(0)\right]}. \quad (19)$$

Divide the numerator and denominator of (19) by $K_0\sum_0^2 a_{1n}(0)$ and obtain:

$$K_{ocp}{}^*(z,0)=\frac{z^{-1}\mu_0+\mu_1z^{-2}+\mu_3z^{-3}+\mu_4z^{-4}}{1+\alpha_1z^{-1}+\alpha_2z^{-2}}=$$
$$=\frac{\Delta U_{OUT}{}^*[z,0]}{\Delta U_{IN}{}^*[z,0]}, \quad (20)$$

where

$$\mu_0=\frac{b_3(1)}{K_0\sum_0^2 a_{1n}(0)}, \quad \mu_1=\frac{b_2(1)}{K_0\sum_0^2 a_{1n}(0)}, \quad \mu_2=\frac{b_1(1)}{K_0\sum_0^2 a_{1n}(0)},$$

$$\mu_3=\frac{b_0(1)}{K_0\sum_0^2 a_{1n}(0)}, \quad \alpha_1=\frac{\sum_0^1 a_{1n}(0)}{\sum_0^2 a_{1n}(0)}, \quad \alpha_2=\frac{a_{10}(0)}{\sum_0^2 a_{1n}(0)}.$$

From (20) we found that:

$$\Delta U_{OUT}{}^*[z,0]=\Delta U_{IN}{}^*[z,0]\sum_1^3\mu_kz^{-k}-\Delta U_{OUT}{}^*[z,0]\sum_1^2\alpha_kz^{-k}.$$

The obtained z-image $\Delta U_{OUT}{}^*[z, 0]$ corresponds to the original of the difference equation:

$$\Delta U_{OUT}{}^*[nT]=$$
$$=\sum_1^3\mu_k\Delta U_{IN}{}^*\left[(n-k)T\right]-\sum_1^2\alpha_k\Delta U_{OUT}{}^*\left[(n-k)T\right]. \quad (21)$$

The difference equation (21) is solved by a digital recursive filter (Fig. 3), which contains four delay links for one period of switching of the PWC and amplifiers in the forward and reverse transmissions with gains μ_k, α_k. Implementation of a digital filter is possible on the basis of a programmable microcontroller.

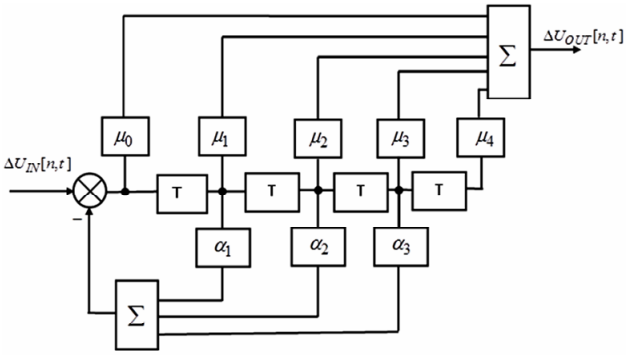

Fig. 3. Block diagram of the position regulator

Transient process analysis in an optimized positioning system. When the optimal synthesized controller is included in the position circuit, the optimal transfer functions of the closed positioning system for ranges of the current parameter ε values:

$$W^*_{1,2\,fbp}(z,\varepsilon)=P^*_{1,2}(z,\varepsilon)\frac{M^*(z,0)}{z^4}.$$

Taking into account (12), for $0\le\varepsilon\le 0.25$ we have:

$$W^*_{1\,fbp}=\frac{a_{13}(\varepsilon)z^4+a_{12}(\varepsilon)z^3+a_{11}(\varepsilon)z^2+a_{10}(\varepsilon)z}{A_n(0)\cdot z^4}. \quad (22)$$

Similarly, taking into account (13), it is possible to obtain the optimal transfer function of the closed positioning system for $0.25\le\varepsilon\le 1$.

Image of the transient characteristics of the positioning system:

$$H_{1,2}{}^*\left[z,\varepsilon\right]=\frac{z}{z-1}W^*{}_{fbp}(z,\varepsilon).$$

Taking into account (22) we have:

$$H^*{}_1(z,\varepsilon)=\frac{1}{A_n(0)}\left[a_{13}(\varepsilon)\frac{z}{z-1}+\right.$$

$$\left.+a_{12}(\varepsilon)\frac{1}{z-1}+a_{11}(\varepsilon)\frac{1}{z(z-1)}+a_{10}(\varepsilon)\frac{1}{z^2(z-1)}\right].$$

The image of the transient characteristic for the values $0\le\varepsilon\le 0.25$ corresponds to the original:

$$H^*{}_1(n,\varepsilon)=\frac{1}{A_n(0)}\left[a_{13}(\varepsilon)+\right.$$
$$\left.+a_{12}(\varepsilon)\left[n-1\right]+a_{11}(\varepsilon)\left[n-2\right]+a_{10}(\varepsilon)\left[n-3\right]\right]. \quad (23)$$

Similarly, it is possible to obtain the transition characteristic $H^*_2(n, \varepsilon)$ for the values $0.25\le\varepsilon\le 1$.

From expression (23) it is seen that in the system optimized by the criterion of speed of the system the transient positioning process is completed in four periods of switching of the PWC. The optimization process begins with a delay of zero period, during which the system is open due to the fact that the feedback signal appears with a delay of one period.

For the positioning system, which is made on the basis of the linear motor LED AT605TU, the transient characteristics for different values of $\beta = T/\sigma$ are calculated. Linear motor parameters: $T_E = 5\cdot10^{-3}$ s, $T_M = 0.1$ s, $R_y = 3$ Ω, $K_E = 10.38$ V·s/m. Transmission coefficients of sensors of circuits of positioning system: $K_{SC} = 15$ V/A, $K_{SS} = 20$ V·s/m, $K_{SP} = 200$ V/m.

The parameters of current and speed regulators are obtained from the condition of setting these circuits to the modular optimum: $K_{CS}=\frac{T_C R_y}{2K_{sc}\sigma}$, $K_S=\frac{K_E T_M}{4R_y K_{ss}\sigma}$.

To minimize current ripple, in [12], it is shown $T_C \ge 2\ \sigma$. In further calculations $\sigma = 10^{-4}$ s, which determined the following gains: $K_{CC} = 0.2$; $K_{CS} = 43$; $K_{OC} = 2$; $K_{OS} = 0.17\cdot10^{-2}$; $K_O = 0.34$.

According to (23) for different values of β transient characteristics of the positioning system are calculated. The results are presented in Fig. 4.

For $\varepsilon = 0.25$, the steady-state values of the deviation of the transient characteristic at the switching period $H^*_c[0.25]$ are calculated. Their difference with the steady-state values of the transient characteristic at the time of operation of the pulse element determines the maximum relative values of the pulsations of the stabilized parameter, i.e. $\Delta^*_c = H^*_c[0{,}25]–1$.

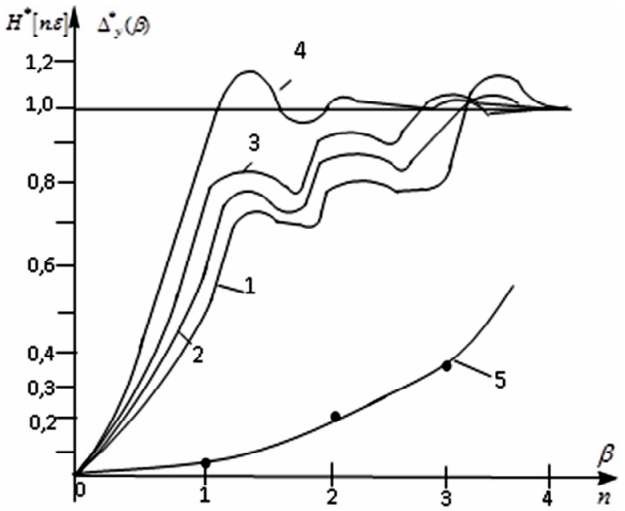

Fig. 4. Transient characteristics of the positioning system: curves 1-4 – for $\beta = 0.5$; 1; 2; 4, curve 5 – the dependence of the maximum pulsations on β in the steady state – $\Delta^*_{max}(\beta)$

The results of the calculation of $\Delta^*_c(\beta)$ are presented in Fig. 4 by curve 5. Obviously, a decrease in β leads to a decrease in ripple, but this reduces the speed of the transient process and increases the overregulation: curve 1 in Fig. 4.

Excessive increase in β leads to an increase in ripples, which negatively affects also the nature of the transient process. From the curves presented in Fig. 4, it is seen that the compromise between the quality of the transient process and the value of the ripples corresponds to $\beta = 1\div2$.

For one such compromise value, $\beta = 1$, the parameters of the links of the optimal position circuit regulator are calculated: $\mu_0 = 32.3$; $\mu_1 = –37.9$; $\mu_2 = 72.6$; $\mu_3 = –17$; $\alpha_1 = 0.5$; $\alpha_2 = 0.1$.

The obtained values of the parameters of the optimal speed digital position controller allow to realize the transient characteristic 2 (Fig. 4), for four intervals of switching of the PWC at relative values of ripples at the level of 0.04.

Curves 2, 3 in Fig. 4 shows that the transient processes that correspond to the recommended values $\beta = 1\div2$, accompanied by a slight over-regulation, which can be eliminated by increasing their duration, which is possible by increasing the degree of the polynomial (16).

Conclusions and prospects for development.

1. The transfer functions of PWC which allow to estimate ripples of the parameter stabilizing at deep regulation in transient and constant modes are proposed.

2. For the final range of change of duty cycle in the process of PWM the regulator of a position circuit is synthesized and its implementation in the form of the digital recursive filter which allows to complete transient process for four periods of switching of the PWC at the minimum overregulation is proposed.

3. It is established that the compromise between the quality indicators of the transient process and the

minimum of ripples of the stabilized parameter (position) corresponds to the values $\beta = 1 \div 2$.

The obtained results of estimating the influence of β on the nature of the transient process and the value of the ripples of the positioning system correspond to the transfer function (1), which is valid for a limited range of regulation. The transfer function (2) reflects the equivalent between the depth of the PWM and the amplitude pulse modulation of the multistage pulse. Based on it, it is possible to establish the pattern of ripple changes in the entire PWM range and, taking this into account, adjust the positioning circuit controller to the final duration of the process, which requires separate consideration.

Obtaining of the transfer function of the link with PWM «in large» taking into account the nonlinearities of the modulation characteristics of the model is possible. To do this, it is necessary to use a multidimensional *z*-transform and Volterra series to separate the linear and nonlinear components of the response of the link to the perturbation.

Conflict of interest. The authors declare no conflict of interest.

REFERENCES

1. Levyn A.V., Alekseev I.I., Kharytonov S.A., Kovalev L.K. *Elektricheskii samolet: ot idei do realizatsii* [Electric aircraft: from idea to implementation]. Moscow, Mashynostroenye Publ., 2010. 288 p. (Rus).

2. Belov M.P., Novikov V.A., Rassudov L.N. *Avtomatizirovannyi elektroprivod tipovykh proizvodstvennykh mekhanizmov i tekhnologicheskikh kompleksov* [Automated electric drive of standard production mechanisms and technological complexes]. Moscow, Academy Publ. Center, 2007. 576 p. (Rus).

3. Sun G., Wu L., Kuang Z., Ma Z., Liu J. Practical tracking control of linear motor via fractional-order sliding mode. *Automatica*, 2018, vol. 94, pp. 221-235. doi: https://doi.org/10.1016/j.automatica.2018.02.011.

4. Bani Melhem M.K., Simic M., Lai C.Y., Feng Y., Ding S. Fuzzy control of the dual-stage feeding system consisting of a piezoelectric actuator and a linear motor for electrical discharge machining. *Proceedings of the Institution of Mechanical Engineers, Part B: Journal of Engineering Manufacture*, 2019, vol. 234, no. 5, pp. 945-955. doi: https://doi.org/10.1177/0954405419889201.

5. Nagaraju N., Venkatesu S., Ujwala N.G. Optimization of Process Parameters of EDM Process Using Fuzzy Logic and Taguchi Methods for Improving Material Removal Rate and Surface Finish. *Materials Today: Proceedings*, 2018, vol. 5, no. 2, pp. 7420-7428. doi: https://doi.org/10.1016/j.matpr.2017.11.413.

6. Hendrawan Y.M., Farrage A., Uchiyama N. Iterative NC program modification and energy saving for a CNC machine tool feed drive system with linear motors. *The International Journal of Advanced Manufacturing Technology*, 2019, vol. 102, no. 9-12, pp. 3543-3562. doi: https://doi.org/10.1007/s00170-019-03390-1.

7. Mo J.-S., Qiu Z.-C., Wei J.-Y., Zhang X.-M. Adaptive positioning control of an ultrasonic linear motor system. *Robotics and Computer-Integrated Manufacturing*, 2017, vol. 44, pp. 156-173. doi: https://doi.org/10.1016/j.rcim.2016.08.011.

8. Bondar R.P., Podoltsev A.D. Operating modes of a linear permanent magnet motor as an element of vibration system. *Pratsi Instytutu Electrodynamiky NAN Ukrainy*, 2019, no. 54, pp. 52-62. (Ukr). doi: https://doi.org/10.15407/publishing2019.54.052.

9. Podoltsev A.D., Bondar R.P. Modeling of coupled electromechanical and thermal processes in a linear permanent magnet motor based on the multiphysics circuit theory. *Technical Electrodynamics*, 2020, no. 2, pp. 50-55. (Ukr). doi: https://doi.org/10.15407/techned2020.02.050.

10. Bondar R.P. Research of the magnetoelectric linear oscillatory motor characteristics during operation on elastoviscous loading. *Electrical Engineering & Electromechanics*, 2019, no. 1, pp. 9-16. doi: https://doi.org/10.20998/2074-272x.2019.1.02.

11. Denysov A.I., Zvolinskyi V.M., Rudenko Yu.V. *Ventil'nye preobrazovateli v sistemakh tochnoi stabilizatsii* [Valve converters in precision stabilization systems]. Kyiv, Naukova Dumka Publ., 1997. 249 p. (Rus).

12. Bashinskyi V., Shapovalov O., Denisov A., Bursala O., Bursala A. Influence of pulsations of the flexible dc motor on the management process of starting the gas turbine motor helicopter. *Technical Electrodynamics*, 2020, no. 2, pp. 56-66. (Ukr). doi: https://doi.org/10.15407/techned2020.02.056.

Received 06.05.2021
Accepted 22.06.2021
Published 27.08.2021

Y.O. Denisov[1], *Doctor of Technical Science, Professor,*
O.I. Denisov[2], *Doctor of Technical Science, Professor,*
O.O. Bursala [2], *Master Student*
[1] Chernihiv Polytechnic National University,
95, Shevchenko Str., Chernihiv, 14035, Ukraine,
e-mail: den71ltd@gmail.com (Corresponding author)
[2] State Scientific Research Institute of Armament and Military Equipment Testing and Certification,
1, Striletska Str., Chernigiv, 14033, Ukraine,
e-mail: den39ltd@gmail.com,
elena.burs1964@gmail.com

How to cite this article:
Denisov Y.O., Denisov O.I., Bursala O.O. Synthesis of the digital regulator of the main contour of the three-circuit system of the linear electric drive of the working body of the mechanism of onboard aviation equipment. *Electrical Engineering & Electromechanics*, 2021, no. 4, pp. 39-45. doi: https://doi.org/10.20998/2074-272X.2021.4.05.

UDC 621.317.3 https://doi.org/10.20998/2074-272X.2021.4.06

V.O. Brzhezitsky, Y.O. Haran, A.O. Derzhuk, O.R. Protsenko, Y.O. Trotsenko, M.M. Dixit

ULTIMATE EFFECT OF NON-IDENTITY OF CAPACITIVE ELEMENTS OF HIGH-VOLTAGE ARM ON FREQUENCY CHARACTERISTICS OF VOLTAGE DIVIDER (ANALYTICAL RESEARCH)

Purpose. *Determination in the analytical form of the maximum limiting influence of the non-identity of the capacitive elements of the high-voltage arm on the amplitude-frequency characteristic and phase-frequency characteristic of the voltage divider with parallel-series connection of R-, C-elements of the high-voltage arm.* ***Methodology****. Based on the previously developed theory of broadband voltage dividers with parallel-series connection of R-, C-elements, analytical expressions for amplitude-frequency and phase-frequency characteristics of the voltage divider are obtained and investigated taking into account the limit case of non-identical capacitive elements of high-voltage arm.* ***Results****. The nature of the dependencies of the frequency characteristics of the broadband voltage divider on the value of the tolerance of the capacitive elements of the high-voltage arm, the division factor of the voltage divider in a wide range of frequency changes is determined. Simplified approximating expressions for the maximum values of frequency characteristics of the voltage divider are proposed and their error is determined.* ***Originality****. For the first time in the analytical form the limiting influence of non-identity of capacitive elements of a high-voltage arm of a voltage divider on its frequency characteristics is considered. A mathematical model of this influence is constructed and the limit values of frequency characteristics of the voltage divider are determined.* ***Practical value.*** *It is recommended to introduce into the normative documentation of broadband voltage dividers the corrected value of the division factor, which allows to significantly reduce the deviation of the actual value of the division factor of the voltage divider from the normalized value in a wide range of frequency changes.* References 13, tables 2, figures 3.

Key words: **voltage divider, frequency characteristics, analytical expressions, tolerance of capacitive elements, parameters adjustment.**

На основі раніше розвинутої теорії широкосмугових подільників напруги з паралельно-послідовним з'єднанням R-, C-елементів вперше одержані аналітичні вирази для амплітудно-частотної та фазо-частотної характеристик подільника напруги з урахуванням граничного випадку неідентичності ємнісних елементів високовольтного плеча. Визначений загальний характер залежностей частотних характеристик від значення допуску ємнісних елементів, коефіцієнта ділення подільника напруги в широкому діапазоні зміни частоти. Запропоновані спрощені апроксимуючі вирази для максимальних значень частотних характеристик та визначена їх похибка. Рекомендовано уведення в нормативну документацію широкосмугових подільників напруги відкоригованого значення коефіцієнта ділення. Бібл. 13, табл. 2, рис. 3.

Ключові слова: **подільник напруги, частотні характеристики, аналітичні вирази, допуск ємнісних елементів, коригування параметрів.**

На основе ранее развитой теории широкополосных делителей напряжения с параллельно-последовательным соединением R-, C-элементов впервые получены аналитические выражения для амплитудно-частотной и фазо-частотной характеристик делителя напряжения с учетом предельного случая неидентичности ёмкостных элементов высоковольтного плеча. Определен общий характер зависимостей частотных характеристик от значения допуска ёмкостных элементов, коэффициента деления делителя напряжения в широком диапазоне изменения частоты. Предложены упрощенные аппроксимирующие выражения для максимальных значений частотных характеристик и определены их погрешности. Рекомендуется введение в нормативную документацию широкополосных делителей напряжения откорректированного значения коэффициента деления. Библ. 13, табл. 2, рис. 3.

Ключевые слова: **делитель напряжения, частотные характеристики, аналитические выражения, допуск ёмкостных элементов, корректировка параметров.**

Introduction. Instantaneous voltage values of high-voltage power systems and their changes over time are one of the most important arrays of information about the state and characteristics of such systems (it should be noted that such an array is constantly changing). Decades or more ago, electromagnetic voltage transformers were used (and are still used) to obtain information on high voltage values (there are even DC «voltage transformers»). This is due to the fact that the controls of such systems used relay devices connected to the output circuits of voltage transformers. The operation of such relay devices is focused on tracking steady (or close to them) modes of power systems. The needs of the current stage of power engineering development require the transition to the use of voltage dividers of various types instead of voltage transformers, and here the additional advantage of voltage dividers is the ability to obtain information not only for steady but also for instantaneous transient voltage values (which is important for control systems improvement). However, the transition to the widespread use of voltage dividers requires additional research, including those proposed in this article.

At the National Technical University of Ukraine «Igor Sikorsky Kyiv Polytechnic Institute» systematic studies of high-voltage dividers have been conducted since 1985. The essence of these studies is that for both AC systems and new DC systems, it is necessary to record instantaneous voltage values, because, for example, for AC systems, transient modes of automatic reconnection, switching and lightning surges, etc. are also important. For DC systems due to the imperfection of rectifiers and inverters, as well as filters, the presence of high voltage ripple (not to mention the importance of recording transients and overvoltages) will be

characterized. Therefore, for both AC and DC systems, it is important to create broadband high-voltage dividers. And in this sense, high-voltage dividers can be unified for both AC and DC systems, which will significantly reduce their cost and increase their availability.

In most cases, the high-voltage arm of broadband voltage dividers consists of a large number of parallel-series connections of *R*-, *C*- elements, which, in general, are not the same (identical). Taking into account the non-identity of *R*-, *C*- elements of the high-voltage arm is a characteristic feature of the above studies.

This article shows the importance of taking into account the possible non-identity of the capacitive elements of the high-voltage arm of broadband voltage dividers, demonstrates its calculated definition, and provides recommendations for significantly reducing its negative impact, which is an urgent problem.

Review of publications. In the modern concept of «digital substation» there is no need to use traditional relay elements of control systems, as signal processing of voltage and current channels will take place according to the scheme «analog value sensor → analog-to-digital converter → digital information processing system». In this case, the existing voltage transformers with high cost of insulating and magnetic materials can be replaced by high-voltage broadband voltage dividers [1]. In this regard, recent publications on high-voltage dividers have paid considerable attention to improving the accuracy of mathematical models, the stability of their parameters, taking into account various factors, features of metrological calibration and standardization of voltage dividers. Thus, in [2] it is reported to confirm the change in the division factor of the reference DC voltage divider in the range of 100-1000 kV in the amount of $2.5 \cdot 10^{-6}$ (2.5 ppm). In [3] it is stated about the change of up to 158.4 ppm of the division factor of the voltage divider «500 kV/2 mA» DC in an environment with temperature of 35 °C depending on the duration of operation of the divider in the range of 30-200 minutes. In [4] it is shown that the DC voltage divider up to 1000 kV must have a bandwidth of at least 10 kHz. Publications [5, 6] are devoted to the creation of real designs of broadband voltage dividers, while in [5] the frequency «response» of the divider according to the substitution scheme is calculated, and in [6] it is established experimentally using an inductive voltage divider. In [7] it is shown that the capacitive «commercial» voltage divider of 22 kV significantly changes its characteristics after 18 hours of continuous operation. In [8] a method of calibration of an industrial AC voltage divider at the level of 400 kV was developed, and the components of the method uncertainty have the following values: on the division factor ±0.26 %; on the phase angle $\pm 3.6 \cdot 10^{-3}$ rad. In [9], the characteristics of the measuring system of the pulse voltage divider with parallel-series connection of *R*-, *C*- elements of the high-voltage arm, designed to measure the aperiodic switching pulse up to 400 kV, are calculated. The considered substitution circuits of different types of high-voltage dividers have shielded parallel-series connections of *R*-, *C*- elements of a high-voltage arm, «typed», as a rule, with identical values of elements.

An additional advantage of high-voltage dividers is the ability to achieve the unique property of providing a constant value of their amplitude-frequency response in the range from zero to megahertz frequencies, which allows to equally record voltage signals from DC to bursts of short-term pulses [10]. However, this property of voltage dividers can be significantly devalued by the influence of non-identity of real values of R_{RV}-, C_{RV}-elements [10] of their high-voltage arm (deviation of R_{RV}, C_{RV} from nominal values R_N, C_N).

Since the creation of high-voltage dividers requires a significant number of *R*-, *C*- elements of the high-voltage arm (from tens to thousands), there is a need to use their less expensive series, which are usually characterized by significant tolerance (normalized deviation of R_{RV}, C_{RV} from R_N, C_N). The tolerance values for resistors $\Delta_R = (R_{RV} - R_N)/R_N$ and for capacitors $\Delta_C = (C_{RV} - C_N)/C_N$ differ significantly: for resistors Δ_R has a value of the order of ±0.01 (±1 %), and for capacitors Δ_C reaches ±0.2 (±20 %).

It matters how R_{RV}, C_{RV} are distributed within the tolerance:

$$R_N(1-\Delta_R)...R_N(1+\Delta_R)\ ;\ C_N(1-\Delta_C)...C_N(1+\Delta_C)\ .$$

The distribution law of R_{RV}, C_{RV} within the tolerance can be: triangular [11], rectangular, and others (parabolic, etc.). The influence of non-identity of high-voltage arm elements on the characteristics of the voltage divider depends both on the limit values Δ_R, Δ_C for high-voltage arm elements and on the distribution law of R_{RV}, C_{RV} within the respective intervals.

Therefore, **the goal of the article** is to determine in analytical form the maximum limiting influence of non-identical capacitive elements of the high-voltage arm on the amplitude-frequency characteristic (frequency response) and phase-frequency characteristic of the voltage divider with parallel-series connection of *R*-, *C*- elements.

From consideration of the theory of broadband voltage dividers [1] it follows that this case corresponds to the limiting discrete distribution of the elements of the high-voltage arm, when half of its capacitive elements has the value: $C' = C_N(1-\Delta_C)$, and the other half: $C'' = C_N(1+\Delta_C)$.

In this formulation, the calculation of the frequency characteristics of the high-voltage broadband voltage divider was performed in [12] using separate examples of frequency response and phase-frequency characteristic (PFC) at different values of Δ_C, but the general features of the frequency characteristics of broadband voltage dividers were not described.

Research methodology. The substitution circuit of the high-voltage divider for the case considered in [10] is presented in Fig. 1.

The influence of non-identity of *R*-elements of the high-voltage arm is neglected, because usually $\Delta_R << \Delta_C$. Below, the index «*C*» in the notation Δ_C is omitted, therefore $\Delta_C \equiv \Delta$, and $R_1 = R_2 = \ldots = R_n = R$.

According to the general theory of broadband voltage dividers [1], the expressions *A* for the frequency response and φ for PFC of the voltage divider in Fig. 1 can be represented as:

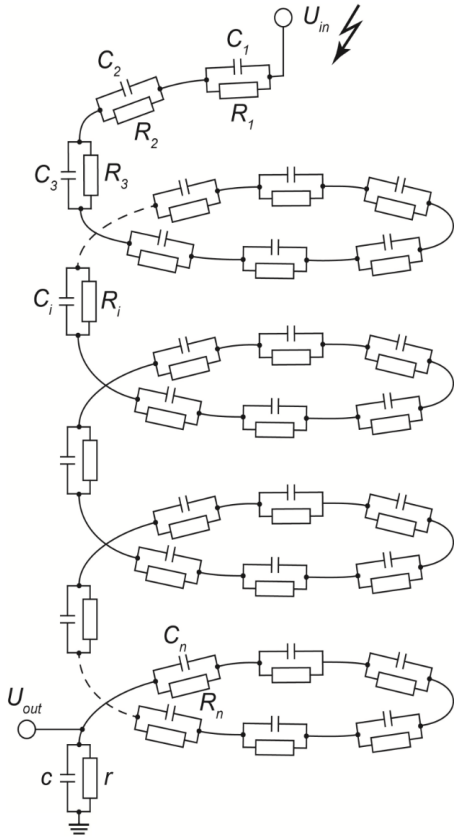

Fig. 1. Substitution circuit of the high-voltage divider voltages with parallel-series connection of *R*-, *C*- elements of the high-voltage arm

$$A = \frac{|U_{out}|}{|U_{in}|} = \frac{1}{K} A^*,$$

$$A^* = \sqrt{\frac{1+\gamma^2}{\left(1+\frac{K-1}{K} f\right)^2 + \gamma^2 \left(1+\frac{K-1}{K}\delta\right)^2}}, \quad (1)$$

$$\varphi = \operatorname{arctg}\left[\frac{(\delta - f)\gamma}{f + \frac{K}{K-1} + \gamma^2\left(\delta + \frac{K}{K-1}\right)}\right], \quad (2)$$

where K is the nominal value of the division factor of the voltage divider (in the general case $K>1$); A^* is the normalized frequency response value; $\gamma = \omega R C_0$ is the dimensionless angular frequency ω parameter; $C_0 = \frac{1}{n}\sum_{i=1}^{n} C_i$ is the average value of the C-elements of the high-voltage arm, which in the case under consideration corresponds to $C_0 \equiv C_N$; f, δ are the functions of non-identity of elements; $\alpha = \alpha' = -\Delta$, and $\alpha = \alpha'' = \Delta$, which are determined below:

$$f = \frac{1}{2} D(\alpha') + \frac{1}{2} D(\alpha''), \quad \delta = \frac{1}{2} G(\alpha') + \frac{1}{2} G(\alpha''), \quad (3)$$

where

$$D(\alpha) = \frac{\gamma^2 \alpha^2 (-1 + \gamma^2 (3 + 2\alpha))}{(1+\gamma^2)[1+\gamma^2(1+\alpha)^2]}, \quad (4)$$

$$G(\alpha) = \frac{\gamma^2 \alpha^2 (-3 - \alpha + \gamma^2 (1+\alpha))}{(1+\gamma^2)[1+\gamma^2(1+\alpha)^2]}. \quad (5)$$

Substituting in (3)-(5) values $\alpha' = -\Delta$, $\alpha'' = \Delta$ we obtain:

$$2f = \frac{\gamma^2 \Delta^2 (-1 + \gamma^2 (3 - 2\Delta))}{(1+\gamma^2)[1+\gamma^2(1-\Delta)^2]} + \frac{\gamma^2 \Delta^2 (-1 + \gamma^2 (3 + 2\Delta))}{(1+\gamma^2)[1+\gamma^2(1+\Delta)^2]}, \quad (6)$$

$$2\delta = \frac{\gamma^2 \Delta^2 (-3 + \Delta + \gamma^2 (1-\Delta))}{(1+\gamma^2)[1+\gamma^2(1-\Delta)^2]} + \frac{\gamma^2 \Delta^2 (-3 - \Delta + \gamma^2 (1+\Delta))}{(1+\gamma^2)[1+\gamma^2(1+\Delta)^2]}. \quad (7)$$

In [1], when deriving (1), (2), the well-known relations for the parameters of the low-voltage arm were taken:

$$r = \frac{nR}{K-1}, \quad c = \frac{C_0}{n}(K-1).$$

Even with the accepted simplifications (6), (7), the analytical study of the dependencies of A^*, φ on γ, Δ, K in the general case is impossible. Therefore, we will use the approach of limit values [13], as well as the concept of continuity of functions $A^*(\gamma, \Delta, K)$, $\varphi(\gamma, \Delta, K)$, which follows from their physical content.

Limit values of the function $A^*(\gamma, \Delta, K)$.

1.1. If $\Delta = 0$, then $A^* \equiv 1$ for any values γ, K, because the expressions f, δ (6), (7) in this case equal to zero.

1.2. If $\gamma = 0$, then also $A^* \equiv 1$ for any values of Δ, K, which physically corresponds to the generally accepted practice of calibration of broadband voltage dividers at high DC voltage.

1.3. Analyzing (1), (6), (7) we come to the conclusion that we can obtain the boundary expression for A^* in the approximation $\gamma^2 \to 0$. Indeed, holding in (1), (6), (7) members of the order of the unit, as well as members of the order $\gamma^2 << 1$, we find

$$\underset{\gamma \to 0}{A^*}(\gamma^2) = 1 + \frac{K-1}{K} \Delta^2 \gamma^2. \quad (8)$$

Analyzing (8), we conclude that A^* for the values of $\gamma << 1$ always increases in the region $A^* > 1$ in a parabolic dependence on γ, and in proportion to the square of the tolerance Δ^2 and the ratio $(K-1)/K$, i.e., the strongest this dependence is manifested for high-voltage dividers, for which $K >> 1$.

1.4. At another threshold $\gamma \to \infty$ we have:

$$f = \frac{\Delta^2 (3 - \Delta^2)}{(1-\Delta^2)^2}; \quad \delta = \frac{\Delta^2}{1-\Delta^2}, \quad (9)$$

and, accordingly:

$$\underset{\gamma \to \infty}{A^*} = \frac{1}{1 + \frac{K-1}{K} \frac{\Delta^2}{1-\Delta^2}}. \quad (10)$$

It follows from (10) that in this case always $A^* < 1$, and the deviation of A^* from 1 increases with increasing K and the value of the tolerance Δ (mainly proportional to Δ^2, because for the real tolerance range $0 < \Delta < 0.2$ contribution the denominator $1 - \Delta^2$ is $1 - 1.0417$).

1.5. It is of fundamental importance how A^* approaches its boundary expression (10): «above» or «below» under the condition $\gamma \to \infty$. To do this, judging by (1), it suffices to determine the behavior of δ in the region $\gamma \to \infty$. The transformation of expression (7) was performed by dividing the numerators and denominators

of its components by γ^4, and members of the order of units, $1/\gamma^2$ and $1/\gamma^4$, were obtained. Then, holding the members of the order of 1 and $1/\gamma^2$, the following expression was obtained:

$$\delta_{\gamma\to\infty}\left(\frac{1}{\gamma^2}\right)=\frac{\Delta^2}{1-\Delta^2}-\frac{\Delta^2}{2\gamma^2}\times$$
$$\times\left[\frac{3-\Delta}{(1-\Delta)^2}+\frac{1+(1-\Delta)^2}{(1-\Delta)^3}+\frac{3+\Delta}{(1+\Delta)^2}+\frac{1+(1+\Delta)^2}{(1+\Delta)^3}\right]. \quad (11)$$

The expression in square brackets for $0<\Delta<0.2$ is always greater than zero. Therefore, δ under the condition $\gamma\to\infty$ approaches its limit value $\Delta^2/(1-\Delta^2)$ from below. Accordingly, the function $A^*(\gamma)$ approaches its limit value (10) always from above.

1.6. Given that depending on γ there will be a transition from the values $A^*>1$ to the values $A^*<1$, it will be useful to find out the value A^* at $\gamma=1$. For this case, the substitution $\gamma=1$ in (1), (6), (7) after performing the reductions gives:

$$A^*(1)=\sqrt{\frac{1}{1-2\frac{\Delta^4}{4+\Delta^4}\frac{K-1}{K}(1-\frac{K-1}{2K})}}. \quad (12)$$

Analysis of (12), as well as of (8)-(11), under the condition $\Delta=0$ confirms the value $A^*\equiv1$. Since in the field of practical interest there is $0<\Delta<0.2$ and then $\Delta^4/(4+\Delta^4)<<1$, expression (12) can be represented as

$$A^*(1)\cong1+\frac{\Delta^4}{4+\Delta^4}\frac{K-1}{K}(1-\frac{K-1}{2K}). \quad (13)$$

For the values of $K>>1$ and $\Delta=0.2$, the addition to the unit in (13) is 0.0002. That is, all dependencies $A^*(\gamma)$ for $0<\Delta<0.2$ will practically pass through the point $A^*(1)=1$.

1.7. Investigation of A * in the range $0<\gamma<1$. From all previous features, in this range the maximum of the function should be. To find it, it is necessary to equate to zero the derivative $dA^*/d\gamma = 0$, and from this condition to determine the value γ_{max}, the substitution of which in (1), (6), (7) will allow to obtain the desired value A_{max}. Due to the complex dependence of A^* on the input values, which practically makes it impossible to perform these operations in analytical form, the computer code is used to find $A^*_{max}(\gamma_{max})$.

The SMath Studio computer code derived the functional dependence of A^* on γ, after which, using the mathematical modules of this code, we found the value γ_{max} for the extremum point and the extremum value A^*_{max} of this function for different Δ and K (by iterative calculation in the program cycle).

Table 1 shows the obtained results of calculations of A^*_{max}, γ_{max} for values $\Delta=0.01$; 0.02; … 0.19; 0.20 and values K = 10; 100; 1000; 10000.

Table 1

Results of calculations of values A^*_{max} (p.u.), γ_{max} (p.u.)

Value	K = 10		K = 100		K = 1000		K = 10000	
Δ, p.u.	γ_{max}	A^*_{max}	γ_{max}	A^*_{max}	γ_{max}	A^*_{max}	γ_{max}	A^*_{max}
0,01	0,577361	1,0000112502	0,577360	1,0000123752	0,577360	1,0000124877	0,577360	1,0000124990
0,02	0,577393	1,0000450035	0,577389	1,0000495037	0,577389	1,0000499537	0,577389	1,0000499988
0,03	0,577446	1,0001012677	0,577438	1,0001113939	0,577437	1,000112406	0,577437	1,0001125077
0,04	0,577520	1,0001800558	0,577506	1,0001980596	0,577504	1,0001998600	0,577504	1,0002000400
0,05	0,577615	1,0002813863	0,577593	1,0003095206	0,577591	1,0003123340	0,577591	1,0003126153
0,06	0,577732	1,0004052827	0,577700	1,0004458019	0,577697	1,0004498538	0,577697	1,0004502590
0,07	0,577870	1,0005517740	0,577827	1,0006069345	0,577823	1,0006124504	0,577822	1,0006130020
0,08	0,578029	1,0007208942	0,577973	1,0007929549	0,577968	1,0008001606	0,577967	1,0008008812
0,09	0,578210	1,0009126829	0,578139	1,0010039051	0,578132	1,0010130268	0,578131	1,0010139390
0,1	0,578412	1,0011271850	0,578325	1,001239833	0,578316	1,0012510971	0,578315	1,0012522235
0,11	0,578636	1,0013644507	0,578530	1,0015007923	0,578519	1,0015144254	0,578518	1,0015157887
0,12	0,578881	1,0016245356	0,578755	1,0017868422	0,578742	1,0018030714	0,578741	1,0018046943
0,13	0,579148	1,0019075010	0,579000	1,0020980480	0,578985	1,0021171007	0,578984	1,0021190059
0,14	0,579437	1,0022134135	0,579265	1,0024344807	0,579247	1,002456585	0,579246	1,0024587951
0,15	0,579748	1,0025423452	0,579550	1,0027962172	0,579530	1,0028216008	0,579528	1,0028241391
0,16	0,580081	1,0028943741	0,579855	1,00318334	0,579832	1,0032122322	0,579830	1,0032151214
0,17	0,580436	1,0032695835	0,580180	1,0035959389	0,580154	1,0036285684	0,580152	1,0036318313
0,18	0,580813	1,0036680628	0,580525	1,0040341078	0,580497	1,0040707048	0,580494	1,0040743644
0,19	0,581213	1,0040899069	0,580891	1,0044979482	0,580859	1,0045387429	0,580856	1,0045428223
0,2	0,581635	1,0045352169	0,581278	1,0049875672	0,581242	1,0050327906	0,581239	1,0050373128

Data processing from Table 1 allows to propose a simplified expression for $A^*_{\max}$ in the form:

$$A^*_{\max} = 1 + 0{,}1255\frac{K-1}{K}\Delta^2. \qquad (14)$$

The error is only the term of the right part (14) in relation to the corresponding data in Table 1 does not exceed ±0.4 % in absolute value, which can be considered quite acceptable.

Figure 2 shows graphs of dependencies $A^*(\gamma)$ calculated by (1), (6), (7) for values of parameters: Δ=0.05; 0.2; K=10; 10^4, which explain the results obtained. To track the complete change of the curves $A^*(\gamma)$, the range of change in γ (on the abscissa axis) is presented on a logarithmic scale (from γ = 0.001 to γ = 1000).

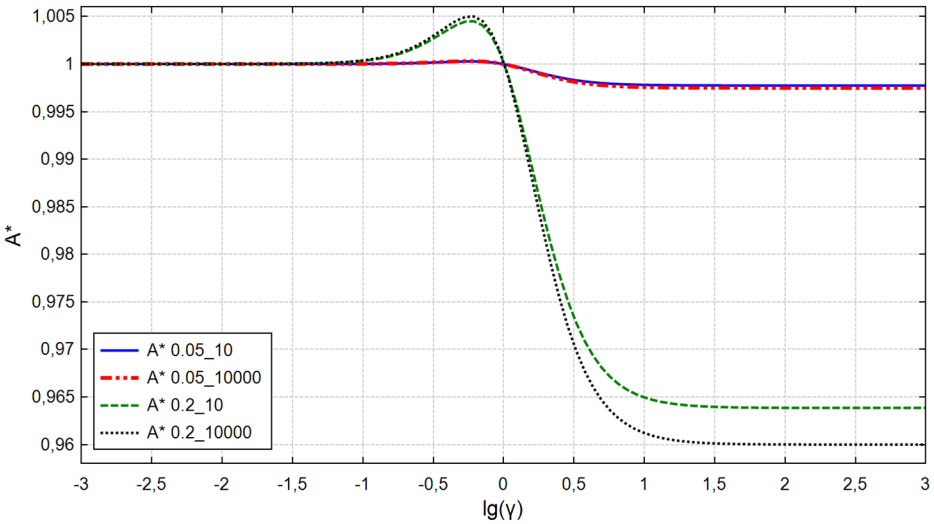

Fig. 2. Calculated dependencies $A^*(\gamma)$ by (1), (6), (7) for parameter values: Δ = 0.05; Δ = 0.2; K = 10; K = 10^4

Limit values of the function $\varphi(\gamma, \Delta, K)$. Both for the value $\gamma\to 0$ and for $\gamma\to\infty$, the function φ has a limit value $\varphi\to 0$, which physically corresponds to the idealized ohmic (in the first case) and idealized capacitive (in the second case) voltage divider.

The expansion of the function φ (2) by the powers of the small parameter γ under the condition $\gamma\to 0$ determines the expression

$$\underset{\gamma\to 0}{\varphi}(\gamma) = -2\frac{K-1}{K}\Delta^2\gamma^3, \qquad (15)$$

and the value φ in (15) is obtained in radians.

At another limit value $\gamma\to\infty$, the expansion of φ (2) by the powers of the small parameter $1/\gamma$ gives the expression

$$\underset{\gamma\to\infty}{\varphi}(\gamma) = -2\frac{K-1}{K}\cdot\frac{\Delta^2}{\gamma}\Psi(\Delta, K), \qquad (16)$$

where the correction function is of the order of unit

$$\Psi = \left(1 - 2\frac{\Delta^2}{K} - \frac{K-2}{K}\Delta^4\right)^{-1}.$$

Maximum value Ψ at Δ=0.2; K=10 is 1.009367, hence for the terms of consideration $1<\Psi<1.009367$.

Similarly to item 1.7, the values $\varphi'_{\min}$ (2), in angular minutes, and the corresponding values γ' (p.u.) were found using the SMath Studio computer code for the parameters Δ=0.01; 0.02; … 0.19; 0.2 and values K=10; 100; 1000; 10000, presented in Table 2.

Table 2

Results of calculations of values $\varphi'_{\min}$ (angular minutes), γ' (p.u.)

Value	K = 10		K = 100		K = 1000		K = 10000	
Δ, p.u.	γ'	$\varphi'_{\min}$	γ'	$\varphi'_{\min}$	γ'	$\varphi'_{\min}$	γ'	$\varphi'_{\min}$
0,01	1,73214	–0,200968	1,73213	–0,221064	1,73213	–0,223073	1,73213	–0,223274
0,02	1,73243	–0,80397	1,7324	–0,884355	1,73239	–0,892394	1,73239	–0,893197
0,03	1,7329	–1,80931	1,73283	–1,99018	1,73283	–2,00826	1,73283	–2,01007
0,04	1,73357	–3,21747	1,73345	–3,53903	1,73343	–3,57118	1,73343	–3,5744
0,05	1,73443	–5,02917	1,73424	–5,53162	1,73422	–5,58186	1,73422	–5,58689
0,06	1,73549	–7,2453	1,7352	–7,96886	1,73518	–8,04121	1,73517	–8,04844
0,07	1,73673	–9,86697	1,73635	–10,8519	1,73631	–10,9503	1,73631	–10,9602
0,08	1,73817	–12,8955	1,73767	–14,1819	1,73762	–14,3106	1,73762	–14,3234
0,09	1,73981	–16,3323	1,73918	–17,9606	1,73911	–18,1234	1,73911	–18,1397
0,1	1,74165	–20,1793	1,74086	–22,1897	1,74078	–22,3906	1,74077	–22,4107

Table 2 (continued)

Value	$K = 10$		$K = 100$		$K = 1000$		$K = 10000$	
Δ, p.u.	γ'	φ'_{min}	γ'	φ'_{min}	γ'	φ'_{min}	γ'	φ'_{min}
0,11	1,74368	–24,4383	1,74273	–26,871	1,74263	–27,1142	1,74262	–27,1385
0,12	1,74592	–29,1114	1,74478	–32,0069	1,74467	–32,2962	1,74466	–32,3252
0,13	1,74836	–34,2011	1,74702	–37,5995	1,74689	–37,9392	1,74687	–37,9731
0,14	1,751	–39,71	1,74945	–43,6517	1,74929	–44,0456	1,74928	–44,085
0,15	1,75386	–45,6408	1,75207	–50,1662	1,75189	–50,6183	1,75187	–50,6636
0,16	1,75692	–51,9966	1,75488	–57,1461	1,75468	–57,6605	1,75466	–57,712
0,17	1,7602	–58,7808	1,75789	–64,5947	1,75766	–65,1754	1,75764	–65,2335
0,18	1,76369	–65,9969	1,7611	–72,5155	1,76084	–73,1666	1,76081	–73,2317
0,19	1,76741	–73,6486	1,76451	–80,9124	1,76422	–81,6378	1,76419	–81,7103
0,2	1,77135	–81,74	1,76812	–89,7895	1,7678	–90,5932	1,76777	–90,6735

Data processing from Table 2 allows to propose a simplified expression for φ'_{min} in the form:

$$\varphi'_{min} = -2252\frac{K-1}{K}\Delta^2. \qquad (17)$$

The error (17) in relation to the corresponding data from Table 2 does not exceed ±0.85 % in absolute value, which can be considered acceptable.

Figure 3 shows the graphs of the dependencies $\varphi'(\gamma)$, calculated by (2), (6), (7) for the values of the parameters: Δ=0.05; 0.20; K=10; 10^4, explaining the results obtained. To track the complete change of the curves $\varphi'(\gamma)$ the range of change in γ (on the abscissa axis) is presented on a logarithmic scale (from γ=0.001 to γ=1000).

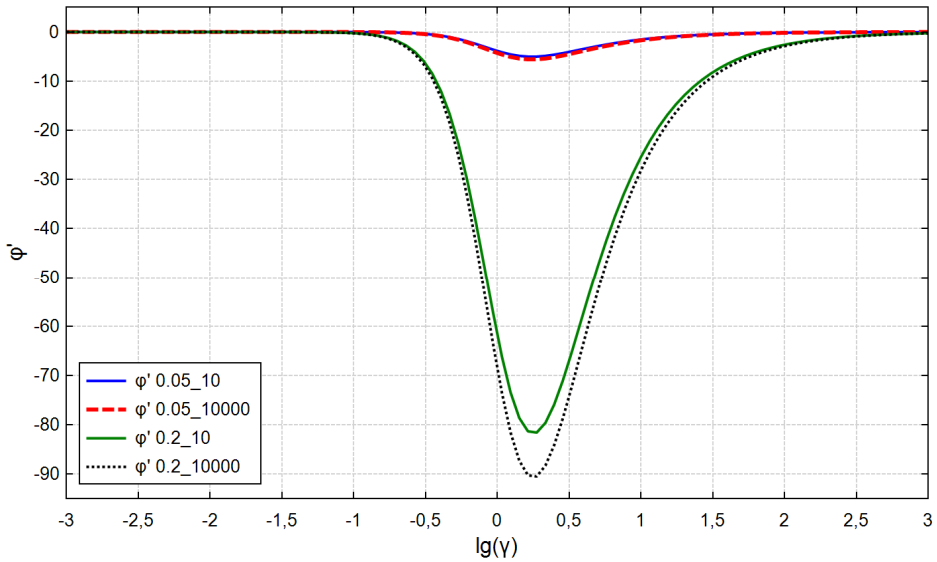

Fig. 3. Calculated dependencies φ' (angular minutes) on γ (p.u.) by (2), (6), (7) for parameter values: Δ = 0,05; Δ = 0,2; K = 10; K = 10^4

Discussion of the results obtained. For the first time in general form, the general features of the frequency characteristics of high-voltage broadband voltage dividers with parallel-series connection of *R*-, *C*- elements of the high-voltage arm, taking into account the non-identity of its capacitive components are discussed.

For the first time, the limiting influence of the non-identity of the capacitive elements of the high-voltage arm on the frequency response and PFC of the voltage divider was quantified and its essential importance was shown.

For the first time, simplified and, at the same time, sufficiently accurate expressions for the limit values of their frequency characteristics are proposed for the range of division factors of broadband voltage dividers $K \geq 10$. For the range of division factors of voltage dividers $1 < K < 10$ it is necessary to conduct additional research.

To reduce the deviations of the frequency response (from the normalized value) of the broadband voltage divider depending on the frequency, it may be recommended to use its adjusted value $A^*_{cor} = \frac{1}{2}\left(A^*_{max} + A^*_{\gamma\to\infty}\right)$ and the corresponding adjusted value of the division factor of the voltage divider $K_{cor} = K / A^*_{cor}$, which can be entered in its passport.

To reduce the deviations of the PFC (from the normalized value) of the voltage divider depending on the frequency, it is recommended to use its adjusted value $\varphi'_{cor} = 0.5 \cdot \varphi'_{min}$, which can be entered in the passport of the voltage divider for the range $\gamma > 0$.

Comparison of the obtained results with the data of publications [2-9] shows that the influence of non-identity

of capacitive elements of high-voltage arm of voltage dividers on their characteristics is significant along with other influencing factors and, therefore, should be taken into account in theory and practice of voltage dividers.

Conclusions.

For the first time in the analytical form the frequency characteristics of a broadband voltage divider are studied taking into account the ultimate influence of non-identity of capacitive elements of its high-voltage arm, which allows to clearly predict the limits of change of amplitude-frequency and phase-frequency characteristics of a voltage divider depending on the tolerance of its constituent elements.

To reduce deviations from the normalized values of the amplitude-frequency and phase-frequency characteristics of the broadband voltage divider depending on the frequency, it is recommended to use their adjusted values, which can be added in the passport and regulatory documentation of the voltage divider.

The obtained results allow to orient the predicted value of the tolerance of capacitive elements of the high-voltage arm when choosing broadband high-voltage voltage dividers, as well as during their development and manufacture.

Prospects for further development in this direction are associated with the use of different laws of distribution of actual values R_{RV}, C_{RV} within their tolerances, including asymmetric types of distributions.

Conflict of interest. The authors of the article declare no conflict of interest.

REFERENCES

1. Anokhin Y.L., Brzhezytskyi V.O., Haran Ya.O., Masliuchenko I.M., Protsenko O.P., Trotsenko Ye.O. Application of high voltage dividers for power quality indices measurement. *Electrical Engineering & Electromechanics*, 2017, no. 6, pp. 53-59. doi: https://doi.org/10.20998/2074-272x.2017.6.08.

2. Li D., Liu K., Lei M., Zhou F., Yue C., Yu J. Study on the ratio change measurement of 1000 kV HVDC divider based on improved DC voltage summation method. *High Voltage*, 2020, vol. 5, no. 2, pp. 202-208. doi: https://doi.org/10.1049/hve.2019.0127.

3. Fang Z., Luo Y., Zhai S., Qian B., Liao Y., Lan L., Wang D. Temperature rise characteristics and error analysis of a DC voltage divider. *Energies*, 2021, vol. 14, no. 7, p. 1914. doi: https://doi.org/10.3390/en14071914.

4. Alf-Peter E., Hällström J., Bergman A. Optimization of the design of a wideband 1000 kV resistive reference divider. *XVII International Symposium on High Voltage Engineering*, Hannover, Germany, August 22-26, 2011. Available at: http://vlabs.iitkgp.ac.in/vhvlab/html/pages/CD/topics_a-h/H-013-ELG-F.pdf (accessed 22 June 2020).

5. Khamlichi A., Rovira J. The Design and characterization of a prototype wideband voltage sensor based on a resistive divider. *Sensors*, 2017, vol. 17, no. 11, p. 2657. doi: https://doi.org/10.3390/s17112657.

6. Slomovitz D., Trigo L., Faverio C., Kyriazis G.A. Advance in the development of wideband resistive voltage dividers. *Journal of Physics: Conference Series*, 2021, vol. 1826, no. 1, p. 012083. doi: https://doi.org/10.1088/1742-6596/1826/1/012083.

7. Hrbac R., Kolar V., Bartlomiejczyk M., Mlcak T., Orsag P., Vanc J. A development of a capacitive voltage divider for high voltage measurement as part of a combined current and voltage sensor. *Elektronika ir Elektrotechnika*, 2020, vol. 26, no. 4, pp. 25-31. doi: https://doi.org/10.5755/j01.eie.26.4.25888.

8. Xu D., Zhang W., Wang N., Wang G., Xu G. The power frequency voltage divider calibration device and its uncertainty. *Energy Reports*, 2020, vol. 6, pp. 380-384. doi: https://doi.org/10.1016/j.egyr.2019.11.091.

9. Havunen J., Hällström J. Reference switching impulse voltage measuring system based on correcting the voltage divider response with software. *IEEE Transactions on Instrumentation and Measurement*, 2021, vol. 70, pp. 1-8. art. no. 1006008. doi: https://doi.org/10.1109/tim.2021.3063753.

10. Brzhezitsky V., Trotsenko Y., Haran Y. Optimization of amplitude-frequency characteristic of broadband voltage divider intended for measurement of power quality parameters. *Technology audit and production reserves*, 2020, vol. 3, no. 1 (53), pp. 35-39. doi: https://doi.org/10.15587/2706-5448.2020.205132.

11. Brzhezitsky V., Haran Y., Derzhuk A., Trotsenko Y., Protsenko O. Amplitude-frequency characteristic of broadband voltage divider with ultimate adjustment of its low-voltage arm. *2020 IEEE 7th International Conference on Energy Smart Systems (ESS)*, 2020, pp. 111-115, doi: https://doi.org/10.1109/ess50319.2020.9160094.

12. Brzhezytskyi V.O., Masliuchenko I.M., Laposha M.Y. Maximum influence of nonidentical R- and C-elements of a high-voltage divider on its frequency characteristics. *Power Engineering: economics, technique, ecology*, 2017, no. 1, pp. 70-76. (Ukr). doi: https://doi.org/10.20535/1813-5420.1.2017.102824.

13. Korn G.A., Korn T.M. *Mathematical handbook for Scientists and engineers*. Dover Publications, 2000. 1151 p.

Received 28.05.2021
Accepted 30.06.2021
Published 27.08.2021

V.O. Brzhezitsky[1], *Doctor of Technical Science, Professor,*
Y.O. Haran[1], *PhD,*
A.O. Derzhuk[1], *Postgraduate Student,*
O.R. Protsenko[1], *PhD, Associate Professor,*
Y.O. Trotsenko[1], *PhD, Associate Professor,*
M.M. Dixit[2],
[1] National Technical University of Ukraine «Igor Sikorsky Kyiv Polytechnic Institute»,
37, Prospect Peremohy, Kyiv-56, 03056, Ukraine,
e-mail: v.brzhezitskiy@ukr.net (Corresponding author)
[2] Vishwaniketan Institute of Management Entrepreneurship and Engineering Technology,
Survey No. 52, Kumbhivali, Tal, Khalapur, Maharashtra, 410202, India,
e-mail: mandardixit78@gmail.com

How to cite this article:
Brzhezitsky V.O., Haran Y.O., Derzhuk A.O., Protsenko O.R., Trotsenko Y.O., Dixit M.M. Ultimate effect of non-identity of capacitive elements of high-voltage arm on frequency characteristics of voltage divider (analytical research). *Electrical Engineering & Electromechanics*, 2021, no. 4, pp. 46-52. doi: https://doi.org/10.20998/2074-272X.2021.4.06.

UDC 621.3 https://doi.org/10.20998/2074-272X.2021.4.07

A. Boussaid, S.E.I. Chelli, A.L. Nemmour, A. Khezzar

AN EFFECTIVE CONTROL ALGORITHM FOR DYNAMIC VOLTAGE RESTORER UNDER SYMMETRICAL AND ASYMMETRICAL GRID VOLTAGE CONDITIONS

Introduction. *Voltage sag, which is associated to a transitory drop in the root mean square voltage characterizing an electrical source network. During these perturbations, the corresponding electronic customers and devices will suffer from serious operating troubles causing dangerous damages.* ***Purpose.*** *In order to attenuate this disturbance effects, the Controlled Dynamic Voltage Restorer constitutes a very interesting solution among many others that have been proposed.* ***The novelty*** *of the proposed work consists in presenting an enhanced algorithm to control efficiently the dynamic voltage restorer when voltage sag is suddenly occurred.* ***Methods.*** *The proposed algorithm is based on an instantaneous phase locked loop using a multi variable filter to synthesize unitary signals involved in compensation voltages computation relative to the sag apparition.* ***Practical value.*** *A detailed study concerning typical voltage sag, which is consolidated by simulation and experimental results, is conducted to show the used algorithm's effectiveness to cancel the corresponding voltage sag.* References 44, table 1, figures 16.

Key words: **dynamic voltage restorer, power quality, voltage sag, phase locked loop, synchronous reference frame.**

Вступ. *Провал напруги, який пов'язаний із тимчасовим падінням середньоквадратичної напруги, характеризує мережу джерел електричної енергії. Під час цих збурень відповідні споживачі (електронні прилади та інші пристрої) будуть страждати від серйозних проблем у їхній експлуатації, що спричиняють небезпечні пошкодження.* ***Призначення***. *Для того, щоб послабити вплив цих збурень, контрольований динамічний відновник напруги видається дуже цікавим рішенням серед багатьох інших, які були запропоновані.* ***Новизна*** *запропонованої роботи полягає у представленні вдосконаленого алгоритму ефективного управління динамічним відновником напруги, коли раптово відбувається провал напруги.* ***Методи***. *Запропонований алгоритм базується на миттєвому фазовому замкненому контурі з використанням багатоваріантного фільтра для синтезу унітарних сигналів, що беруть участь у обчисленні напруги компенсації стосовно прояву провалу.* ***Практичне значення***. *Детальне дослідження стосовно типового провалу напруги, яке узагальнено за допомогою моделювання та експериментальних результатів, проведено, щоб показати ефективність використовуваного алгоритму для ліквідації відповідного провалу напруги.* Бібл. 44, табл. 1, рис. 16.

Ключові слова: **динамічний відновник напруги, якість електроенергії, провал напруги, фазовий замкнений контур, синхронна система відліку.**

1. Introduction. Power distribution system is an irreplaceable thing. Indeed, it should provide energy for costumers in an ideal sinusoidal form. For that, the number of connected equipments to the power network still increasing but that fact imposes critical problems to the network [1–3]. Poor power quality outcomes in financial losses which has a major harmful impact on the economical industry sector.

The voltage quality issues is more important in comparison to sensitive loads which requires to be supplied cautiously, regarding to the previous mentioned problem, it consist mainly in voltage sags and swells, voltage harmonics, current harmonics, fluctuations (flickers), frequency variation and unbalance [4–7].

Voltage sag has been widely studied in a considerable research papers, which is defined as temporary decrease in the root mean square voltage between 10 to 90 % of nominal voltage, for a duration interval of 0.5 cycles to one minute as it's presented in IEEE 1346, IEEE 1159 and IEC 61000-2-1 standers [8, 9]. By way of explanation it is characterized by a sudden reduction of nominal voltage from 0.1 to 0.9 per unit followed after a short period of time by a voltage recovery. According to the mentioned standards, normal voltage sag takes from 10 ms to 1 minute.

Voltage sags caused mainly by large induction motors starting or by different faults related to power system. Consequentially, sensitive loads and a significant number of electronic devices could be malfunctioned or completely deteriorated as a result for voltage sag occurrence. Hence, huge losses at costumer loads are take place.

Voltage swell is defined in the previous mentioned IEEE standard as an increase in the root mean square (RMS) supply voltage from 1.1 to 1.8 per unit for duration from 0.5 cycles to 1 min. Voltage swell are mainly due to large capacitors switching or connecting / disconnecting of heavy loads. Voltage swells are less widespread in distribution network, for that reason, they are not as important as voltage sags [10–14].

The above mentioned issues related to power quality has opened up a discussion on possible solutions to overcome these problems. Researchers have proposed a large number of custom power devices (CPDs). The most effective one is to use compensators based on power electronic devices.

These compensators could be in series, shunt or hybrid form. Literature is rich by numerous classifications of CPD [15], Based upon its structure, various custom power devices are usually classified into three categories: unified power quality conditioners (UPQC), distribution static compensator (D-STATCOM) and dynamic voltage restorer (DVR).

Using series or shunt power filters in separate may not be the wanted preferred solution. For this reason, the device named UPQC [16, 17] performing both functionalities of series and shunt active filter is introduced and its concept is developed [18, 19].

The D-STATCOM is another choice for solving voltage unbalance, and power quality enhancement. It maintains the voltage sag at the desired reference by supplying or receiving the reactive power in the distribution

network. This compensator has been deployed in a three-phase four-wire distribution system [20].

Another alternative based on series custom power compensation could ensure a high quality voltage purpose [12, 13]. DVR is composed of a dc-energy storage system, a voltage source converter, an output filter and a coupling transformer.

The performance of the abovementioned CPDs is related mainly to the control algorithm of each device. Indeed, researchers pay a great attention to the algorithm strategies. Instantaneous Symmetrical Components Theory (ISCT) generates reference waveforms to balance a given load [21, 22]. Instantaneous Power Theory is introduced to compensate voltage faults in a dynamic way in the time domain based on PQR transformation [23]. Adaline (Adaptive linear element) control strategy is an Artificial Neural Network (ANN) that is used to control a capacitor supported DVR for power quality enhancement [24]. Space Vector PWM Strategy is presented in [25] to control a modified DVR composed of a conventional three phase voltage source inverter and an emitter follower. Synchronous Reference Frame Theory [26] is one of the most used algorithms to generate reference signals; its operating principle is based mainly on converting the load voltages to the rotating reference frame using the Park's transformation with unit vectors derived by a phase locked loop (PLL).

Detecting the grid phase angle and frequency in a fast and accurate way is the key of a good synchronization process. Several synchronization methods have been proposed in literature; the method based on detecting the zero crossing point of the grid voltages is characterized by a large synchronization time. In addition, it fails in detecting that point in case of grid frequency variation and unbalanced voltages.

The algorithm based on $\alpha\beta$ stationary reference frame conversion [27] is another alternative to detect the grid phase angle and frequency. The algorithm performances are related mainly to the intrinsic filter parameters that affect the algorithm dynamic response under asymmetrical grid faults conditions.

In three phase application, the phase locked loop (PLL) is the most used strategy where the synchronous reference frame (SRF) based PLL constitutes the common configuration [28–30]. It based on transforming the three phase voltages from *abc* frame to synchronous rotating reference frame using Park's transformation in order to identify the grid angle and frequency quantities.

Synchronous Reference Frame is known as a feed forward open loop control strategy. It is characterized by its simplicity and stability. Their main inconvenient is expressed in poor transient response and possibility offset error at the steady state because of voltage drop on the injection transformer and the series branch of the filter. To overcome these problems, feedback controllers are used. Feedback control process consists of measuring the DVR output voltages and fed back to the controller voltages. A variety of controllers have been presented in literature such as proportional, Proportional-Integral (PI), Proportional-resonant (PR) [31, 32], fuzzy controller [33, 34], H_∞ controller [35], sliding mode controller [36–38], state variable controller [39], predictive and repetitive controllers [40–42], feedback linearization [43].

The goal of the paper is the investigation of an effective phase locked loop to generate unitary signals that contain the fundamental voltage phase angle information used in calculating compensating voltage in case of a voltage sag occurrence.

Subject of investigations. The introduced PLL is compared to the conventional one in simulation and experiment. After that, controlling the DVR by the proposed algorithm is accomplished to show the effectiveness of the algorithm.

This paper is structured as follows: Section 2 describes the Dynamic Voltage Restorer Configuration topology with its operating principle with respect to sudden voltage sags occurring. Section 3 presents the control algorithm explaining both conventional phase locked loop topology and the proposed one. Section 4 discusses the obtained results through simulation and experimentation studies. Finally, a conclusion relative to the obtainable work is presented.

2. DVR Configuration Topology. A dynamic voltage restorer is generally connected in series with the protected load through a transformer. A DVR generates voltage references to be added to those of the grid in order to compensate the voltage disturbance at the load side. The schematic configuration of a typical DVR is presented in Fig. 1, which contains the following elements:

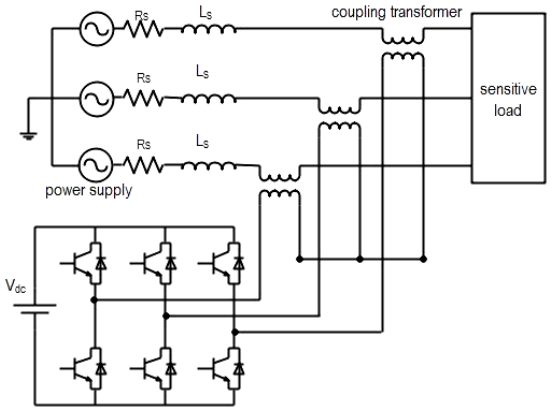

Fig. 1. DVR Schematic Topology

1) *Energy storage device*: commonly called DC bus side, it allows the voltage source inverter to provide the power grid by the reference generated voltages via the transformer. It could be batteries, capacities or even photovoltaic panels.

2) *Voltage Source Inverter* (*VSI*): a voltage source inverter is a power electronic configuration fed by the previously mentioned energy storage device to regenerate the desired sinusoidal voltage references. Recently, the switching configuration of the Voltage Source Inverter is based on IGBT. Nevertheless, peaks due to the switching process are eliminated by passive elements such as resistance R, inductance L, and a capacitance C at the VSI output.

3) *Injection transformer*: the main purpose of this transformer is to inject the generated voltage references to

the power grid which is connected by its high voltage side, whereas, the low voltage side is connected to the DVR power circuit.

4) *Control strategy*: control algorithm is considered as DVR heart. definitely, it detect the voltage disturbance and generate a voltage reference in phase to those of the grid and control the Voltage Source Inverter by generated voltage in feedback control in order to compensate the occurred voltage disturbance.

DVR could be expressed in an equivalent circuit (Fig. 2). It consists of a source voltage V_s delivering a current I_s, the source reactance is defined by X_s. The considered source is feeding two identical loads Z_A and Z_B passing through a feeder for each load F_A and F_B, each feeder has a reactance x_A and x_B respectively.

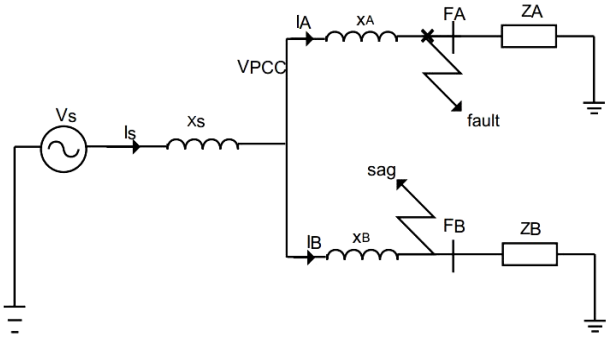

Fig. 2. Equivalent circuit for voltage sag calculation

From the equivalent circuit and basing on Kirchhoff's Law, voltage $V_{pre\text{-}sag}$ and current I_s in case of healthy power grid at the point of common coupling are given by:

$$V_{pre-sag} = V_s - I_s X_s; \quad (1)$$

$$I_s = I_A + I_B = \frac{V_{pre-sag}}{Z_A + x_A} + \frac{V_{pre-sag}}{Z_B + x_B} \quad (2)$$

The current through Z_A and Z_B is the same because of the identical impedances in healthy conditions. At the occurrence fault time on the first feeder, a high circuit current will flow to the broken feeder, on the other side, the current of the second feeder will be reduced. Therefore, the voltage of the second feeder will be decreased as well. This voltage drops is defined as voltage sag. At that point, the source current I_{sfault} and voltage sag V_{sag} are defined as:

$$V_{sag} = V_s - I_{sfault} X_s; \quad (3)$$

$$I_{sfault} = \frac{V_{sag}}{x_A} + \frac{V_{sag}}{Z_B + x_B}. \quad (4)$$

Thus, DVR must be inserted between the point of common coupling and the sensitive load where the voltage sag takes place. Figure 3 illustrates the DVR placement process.

Most of disturbances in power grid are related to voltage sag and swell. Decreasing and increasing of voltage amplitude at the load side are accompanied by a phase angle jump, for that, control strategies must be adopted to compensate this issue in a very fast way in order to avoid losses of power supply. Figure 4 shows the phasor diagram for a DVR compensation in both voltage sag and voltage swell.

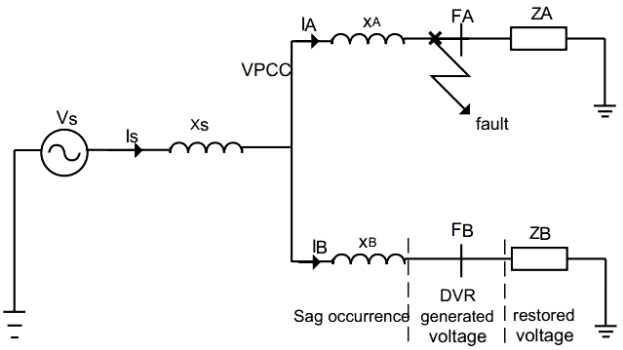

Fig. 3. Equivalent circuit for DVR voltage injection calculation

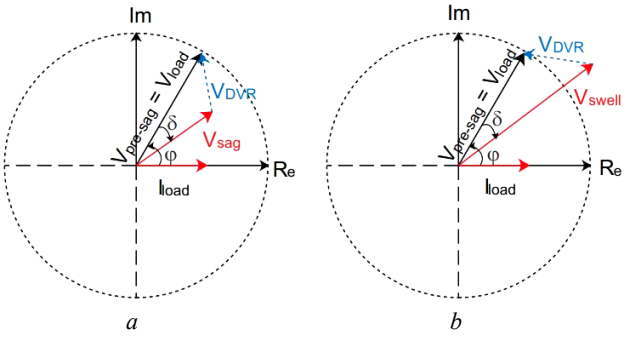

Fig. 4. Phasor diagram for:
(*a*) voltage sag compensation; (*b*) voltage swell compensation

3. DVR Control Strategy. The DVR compensates voltage sags by injecting or absorbing reactive power or real power [44]. Reactive power is injected when the DVR voltages are in quadrature with the currents with respect to fundamental frequency, at that point, DVR relay on a self supported dc bus. Nevertheless, active power is injected when the DVR voltages are in phase with the current, thereupon, the need of a battery at the DC bus is necessary.

The voltages references are used to generate the IGBTs gate pulses for the voltage source inverter in a synchronous reference frame. The schematic corresponding to the SRF theory is shown in Fig. 5.

Firstly, source and load voltages are sensed and transformed to a stationary references frame using Concordia transformation as follow:

$$\begin{cases} v_{sa} = \sum_{h=-1}^{+1} V_{sah} \sin(\omega t + \phi_{sah}); \\ v_{sb} = \sum_{h=-1}^{+1} V_{sbh} \sin(\omega t + \phi_{sbh} - \frac{2\pi}{3}); \\ v_{sc} = \sum_{h=-1}^{+1} V_{sch} \sin(\omega t + \phi_{sch} + \frac{2\pi}{3}); \end{cases} \quad (5)$$

$$\begin{cases} v_{La} = \sum_{h=-1}^{+1} V_{Lah} \sin(\omega t + \phi_{Lah}); \\ v_{Lb} = \sum_{h=-1}^{+1} V_{Lbh} \sin(\omega t + \phi_{Lbh} - \frac{2\pi}{3}); \\ v_{Lc} = \sum_{h=-1}^{+1} V_{Lch} \sin(\omega t + \phi_{Lch} + \frac{2\pi}{3}), \end{cases} \quad (6)$$

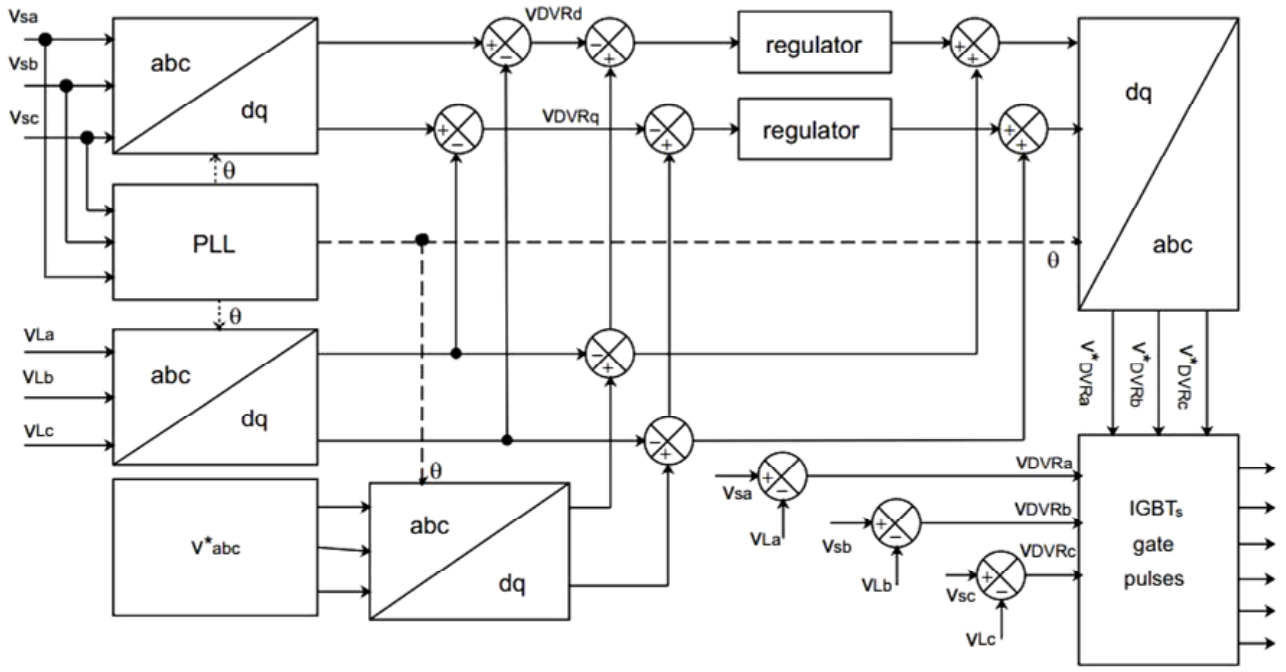

Fig. 5. Block diagram of the SRF control method

where: V_{sah}, V_{sbh} and V_{sch} are the voltages source amplitudes; V_{Lah}, V_{Lbh} and V_{Lch} are the voltages load amplitudes; ϕ_{sah}, ϕ_{sbh} and ϕ_{sch} are the voltages source phase angles; ϕ_{Lah}, ϕ_{Lbh} and ϕ_{Lch} are the voltages load phase angles; ω is the voltage fundamental pulsation.

$$\begin{bmatrix} v_{s\alpha} \\ v_{s\beta} \end{bmatrix} = \sqrt{\frac{2}{3}} \begin{bmatrix} 1 & -\frac{1}{2} & -\frac{1}{2} \\ 0 & \frac{\sqrt{3}}{2} & -\frac{\sqrt{3}}{2} \end{bmatrix} \begin{bmatrix} v_{sa} \\ v_{sb} \\ v_{sc} \end{bmatrix}; \quad (7)$$

$$\begin{bmatrix} v_{L\alpha} \\ v_{L\beta} \end{bmatrix} = \sqrt{\frac{2}{3}} \begin{bmatrix} 1 & -\frac{1}{2} & -\frac{1}{2} \\ 0 & \frac{\sqrt{3}}{2} & -\frac{\sqrt{3}}{2} \end{bmatrix} \begin{bmatrix} v_{La} \\ v_{Lb} \\ v_{Lc} \end{bmatrix}. \quad (8)$$

Since the voltages are converted to a stationary reference frame, the unit vector derived through a phase locked loop is taking in account to transform these voltages to a synchronous reference frame using Park transformation:

$$\begin{bmatrix} v_{sd} \\ v_{sq} \end{bmatrix} = \sqrt{\frac{2}{3}} \begin{bmatrix} \cos\theta & \sin\theta \\ -\sin\theta & \cos\theta \end{bmatrix} \begin{bmatrix} v_{s\alpha} \\ v_{s\beta} \end{bmatrix}; \quad (9)$$

$$\begin{bmatrix} v_{Ld} \\ v_{Lq} \end{bmatrix} = \sqrt{\frac{2}{3}} \begin{bmatrix} \cos\theta & \sin\theta \\ -\sin\theta & \cos\theta \end{bmatrix} \begin{bmatrix} v_{L\alpha} \\ v_{L\beta} \end{bmatrix}. \quad (10)$$

Figure 6 shows the phasor diagram of synchronous transformation. The $\alpha\beta$ coordinates are orthogonal axes obtained from the *abc* frame. The *dq* synchronous frame is obtained by rotating the the $\alpha\beta$ coordinates.

The reference load voltages (v^*_{La}, v^*_{Lb}, v^*_{Lc}) are transformed to a synchronous reference frame as well in the same way. In the meantime, the DVR voltage along *dq* frame could be expressed by:

$$\begin{cases} v_{DVR_d} = v_{sd} - v_{Ld}; \\ v_{DVR_q} = v_{sq} - v_{Lq}. \end{cases} \quad (11)$$

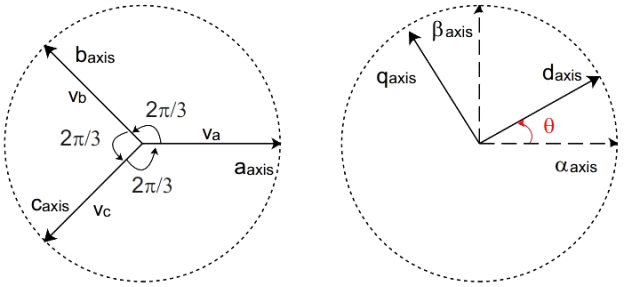

a *b*

Fig. 6. Phasor diagram exhibits the relation between *abc* frame (*a*) and *dq* frame (*b*)

Consequently, the DVR reference voltages are obtained by:

$$\begin{cases} v^*_{DVR_d} = v^*_{sd} - v_{Ld}; \\ v^*_{DVR_q} = v^*_{sq} - v_{Lq}. \end{cases} \quad (12)$$

A controller is used to minimize the error between actual DVR voltages and the generated reference voltage. Lastly, DVR reference voltages are obtained in *abc* reference frame by applying the Concordia inverse transformation and Park inverse transformation as follow:

$$\begin{bmatrix} v^*_{DVR_\alpha} \\ v^*_{DVR_\beta} \end{bmatrix} = \sqrt{\frac{2}{3}} \begin{bmatrix} \cos\theta & -\sin\theta \\ \sin\theta & \cos\theta \end{bmatrix} \begin{bmatrix} v^*_{DVRd} \\ v^*_{DVRq} \end{bmatrix}; \quad (13)$$

$$\begin{bmatrix} v^*_{DVR_a} \\ v^*_{DVR_b} \\ v^*_{DVR_c} \end{bmatrix} = \sqrt{\frac{2}{3}} \begin{bmatrix} 1 & 0 \\ -\frac{1}{2} & \frac{\sqrt{3}}{2} \\ -\frac{1}{2} & -\frac{\sqrt{3}}{2} \end{bmatrix} \begin{bmatrix} v^*_{DVR\alpha} \\ v^*_{DVR\beta} \end{bmatrix}. \quad (14)$$

The three phase voltages system. The balanced three phase voltages system which takes into account any type of distortion can expressed by:

$$\begin{cases} v_{sa} = \sum_{h=-\infty}^{+\infty} V_h \sin(h\omega t + \phi_h); \\ v_{sb} = \sum_{h=-\infty}^{+\infty} V_h \sin(h\omega t + \phi_h - \frac{2\pi}{3}); \\ v_{sc} = \sum_{h=-\infty}^{+\infty} V_h \sin(h\omega t + \phi_h + \frac{2\pi}{3}). \end{cases} \quad (15)$$

The three phase distorted currents form could be represented as follow:

$$\begin{cases} i_{sa} = \sum_{h=-\infty}^{+\infty} I_h \sin(h\omega t + \varphi_h); \\ i_{sb} = \sum_{h=-\infty}^{+\infty} I_h \sin(h\omega t + \varphi_h - \frac{2\pi}{3}); \\ i_{sc} = \sum_{h=-\infty}^{+\infty} I_h \sin(h\omega t + \varphi_h + \frac{2\pi}{3}), \end{cases} \quad (16)$$

where: h denotes the order of the inverse, homopolar and direct harmonic components in the voltage or current systems; V_h, I_h, ϕ_h and φ_h are the amplitudes and phase angles of the harmonic components of the voltage and current systems respectively; $\omega = 2\pi f_s$ is the fundamental pulsation of the voltage or current systems.

Phase Locked Loop. Conventional Phase Locked Loop. A PLL principal is based mainly on Park transformation, beyond that, if the instantaneous derivative angle involved in Park transformation is equal to the three phase voltage pulsation system, the components along *dq* axes will be constant.

The block diagram of a typical PLL is shown in Fig. 7, it contain a phase detector (PD) in order to perform a comparison between the input signal and the arrived one from the Voltage Controlled Oscillator (VCO). Low-pass filter (LPF) is used to correct the error at the PD-output.

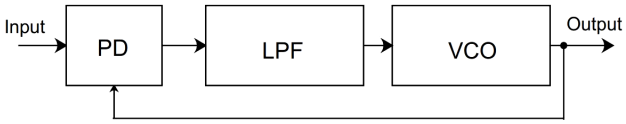

Fig. 7. Typical phase locked loop block diagram

The PLL consider the utility voltages expressed by Eq. (5), then, it goes to a synchronous frame passing by stationary frame using Eq. (7) and Eq. (9). After all calculation, the obtained equation is given by:

$$\begin{cases} v_d = V_s \sin(\theta - \theta_{mes}); \\ v_q = V_s \cos(\theta - \theta_{mes}). \end{cases} \quad (17)$$

From Eq. (17) one can notice that, if the phase angle error $\theta_\xi = \theta - \theta_{mes}$ is small, than this equation becomes:

$$v_d = V_s(\theta - \theta_{mes}). \quad (18)$$

At the moment $\theta = \theta_{mes}$, the PLL is locked, on the other hand, if $\theta \neq \theta_{mes}$, the phase error is governed by a controller adjusting ω until $\theta = \theta_{mes}$.

To accomplish the above explained phase lock, we consider the following block diagram of the locked loop as shown in Fig. 8.

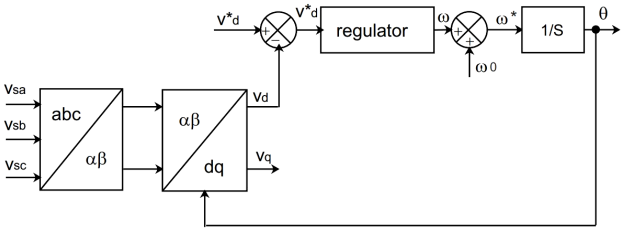

Fig. 8. Three phase PLL structure diagram

Proposed-Phase Locked Loop. The main purpose of any PLL configuration is to generate a unite vector containing the utility phase angle in order to pass to a synchronous reference frame. The proposed configuration is based on a Multi Variable Filter (MVF) to generate a *sin* and *cos* unite vectors directly that contain the utility phase angle information.

The transfer function of the MVF is based on 'Hong-Seok-Song' work. Its formulation is expressed by the following equation

$$\begin{cases} \tilde{x}_\alpha(s) = \frac{k(s+k)}{(s+k)^2 + \omega_c^2} x_\alpha(s) - \frac{k\omega_c}{(s+k)^2 + \omega_c^2} x_\beta(s); \\ \tilde{x}_\beta(s) = \frac{k(s+k)}{(s+k)^2 + \omega_c^2} x_\beta(s) + \frac{k\omega_c}{(s+k)^2 + \omega_c^2} x_\alpha(s), \end{cases} \quad (19)$$

where x_α, x_β are the input signals and $\tilde{x}_\alpha$, $\tilde{x}_\beta$ are the fundamental output signals.

From its formulation, the MVF filter is similar to a band-pass filter in the output response. Conversely, the integral effect of the MVF is neglected because it does not introduce a phase shift to the output signal regarding to its input. By way of explanation, both input and outputs MVF's signals have the same phase angle.

The developed analytical formulation of Eq. (19), could be given by:

$$\tilde{x}_\alpha = \sqrt{\frac{3}{2}} \sum_{h=-\infty}^{+\infty} \frac{I_h}{\sqrt{1 + \left(\frac{(1-h)\omega}{k}\right)^2}} \begin{pmatrix} \sin\left(h\omega t + \varphi_h + a\tan\left(\frac{(1-h)\omega}{k}\right)\right) \\ -e^{-kt} \sin\left(h\omega t + \varphi_h + a\tan\left(\frac{(1-h)\omega}{k}\right)\right) \end{pmatrix} \quad (20)$$

$$\tilde{x}_\beta = -\sqrt{\frac{3}{2}} \sum_{h=-\infty}^{+\infty} \frac{I_h}{\sqrt{1 + \left(\frac{(1-h)\omega}{k}\right)^2}} \begin{pmatrix} \cos\left(h\omega t + \varphi_h + a\tan\left(\frac{(1-h)\omega}{k}\right)\right) \\ -e^{-kt} \cos\left(h\omega t + \varphi_h + a\tan\left(\frac{(1-h)\omega}{k}\right)\right) \end{pmatrix}$$

Eq. (20) shows that the MVF effectiveness in cancelation any kind of disturbance is related principally to the constant k. Indeed, it is obvious if k is taken small, the disturbances will be attenuated perfectly. Otherwise, the transient time response will increase in parallel which is explained by the exponential part. In this case, taking k so small, Eq. (20) takes the following form:

$$\begin{cases} \tilde{x}_\alpha = \sqrt{\frac{3}{2}}\left(1 - e^{-kt}\right)\sin(\omega t + \varphi_1); \\ \tilde{x}_\beta = -\sqrt{\frac{3}{2}}\left(1 - e^{-kt}\right)\cos(\omega t + \varphi_1). \end{cases} \quad (21)$$

The concept is to hold back the voltage disturbance as possible in order to get a correct phase angle information which lead to a correct DVR control. A unit vector is obtained instantaneously without any phase

shift by taking k so small, the negative aspect of large time response is defeated. The unit vector is defined by Eq. (22):

$$\begin{cases} \dfrac{\tilde{x}_\alpha(t)}{\sqrt{\tilde{x}_\alpha^2+\tilde{x}_\beta^2}} = \sin(\omega t+\varphi_1); \\ \dfrac{\tilde{x}_\beta(t)}{\sqrt{\tilde{x}_\alpha^2+\tilde{x}_\beta^2}} = \cos(\omega t+\varphi_1). \end{cases} \quad (22)$$

4. Performances of the proposed PLL. To examine the proposed PLL performances, several tests have been accomplished. In the first case, a balanced three phase source voltages are considered as presented in Fig. 9.

From Fig. 9,a.1 and Fig. 9,b.1 one can notice that, the classical and proposed PLL have similar behavior where they produce suitable unit vectors, it is obvious from the presented phase angles as shown in Fig. 9,a.2 and Fig. 9,b.2.

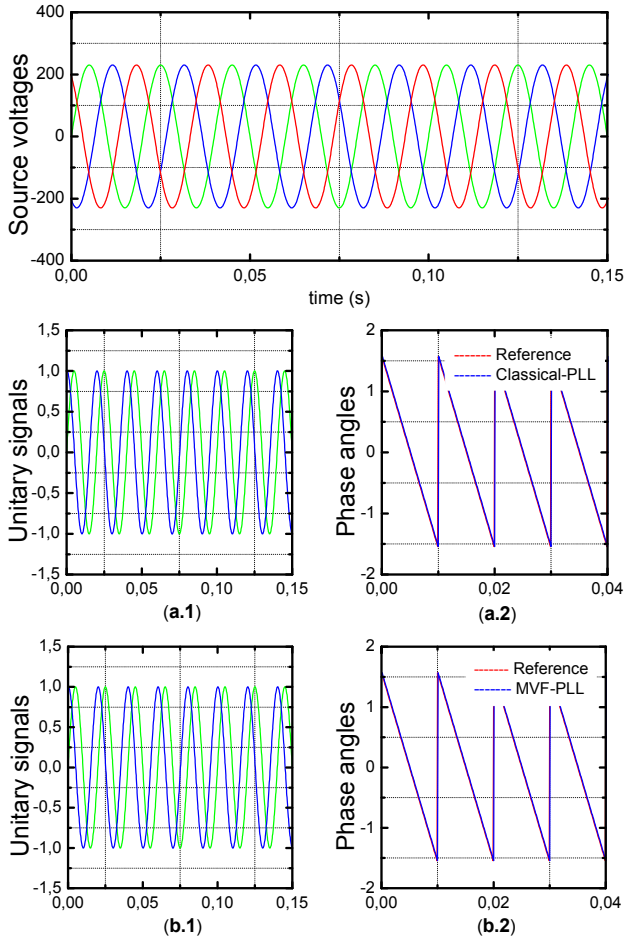

Fig. 9. Simulation results, Case 1: Balanced source voltages

The second case of study takes unbalanced three phase voltages without harmonics expressed in a total mitigation of voltage phase as shown in Fig. 10.

In this case, the classical PLL fails in extracting the sin and cosine signals from the unbalanced source voltages as presented in Fig. 10,a.1, this fact leads to a phase angle shifting from its reference as illustrated in Fig. 10,a.2.

On the other hand, the proposed PLL still give pure unit vectors in Fig. 10,b.1, with a soft phase angle shifting from $t = 0$ s to $t = 0.01$ s, which is totally acceptable under these sever unbalance conditions as shown in Fig. 10,b.2.

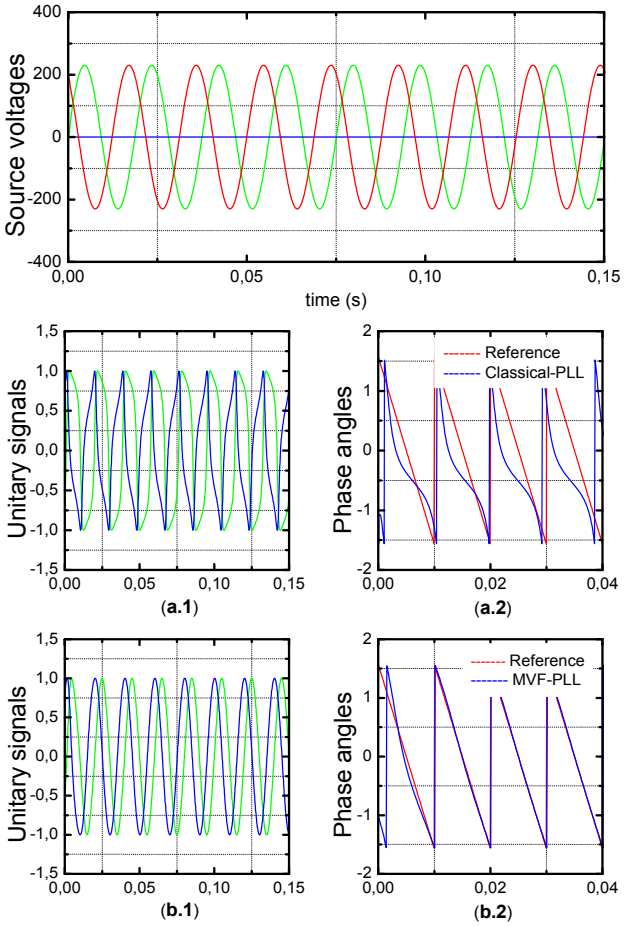

Fig. 10. Simulation results, Case 2: Unbalanced source voltages

The three phase source voltages are considered balanced and distorted by injecting the third and the fifth harmonics in the main voltages defined by the following equations:

$$\begin{cases} v_a = V_{a1}\sin(\omega t+\varphi_{a1})+V_{a3}\sin(3\omega t+\varphi_{a3})+ \\ +V_{a5}\sin(5\omega t+\varphi_{a5}); \\ v_b = V_{b1}\sin\left(\omega t+\varphi_{b1}-\dfrac{2\pi}{3}\right)+V_{b3}\sin\left(3\omega t+\varphi_{b3}-\dfrac{2\pi}{3}\right)+ \\ +V_{b5}\sin\left(5\omega t+\varphi_{b5}-\dfrac{2\pi}{3}\right); \\ v_c = V_{c1}\sin\left(\omega t+\varphi_{c1}+\dfrac{2\pi}{3}\right)+V_{c3}\sin\left(3\omega t+\varphi_{c3}+\dfrac{2\pi}{3}\right)+ \\ +V_{c5}\sin\left(5\omega t+\varphi_{c5}+\dfrac{2\pi}{3}\right). \end{cases} \quad (23)$$

Figure 11 describes the three phase distorted voltages. From Fig. 11,a.1 and Fig. 11,a.2 it is clear that the classical PLL exhibits poor capacities in extracting the unit vectors containing the phase angle information. Otherwise, the proposed PLL still present high capability in giving an instantaneous unit vector even the presence of harmonics in the three phase source voltages as illustrated in Fig. 11,b.1 and Fig. 11,b.2.

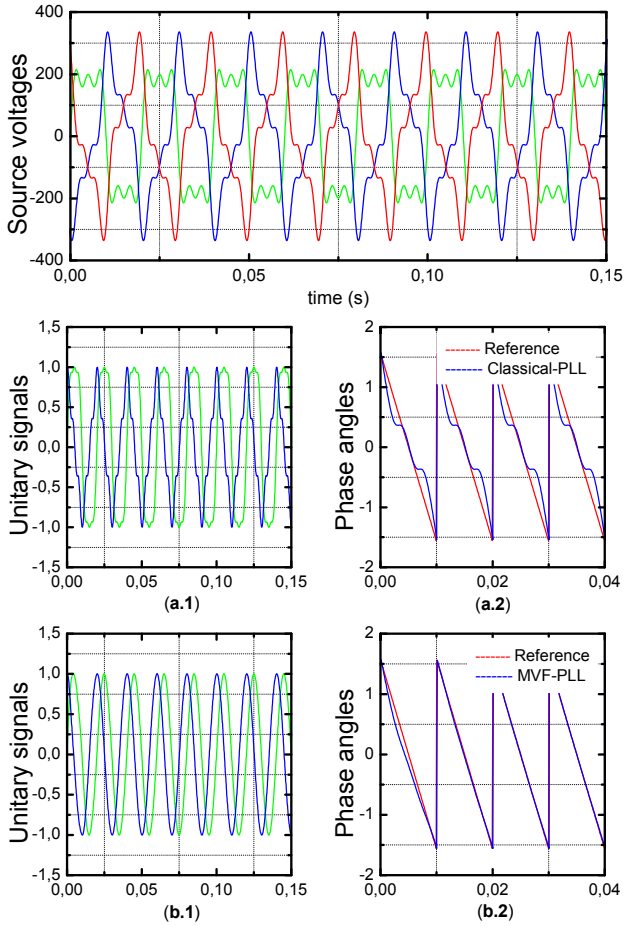

Fig. 11. Simulation results, Case 3: Balanced distorted source voltages

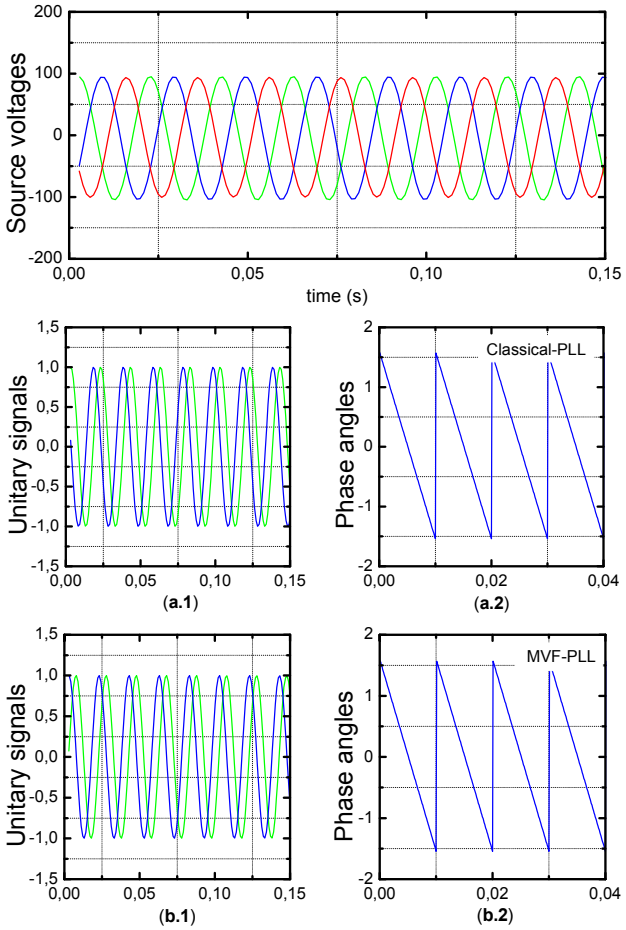

Fig. 13. Experimental results, Case 1: Balanced source voltages

Experimental validation. The proposed method performances are verified through simulation and experiment validations using Dspace 1104 platform as shown in Fig 12. Hardware parameters and control parameters used in experimental test are summarized in Table 1.

Fig. 12. Experimental platform

Table 1

Experimental parameters

V_s	V_{dc}	C_{dc}	l_f	K_{MVF}
110 V	300 V	1100 µF	4 mH	0.0001

Figure 13 presents the balanced three phase voltages. In this case both classical PLL and the proposed one success in extracting unitary signals that contains the phase angle information as shown in Figs. 13,a.1, a.2 and Figs. 13,b.1, b.2.

Figure 14 shows unbalanced three phase voltages expressed in taking-off the second phase. One can notice that, the classical PLL fails in extracting unitary signals as shown in Fig. 14,a.1 which leads to certain loss of phase angle information as presented in Fig. 14,a.2. On the other hand, the proposed MVF-PLL is motionless to this kind of unbalance and gives acceptable unit vectors and phase angle quality as shown in Fig. 14,b.1 and Fig. 14,b.2.

The last test is based on generating harmonics on the three phase source voltage as it generated in the simulation section. It is clear from Fig. 15 that the source voltages contain a huge amount of harmonics which weaken the classical PLL in extracting fundamental phase angle as shown in Fig. 15,a.1 and Fig. 15,a.2. Where, the MVF-PLL preserves its capability in giving true information in experiment tests as in simulation.

The aim of the second section of experimental study is dedicated to examine the dynamic voltage restorer under various conditions. Indeed, the first case is expressed in introducing a voltage sag in one phase by inserting a resistor in that phase in order to have the desired sag from t = 8:27 s to t = 8:44 s as it is shown in Fig. 16,a.1. The reference component required to compensate that sag is presented in Fig. 16,a.2. It is clear that, the DVR hits in rejecting the introduced voltage sag perfectly as it is illustrated in Fig. 16,a.3.

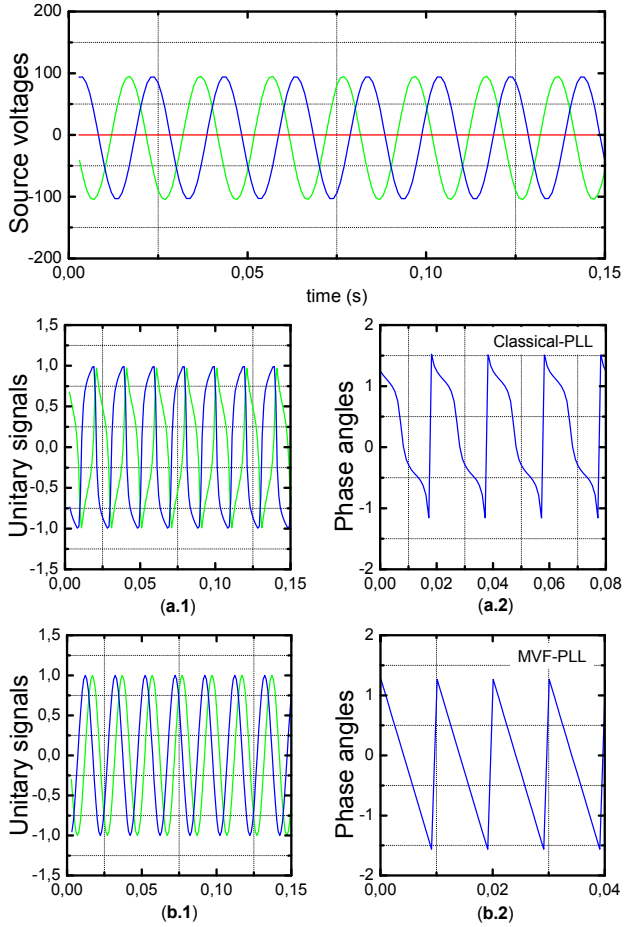

Fig. 14. Experimental results, Case 2: Unbalanced source voltages

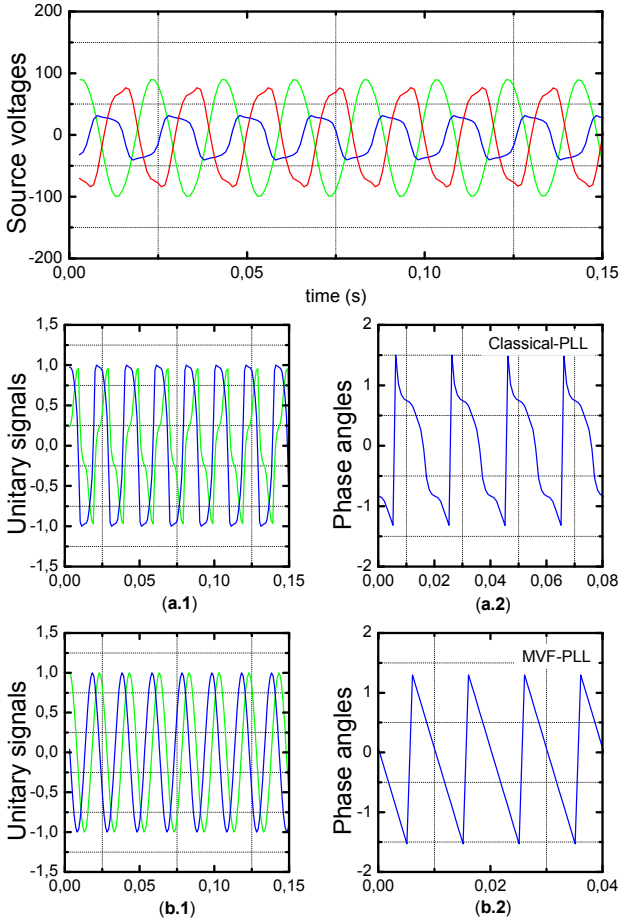

Fig. 15. Experimental results, Case 3: Balanced distorted source voltages

Fig. 16,b.1 presents a voltage sags of two phases in three phase source voltages from t = 1:65 s to t = 2:15 s. This case is considered as one of the most spread sags in the grid networks. From Fig. 16,b.2, one can notice that, the enhanced algorithm gives coherent reference voltages to compensate that occurred on the grid and make it balanced sinusoidal as shown in Fig. 16,b.3.

To put the dynamic voltage restorer under more sever conditions a three phase voltage sag is considered from t = 2:54 s to t = 2:67 s in the third test as shown in Fig. 16,c.1. The DVR stills generate the wanted voltages as shown in Fig. 16,c.2, to compensate the occurred sag on the grid and ensure the balanced three phase voltages of the grid, Fig. 16,c.3.

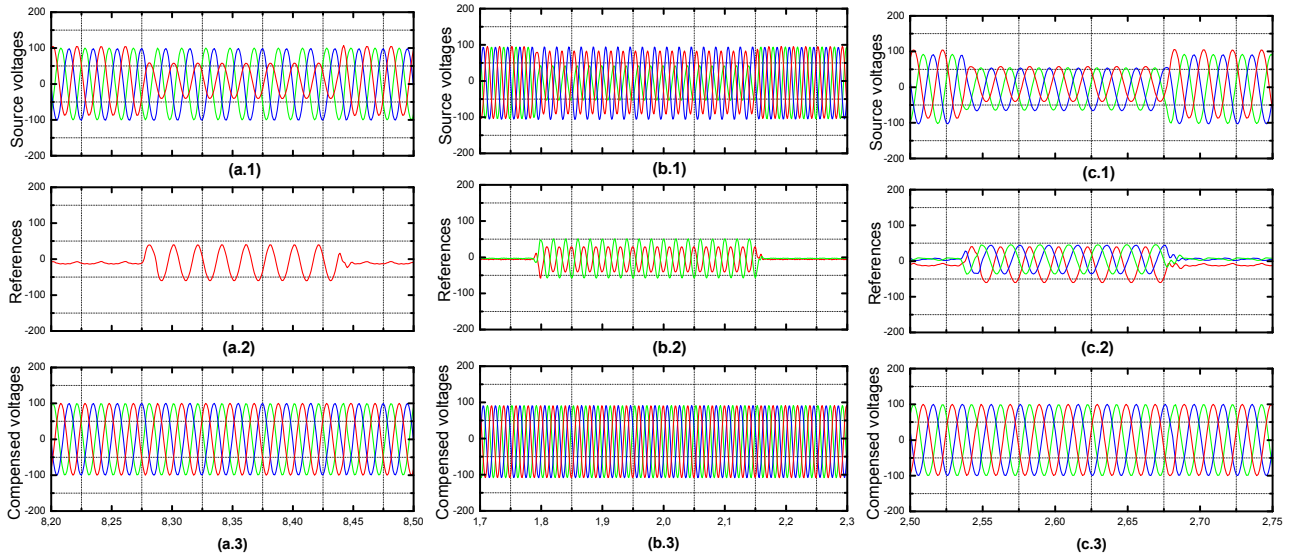

Fig. 16. Experimental results, DVR behavior under different conditions

Conclusions.

Voltage sag is a crucial problem for industries, indeed, it introduce malfunction for costumer's equipments. Researchers have investigated numerous solutions to mitigate the harmful effect of voltage sag. Dynamic voltage restorer is one of the most famous solutions. In this paper, authors have introduced an enhanced algorithm based on synchronous reference frame to control a dynamic voltage restorer for voltage sags rejection. The presented algorithm is based on a Multi variable filter in order to synthesis unitary signals containing fundamental phase angle information involved in generating necessary voltages for compensating the occurred sags. The considered algorithm is tested under different conditions such as single phase sag, two phase sag and three phase sag, on the other hand, the Multi variable filter configuration is examined under the most sever conditions such as a total phase exclusion and in the case of a huge account of harmonic presence, where elimination of harmonics is not our case of study in this paper but to show the effectiveness of the proposed algorithm in synthesizing the unitary signals. The efficiency of the introduced method is validated by simulation and experimental results.

Conflict of interest. The authors declare that they have no conflicts of interest.

REFERENCES

1. Patel A., Mathur H.D., Bhanot S. An improved control method for unified power quality conditioner with unbalanced load. *International Journal of Electrical Power & Energy Systems*, 2018, vol. 100, pp. 129-138. doi: https://doi.org/10.1016/j.ijepes.2018.02.035.

2. Pelz G.M., da Silva S.A.O., Sampaio L.P. Comparative analysis involving PI and state-feedback multi-resonant controllers applied to the grid voltage disturbances rejection of a unified power quality conditioner. *International Journal of Electrical Power & Energy Systems*, 2020, vol. 115, p. 105481. doi: https://doi.org/10.1016/j.ijepes.2019.105481.

3. Yazdi F., Hosseinian S.H. A novel "Smart Branch" for power quality improvement in microgrids. *International Journal of Electrical Power & Energy Systems*, 2019, vol. 110, p. 161-170. doi: https://doi.org/10.1016/j.ijepes.2019.02.026.

4. Krylov D.S., Kholod O.I. The efficiency of the active controlled rectifier operation in the mains voltage distortion mode. *Electrical Engineering & Electromechanics*, 2021, no. 2, pp. 30-35. doi: https://doi.org/10.20998/2074-272x.2021.2.05.

5. Philip M.A.D., Kareem P.F.A. Power conditioning using DVR under symmetrical and unsymmetrical fault conditions. *European Journal of Electrical Engineering*, 2020, vol. 22, no. 2, pp. 179-191. doi: https://doi.org/10.18280/ejee.220212.

6. Gongati P.R.R., Marala R.R., Malupu V.K.. Mitigation of certain power quality issues in wind energy conversion system using UPQC and IUPQC devices. *European Journal of Electrical Engineering*, 2020, vol. 22, no. 6, pp. 447-455. doi: https://doi.org/10.18280/ejee.220606.

7. Das C.K., Bass O., Kothapalli G., Mahmoud T.S., Habibi D. Overview of energy storage systems in distribution networks: Placement, sizing, operation, and power quality. *Renewable and Sustainable Energy Reviews*, 2018, vol. 91, pp. 1205-1230. doi: https://doi.org/10.1016/j.rser.2018.03.068.

8. Syvokobylenko V.F., Lysenko V.A. Improving the efficiency of fault protection systems of electrical grids based on zero sequence voltages and currents wavelet transforms. *Electrical Engineering & Electromechanics*, 2020, no. 4, pp. 67-72. doi: https://doi.org/10.20998/2074-272X.2020.4.09.

9. Boukhechem I., Boukadoum A., Boukelkoul L., Lebied R. Sensorless direct power control for three-phase grid side converter integrated into wind turbine system under disturbed grid voltages. *Electrical Engineering & Electromechanics*, 2020, no. 3, pp. 48-57. doi: https://doi.org/10.20998/2074-272X.2020.3.08.

10. Hossain E., Tür M.R., Padmanaban S., Ay S., Khan I. Analysis and mitigation of power quality issues in distributed generation systems using custom power devices. *IEEE Access*, 2018, vol. 6, pp. 16816-16833. doi: https://doi.org/10.1109/access.2018.2814981.

11. Deng Y., Jia H., Tong X., Dai Z., Qiu X., Wang L. Voltage sag identification based on deep learning method with gated recurrent unit. *2020 Chinese Automation Congress (CAC)*, 2020, pp. 1113-1117. doi: https://doi.org/10.1109/cac51589.2020.9327836.

12. Tu C., Guo Q., Jiang F., Chen C., Li X., Xiao F., Gao J. Dynamic voltage restorer with an improved strategy to voltage sag compensation and energy self-recovery. *CPSS Transactions on Power Electronics and Applications*, 2019, vol. 4, no. 3, pp. 219-229. doi: https://doi.org/10.24295/cpsstpea.2019.00021.

13. Li P., Xie L., Han J., Pang S., Li P. A New Voltage Compensation Philosophy for Dynamic Voltage Restorer to Mitigate Voltage Sags Using Three-Phase Voltage Ellipse Parameters. *IEEE Transactions on Power Electronics*, 2018, vol. 33, no. 2, pp. 1154-1166. doi: https://doi.org/10.1109/tpel.2017.2676681.

14. Han Y., Feng Y., Yang P., Xu L., Xu Y., Blaabjerg F. Cause, classification of voltage sag, and voltage sag emulators and applications: a comprehensive overview. *IEEE Access*, 2020, vol. 8, pp. 1922-1934. doi: https://doi.org/10.1109/access.2019.2958965.

15. Singh S., Letha S.S. Various custom power devices for power quality improvement: a review. *2018 International Conference on Power Energy, Environment and Intelligent Control (PEEIC)*, 2018, pp. 689-695. doi: https://doi.org/10.1109/PEEIC.2018.8665470.

16. Bhosale S.S., Bhosale Y.N., Chavan U.M., Malvekar S.A. Power quality improvement by using UPQC: a review. *2018 International Conference on Control, Power, Communication and Computing Technologies (ICCPCCT)*, 2018, pp. 375-380. doi: https://doi.org/10.1109/ICCPCCT.2018.8574264.

17. Karelia N., Sant A.V., Pandya V. Comparison of UPQC topologies for power quality enhancement in grid integrated renewable energy sources. *2019 IEEE 16th India Council International Conference (INDICON)*, 2019, pp. 1-4. doi: https://doi.org/10.1109/indicon47234.2019.9029108.

18. Gowtham N., Shankar S. UPQC: a custom power device for power quality improvement. *Materials Today: Proceedings*, 2018, vol. 5, no. 1, pp. 965-972. doi: https://doi.org/10.1016/j.matpr.2017.11.172.

19. Jin T., Chen Y., Guo J., Wang M., Mohamed M.A. An effective compensation control strategy for power quality enhancement of unified power quality conditioner. *Energy Reports*, 2020, vol. 6, p. 2167-2179. doi: https://doi.org/10.1016/j.egyr.2020.07.027.

20. Tooski P.Y., Eskandari B., Azizi M.R. Three-phase four-wire compensator in distribution system; Detailed simulation for implementation. *2018 9th Annual Power Electronics, Drives Systems and Technologies Conference (PEDSTC)*, 2018, pp. 206-211. doi: https://doi.org/10.1109/pedstc.2018.8343797.

21. Liu J., Xu W., Chan K.W., Liu M., Zhang X., Chan N.H.L. A three-phase single-stage AC–DC wireless-power-transfer converter with power factor correction and bus voltage control. *IEEE Journal of Emerging and Selected Topics in Power Electronics*, 2020, vol. 8, no. 2, pp. 1782-1800. doi: https://doi.org/10.1109/JESTPE.2019.2916258.

22. Aboelsaud R., Ibrahim A., Garganeev A.G. Review of three-phase inverters control for unbalanced load compensation. *International Journal of Power Electronics and Drive Systems (IJPEDS)*, 2019, vol. 10, no. 1, p. 242. doi: https://doi.org/10.11591/ijpeds.v10.i1.pp242-255.

23. Sarkar M.N.I., Meegahapola L.G., Datta M. Reactive power management in renewable rich power grids: a review of grid-codes, renewable generators, support devices, control strategies and optimization algorithms. *IEEE Access*, 2018, vol. 6, pp. 41458-41489. doi: https://doi.org/10.1109/access.2018.2838563.

24. Singh S.P., Bhat A.H. Design and performance evaluation of self-supported dynamic voltage restorer for mitigating various power quality problems. *International Journal of Power Electronics*, 2020, vol. 12, no 1, p. 54-84. doi: https://doi.org/10.1504/IJPELEC.2020.108386.

25. Sivaperumal P., Dash S.S., Saravanan K. Enhancing the power of quality issues using superconducting magnetic storage devices–based dynamic voltage restorer–aided switched coupled inductor inverter with space vector pulse width modulation techniques. *Measurement and Control*, 2019, vol. 52, no. 9-10, p. 1329-1343. doi: https://doi.org/10.1177/0020294019858169.

26. Manitha P.V., Nair M.G. Adapted synchronous reference frame based control for a dynamic voltage restorer. *2019 Innovations in Power and Advanced Computing Technologies (i-PACT)*, 2019, pp. 1-5. doi: https://doi.org/10.1109/i-pact44901.2019.8960020.

27. Ali Z., Christofides N., Hadjidemetriou L., Kyriakides E., Yang Y., Blaabjerg F. Three-phase phase-locked loop synchronization algorithms for grid-connected renewable energy systems: A review. *Renewable and Sustainable Energy Reviews*, 2018, vol. 90, pp. 434-452. doi: https://doi.org/10.1016/j.rser.2018.03.086.

28. Xia T., Zhang X., Tan G., Liu Y. Synchronous reference frame single-phase phase-locked loop (PLL) algorithm based on half-cycle DFT. *IET Power Electronics*, 2020, vol. 13, no. 9, pp. 1893-1900. doi: https://doi.org/10.1049/iet-pel.2019.1542.

29. Zou Z.-X., Rosso R., Liserre M. Modeling of the Phase Detector of a Synchronous-Reference-Frame Phase-Locked Loop Based on Second-Order Approximation. *IEEE Journal of Emerging and Selected Topics in Power Electronics*, 2020, vol. 8, no. 3, pp. 2534-2545. doi: https://doi.org/10.1109/jestpe.2019.2920309.

30. Hans F., Schumacher W., Harnefors L. Small-Signal Modeling of Three-Phase Synchronous Reference Frame Phase-Locked Loops. *IEEE Transactions on Power Electronics*, 2018, vol. 33, no. 7, pp. 5556-5560. doi: https://doi.org/10.1109/tpel.2017.2783189.

31. Patel S.R., Solanki M.D. Comparision of proportional integral and hysteresis controllers for controlling the DVR. *2018 2nd International Conference on Trends in Electronics and Informatics (ICOEI)*, May 2018. doi: https://doi.org/10.1109/icoei.2018.8553769.

32. Hung V.T., Shu H., Giang L.N., The N.D. Double-loop control structure using proportional resonant and sequence-decoupled resonant controllers in static coordinates for dynamic voltage restorer. *Chinese Journal of Electrical Engineering*, 2019, vol. 5, no. 3, pp. 10-19. doi: https://doi.org/10.23919/cjee.2019.000016.

33. Sathik Basha A., Ramasamy M. Design of Z-source inverter-based dynamic voltage restorer circuitry with R-SOGI control scheme for enrichment of power quality. *Journal of Circuits, Systems and Computers*, 2021, p. 2150195. doi: https://doi.org/10.1142/s0218126621501954.

34. Huchche V.A., Patne N.R., Junghare A.S. Mitigating voltage sags using FOPI and fuzzy logic controllers in induction motors. *2017 IEEE International Conference on Power, Control, Signals and Instrumentation Engineering (ICPCSI)*, Sep. 2017. doi: https://doi.org/10.1109/icpcsi.2017.8392281.

35. Zhao J., Mili L. A Decentralized H-Infinity Unscented Kalman Filter for Dynamic State Estimation Against Uncertainties. *IEEE Transactions on Smart Grid*, 2019, vol. 10, no. 5, pp. 4870-4880. doi: https://doi.org/10.1109/tsg.2018.2870327.

36. Biricik S., Komurcugil H., Tuyen N.D., Basu M. Protection of sensitive loads using sliding mode controlled three-phase DVR with adaptive notch filter. *IEEE Transactions on Industrial Electronics*, 2019, vol. 66, no. 7, pp. 5465-5475. doi: https://doi.org/10.1109/tie.2018.2868303.

37. Komurcugil H., Biricik S., Babaei E. Super Twisting Algorithm Based Sliding Mode Control Method for Single-Phase Dynamic Voltage Restorers. *2019 2nd International Conference on Smart Grid and Renewable Energy (SGRE)*, 2019, pp. 1-6. doi: https://doi.org/10.1109/sgre46976.2019.9020687.

38. Biricik S., Komurcugil H., Ahmed H., Babaei E. Super Twisting Sliding Mode Control of DVR with Frequency-Adaptive Brockett Oscillator. *IEEE Transactions on Industrial Electronics*, 2020. Article in Press. doi: https://doi.org/10.1109/TIE.2020.3038089.

39. SasiKiran P., Manohar T.G. UKF based estimation approach for DVR control to compensate voltage swell in distribution systems. *Ain Shams Engineering Journal*, 2018, vol. 9, no. 4, pp. 441-453. doi: https://doi.org/10.1016/j.asej.2016.02.001.

40. Trabelsi M., Komurcugil H., Refaat S.S., Abu-Rub H. Model predictive control of packed U cells based transformerless single-phase dynamic voltage restorer. *2018 IEEE International Conference on Industrial Technology (ICIT)*, 2018, pp. 1926-1931. doi: https://doi.org/10.1109/icit.2018.8352480.

41. Trabelsi M., Vahedi H., Komurcugil H., Abu-Rub H., Al-Haddad K. Low complexity model predictive control of PUC5 based dynamic voltage restorer. *2018 IEEE 27th International Symposium on Industrial Electronics (ISIE)*, 2018, pp. 240-245. doi: https://doi.org/10.1109/isie.2018.8433616.

42. Taher S.A., Fard H.T., Kashani E.B. New switching approach for DVR using one cycle control method. *Ain Shams Engineering Journal*, 2018, vol. 9, no. 4, pp. 2227-2254. doi: https://doi.org/10.1016/j.asej.2017.03.003.

43. Van T.L., Nguyen N.M.D., Toi L.T., Trang T.T. Advanced control strategy of dynamic voltage restorers for distribution system using sliding mode control input-output feedback

linearization. *International Conference on Advanced Engineering Theory and Applications*. Springer, Cham, 2017. p. 521-531. doi: https://doi.org/10.1007/978-3-319-69814-4_50.

44. Mythily G., Lakshmi Kumari S.V.R. Power quality improvement by IUPQC. *2018 International Conference on Inventive Research in Computing Applications (ICIRCA)*, Jul. 2018. doi: https://doi.org/10.1109/icirca.2018.8597191.

Received 24.05.2021
Accepted 25.06.2021
Published 27.08.2021

Abdelfettah Boussaid [1, 2]*, Doctor of Electrical Engineering, Professor,*
Seif El Islam Chelli [2]*, PhD Student,*
Ahmed Lokmane Nemmour [2]*, Doctor of Electrical Engineering, Professor,*
Abdelmalek Khezzar [2]*, Doctor of Electrical Engineering, Professor,*
[1] Institut des Sciences et des Techniques Appliquées, University Frères Mentouri Constantine 1, Algeria,
[2] Laboratoire d'électrotechnique de Constantine, University Frères Mentouri Constantine 1, Algeria,
e-mail: Abdlfettah.Boussaid@lec-umc.org (Corresponding author),
seif-elislam.chelli@lec-umc.org
Ahmed-Lokmane.Nemmour@lec-umc.org
abdelmalek.khezzar@lec-umc.org

How to cite this article:
Boussaid A., Chelli S.E.I., Nemmour A.L., Khezzar A. An effective control algorithm for dynamic voltage restorer under symmetrical and asymmetrical grid voltage conditions. *Electrical Engineering & Electromechanics*, 2021, no. 4, pp. 53-63. doi: https://doi.org/10.20998/2074-272X.2021.4.07.

UDC 62-838: 629.423 https://doi.org/10.20998/2074-272X.2021.4.08

V.I. Omelyanenko, Ie.S. Riabov, L.V. Overianova, H.V. Omelianenko

TRACTION ELECTRIC DRIVE BASED ON FUEL CELL BATTERIES AND ON-BOARD INERTIAL ENERGY STORAGE FOR MULTI UNIT TRAIN

*The **aim** of the work is to study the possibility and features of the use of inertial storage devices in the traction electric drive of multi unit train with a power plant based on fuel cells. **Methodology**. The principle of power flow control in traction electric drives in the modes of acceleration and braking of rolling stock is proposed. The mathematical model of the traction electric drive in the form of the combination of three components: the train, the traction unit and the battery of fuel cells is developed. It was used to study the operation of a traction electric drive when solving a test traction task for rolling stock. **Results**. It is established that the use of inertial energy storage reduces hydrogen consumption by at least 25 %, which increases the mileage of rolling stock between equipment by more than 30 %. **Originality**. The traction electric drive on the basis of fuel elements and the inertial energy storage for the multi unit train is offered. The work of the proposed traction electric drive in solving the test traction problem for rolling stock is investigated. **Practical significance.** A mathematical model of the traction electric drive has been developed. The test traction problem for rolling stock is solved.* References 16, tables 4, figures 6.
Key words: **traction electric drive, fuel cell, inertial storage, multi unit train.**

В роботі розглянуто тяговий електропривод на основі паливних елементів та інерційного накопичувача енергії для мотор-вагонного рухомого складу. Запропоновано принцип керування потоками потужності у тяговому електроприводі у режимах розгону та гальмування рухомого складу. Розроблено математичну модель тягового електропривода у вигляді сукупності трьох складових: поїзда, тягового блока і батареї паливних елементів. За допомогою неї досліджено роботу запропонованого тягового електроприводу при вирішенні тестової тягової задачі для рухомого складу. Встановлено, що застосування інерційного накопичувача енергії зменшує витрати водню не менш ніж на 25 %, що забезпечує збільшення пробігу рухомого складу між екіпіруванням понад 30 %. Бібл. 16, табл. 4, рис. 6.
Ключові слова: **тяговий електропривод, паливний елемент, інерційний накопичувач, мотор-вагонний рухомий склад.**

В работе рассмотрены тяговый электропривод на основе топливных элементов и инерционного накопителя энергии для мотор-вагонного подвижного состава. Предложен принцип управления потоками мощности в тяговом электроприводе в режимах разгона и торможения подвижного состава. Разработана математическая модель тягового электропривода в виде совокупности трех составляющих: поезда, тягового блока и батареи топливных элементов. С помощью нее исследована работа предложенного тягового электропривода при решении тестовой тяговой задачи для подвижного состава. Установлено, что при применении инерционного накопителя энергии уменьшается расход водорода не менее чем на 25 %, что обеспечивает увеличение пробега подвижного состава между экипировками более чем на 30 %. Библ. 16, табл. 4, рис. 6.
Ключевые слова: **тяговый электропривод, топливный элемент, инерционный накопитель, мотор-вагонный подвижной состав.**

Introduction. Fuel cells as the basis for efficient and environmentally friendly power supply systems are currently of interest in terms of their use on rolling stock by replacing conventional diesel trains on non-electrified railway lines with multi unit «hydrogen» trains [1, 2]. To date, several global manufacturers have created rolling stock using fuel cells [3]. For the first time, fuel cells on rolling stock were used on prototype trains by JR East Company and the RTRI Research Center in Japan. In the USA, fuel cells were installed on a BNSF shunting diesel locomotive for research and trial operation. After extensive testing of the «hydrogen» trains iLINT (developed by Alstom) and Mireo Plus H (developed by Siemens), these Companies have entered into contracts for the commercial supply of fuel cell trains. Spanish Companies CAF and Talgo are planning the modernization and creation of multi unit trains using fuel cells. However, the use of fuel cells on rolling stock has a number of features due to the specificity of the traction drive, which is characterized by a wide range of changes in load and rotation speed.

Analysis of literature data and problem definition. An integral part of a fuel cell power plant is an energy storage device, the use of which increases the efficiency of using fuel cells on a rolling stock. In existing projects, only lithium-ion batteries are considered as energy storage [3-5]. Inertial energy storage units remain out of sight for such trains [5]. However, despite the successes in the development of electrochemical storage devices, we consider it expedient to study and investigate all available technical solutions for energy storage devices, the use of which contributes to an increase in the energy and resource efficiency of rolling stock.

The analysis [6-9] showed that the specific weight energy indicators of capacitor, electrochemical and inertial storage devices have practically the same order of 0.02-0.08 MJ/kg. As for the specific volumetric energy indicators, here inertial ones are superior to other types [6]: 25.7-151 MJ/m^3 for inertial ones and 0.6-17.3 MJ/m^3 for other types. The same picture is observed with weight, as well as volumetric specific power indicators: 1.29-2.5 kW/kg and 536-4273 kW/m^3 for inertial ones, as well as 0.16-0.26 kW/kg and 54-173 kW/m^3 for other types. Therefore, we can say that inertial energy storage devices are significantly superior to capacitor and electrochemical storage devices in terms of their specific energy and power indicators. But, unlike electrochemical

storage devices, which are widely used on various vehicles and the features of their application in traction electric drives have been studied quite well, the use of inertial storage devices on vehicles is limited [9-13].

The goal of the work is a study of the possibility and peculiarities of using inertial storage devices in the traction electric drive of multi unit trains with a power plant based on fuel cells.

To achieve this goal, two tasks were solved. The first one is to create a general mathematical model of a traction electric drive of the regional multi unit train with an autonomous power source based on a battery of fuel cells and an on-board inertial energy storage device, which would link the main parameters of the power plant components with the operating properties of this drive and adequately reflect all modes of its operation. The second one is to test the created model using the example of a conceptual project of a regional train moving along a specific non-electrified section of the railway.

1. Diagram of a traction electric drive and power flows. Traction electric drive diagram shown in Fig. 1, includes the following components: a source of electrical energy, a storage device and an actuator. The source of electrical energy is represented by a hydrogen storage system (HFT), a fuel cell (FC) and a P_DC-DC converter. The storage device is represented by an inertial energy accumulator FESS and an S_DC-DC converter. The actuator (DM) consists of an induction traction motor (IM), a gearbox (G) and a wheel-rail (W-R) mechanism. The output of the P_DC-DC converter and the input of the autonomous voltage inverter (TI) are connected by a DC bus, to which FESS, an auxiliary power system (AS), and a braking resistor block (BR) are connected in parallel through the corresponding semiconductor converters.

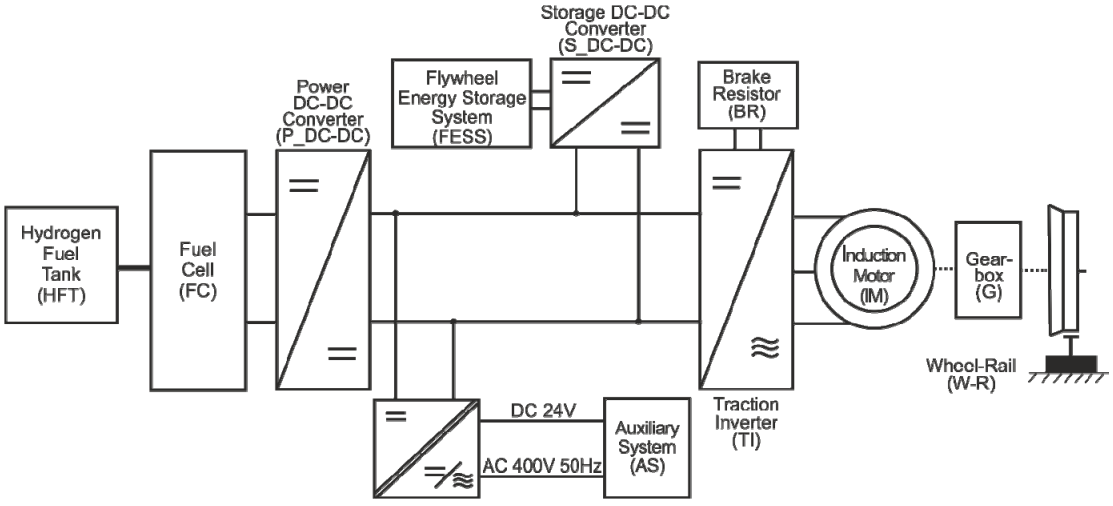

Fig. 1. Traction drive block diagram:

HFT – hydrogen storage system; FC – fuel cell battery; P_DC-DC – DC voltage converter of the fuel cell battery; FESS – energy storage; S_DC-DC – storage DC converter; AS – auxiliary power supply system; BR – block of braking resistors; TI – autonomous voltage inverter; IM – traction induction motor; G – gearbox; W-R – wheel-rail mechanism

The calculation diagrams of power flows between the main nodes of the traction electric drive diagram for various operating modes of the rolling stock were determined by us, based on the following assumptions.

The nominal electric power of the fuel cell battery P_{fc} is determined based on the requirement to ensure the driving mode with the maximum permissible speed, as well as the operation of auxiliary devices P_{as}. That is, the condition must be met

$$P_{fc} = P_p + P_{as}\,, \tag{1}$$

where P_p is the power supplied to the traction unit.

Here, the power consumed by auxiliary devices, in any modes of movement of the rolling stock, is taken as a constant value P_{as} = const.

The value of the energy intensity and power of the storage device are taken such that they are able to provide, together with FC, the required modes of acceleration and braking of the rolling stock. Therefore, the braking resistor link BR can be excluded from consideration.

Diagrams of power flows in the modes of braking and acceleration of the rolling stock are shown in Fig. 2. It is obvious that for the adopted scheme of the traction electric drive, the power flows are determined by the values of the currents in the corresponding branches. We will consider the processes from the standpoint of the storage device.

Braking mode.

The current I_{ch} consumed by the drive in this operating mode, in accordance with the 1st Kirchhoff law

$$I_{ch} = I_{inv} - I_{as} + I_{dc}\,. \tag{2}$$

Current I_{inv} due to IM operation in generator mode:

$$I_{inv} = \frac{P_{wr}}{U_{dc}}\eta_{\Sigma} = \frac{\sqrt{3}}{U_{dc}}U_m I_m \eta_{inv}\cos\varphi_m\,, \tag{3}$$

where $\eta_{\Sigma} = \eta_g\eta_m\eta_{inv}$ is the total efficiency of the DM link of the traction block; $\cos\varphi_m$ is the power factor of the IM; η_g, η_m, η_{inv} are the efficiencies of the gearbox, IM and TI, respectively.

Current consumed by auxiliary devices:

$$I_{as} = P_{as}/U_{dc}\,. \tag{4}$$

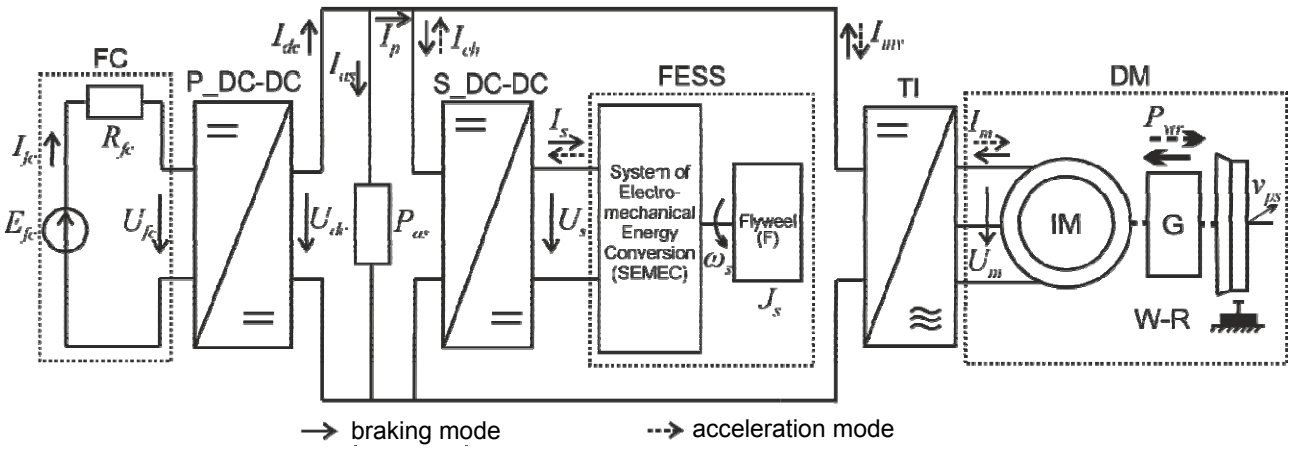

Fig. 2. Calculation diagram of the braking and acceleration modes:
I_{fc} – current of the FC; I_{dc} – current on the output of the P_DC-DC; I_p – current supplied to the traction block; I_{as} – auxiliary current; I_{ch} – current on the input of the S_DC-DC; I_s – current of the FESS; I_{inv} – current of the TI; I_m – current of the IM; U_{fc}, U_{dc}, U_s, U_m –FC, DC link, SEMEC and IM voltages, respectively; E_{fc} – electromotive force (EMF) of the FC; R_{fc} – active resistance of the FC; P_{wr} – rim power; ω_s, J_s – flywheel F speed and moment of inertia; v_{ps}– train speed

FC current:

$$I_{dc} = \frac{U_{fc}\eta_{fc}}{U_{dc}} I_{fc}, \quad (5)$$

where η_{fc} is the efficiency of the FC.

As a result, the power consumed by the storage device is supplied to the storage electromechanical energy conversion (SEMEC) system by current

$$I_{ch} = \frac{\sqrt{3}}{U_{dc}} U_m I_m \eta_{inv} \cos\varphi_m - \frac{P_{as}}{U_{dc}} + \frac{U_{fc}\eta_{fc}}{U_{dc}} I_{fc}. \quad (6)$$

Based on the power balance for the storage device

$$U_{dc} I_{ch} \eta_{s\_dc} = U_s I_s, \quad (7)$$

where η_{s_dc} is the efficiency of the P_DC-DC, and the current consumed by the SEMEC of the storage device is

$$I_s = \frac{U_{dc} I_{ch} \eta_{s\_dc}}{U_s}. \quad (8)$$

As a result, we get the accumulation of energy by the storage device in the process of braking of the rolling stock in the form of an increase in the rotation frequency of its flywheel

$$\frac{d\omega_s}{dt} = \frac{U_s I_s \eta_s}{J_s \omega_s}, \quad (9)$$

where η_s is the efficiency of the FESS.

Acceleration mode.

Here IM consumes the electricity generated by the FC minus the energy used for its own needs, as well as the energy stored by the storage device.

In this mode, the current supplied by the storage device, in accordance with the 1st Kirchhoff law, is defined as

$$I_{ch} = I_{inv} + I_{as} - I_{dc}. \quad (10)$$

The current consumed by the autonomous traction inverter

$$I_{inv} = \frac{P_{wr}}{U_{dc}\eta_{\Sigma}} = \frac{\sqrt{3}}{U_{dc}\eta_{inv}} U_m I_m \cos\varphi_m. \quad (11)$$

Provided that the expressions for the current consumed by the auxiliary devices and generated by the FC remain the same – (4) and (5), respectively, the power generated by the SEMEC of the storage device is supplied to the DC link by current

$$I_{ch} = \frac{\sqrt{3}}{U_{dc}\eta_{inv}} U_m I_m \cos\varphi_m + \frac{P_{as}}{U_{dc}} - \frac{U_{fc}\eta_{fc}}{U_{dc}} I_{fc}. \quad (12)$$

From the power balance for the SEMEC of the storage device in this mode

$$U_{dc} I_{ch} = U_s I_s \eta_{s\_dc} \quad (13)$$

we get the current supplied by the SEMEC of the storage device, in the following form

$$I_s = \frac{U_{dc}}{U_s \eta_{s\_dc}} I_{ch}. \quad (14)$$

The mechanical power spent on the acceleration of the train, taken from the flywheel of the storage device, is fed through the SEMEC to the S_DC-DC

$$N = J_s \omega_s \frac{d\omega_s}{dt} \eta_s = U_s I_s. \quad (15)$$

As a result, in the process of acceleration, we get a decrease in the energy stored by the flywheel due to a decrease in the frequency of its rotation.

$$\frac{d\omega_s}{dt} = \frac{U_s I_s}{J_s \omega_s \eta_s}. \quad (16)$$

Thus, from the above relationships, it is obvious that with the required power on the wheel rims P_{wr} and the available power of the FC P_{fc}, the presence of an energy storage device in the traction electric drive circuit allows organizing power flows between its components in any operating modes of the rolling stock (by analogy with those discussed above, also in the driving modes with constant speed, coasting and parking). The voltage relationships at the inputs and outputs of the power parts of the semiconductor converter circuits (P_DC-DC, S_DC-DC, TI), through which FC, FESS and DM are connected to the DC link bus act as a regulator of these flows.

2. Traction drive mathematical model.

We represent the mathematical model of the considered traction drive in the form of a combination of three components: a train, a traction block, and a battery of fuel cells.

Mathematical model of a train.

The traction or braking force of the rolling stock $\pm F_t$ in the entire speed range is determined by the power on the rim of the wheels $P_{wr}=\pm F_t v_{ps}$ which is due to the total power of the traction motors on the axles of the wheelsets equipped with motors.

If we assume that a train with mass m_{ps} concentrated at one point moves along a track of length s at time t at speed v_{ps}, has acceleration dv_{ps}/dt, experiences force of resistance to motion F_{rr}, gravitational force from the slope of the track F_g, as well as force of resistance from motion in the curves F_c and at the same time traction motors provide the traction or braking force F_t, then the relationship of the distance traveled by the train and the speed with time, as well as with the forces acting on it, is represented in the form of a system

$$\begin{cases} \dfrac{dv_{ps}}{dt} = \dfrac{\pm F_t - F_{rr} \pm F_g - F_c}{(1+\varepsilon)m_{ps}}; \\ \dfrac{ds}{dt} = v_{ps}. \end{cases} \tag{17}$$

where $(1+\varepsilon)$ is the coefficient of the rotating mass of the train.

The resistance to motion due to the rolling friction of the wheels on the rails and the aerodynamics of the train is determined using the Davis formula

$$F_{rr} = A_{rr} + B_{rr} v_{ps} + C_{rr} v_{ps}^2, \tag{18}$$

where A_{rr}, B_{rr}, C_{rr} are the constant coefficients depending on the configuration of the train.

These coefficients are due to the following: A_{rr} – rolling friction of wheels on rails and friction of axles of wheel pairs; B_{rr} – friction of the wheel flanges against the side surfaces of the rail head; C_{rr} – train aerodynamics.

The gravitational force from the slope is calculated using the equality:

$$F_g = 0{,}001 m_{ps} g i, \tag{19}$$

where g s the acceleration of gravity; i is the slope of the track.

The drag force from movement in curves for trains of the class under consideration is determined using the expression

$$F_c = \frac{0{,}006867}{R} m_{ps}, \tag{20}$$

where R is the curve radius.

Thus, the presented model shows that for given track parameters and restrictions on the speed of rolling stock on its sections, the curves of movement are determined by the power on the rim of the wheels P_{wr}. By varying P_{wr} by changing its constituent components, it is possible to regulate the required traction force and the speed of the rolling stock.

Mathematical model of the traction block.

By the traction block we denote a part of the traction electric drive circuit, including FESS and DM, which, through the S_DC-DC and TI converters, respectively, are fed by the so-called traction current I_p, which is formed by the FC current I_{dc} minus the current of auxiliary consumers I_{as}

$$I_p = \frac{U_{fc} I_{fc} \eta_{p\_dc}}{U_{cd}} - I_{as}, \tag{21}$$

where η_{p_dc} is the efficiency of the P_DC-DC.

At this stage of research, this current will be considered given and unchanged. This assumption implies the exchange of energy only within the traction block, that is, between the DM actuator and the FESS storage device, and the operation of the P_DC-DC converter in a static mode with a specific conversion factor.

The central link of the traction block is an inertial energy storage device. FESS is a combination of an annular cylindrical flywheel (accumulator) and a SEMEC electromechanical energy converter system in the form of a inverted DC machine with excitation from permanent magnets and a semiconductor switch [12, 13].

The SEMEC diagram is shown in Fig. 3. Here we are dealing with a two-pole four-phase machine, each phase of which contains one coil, displaced along the circumference of the armature by an angle proportional to τ/ N_f, where N_f is the number of phases, and τ is the pole division.

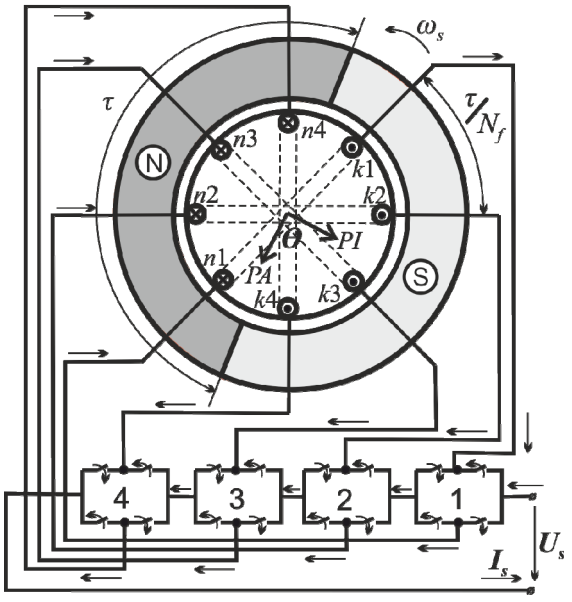

Fig. 3. System for electromechanical energy conversion of storage device:
θ –load angle between the axis of the magnetic field of the inductor PI and the armature current PA; $n1...n4$, $k1...k4$ – beginnings and ends of the winding coils, respectively; 1…4 – switches

Mathematical models of the operation of the traction block in acceleration and braking modes are presented in Table 1.

As follows from the formula for the EMF of the drive of the SEMEC (Table 1), in the system under

consideration it is possible to regulate the value of the electromotive force in two channels – by the number of phases of the armature winding and by the load angle, changing the switching algorithm of semiconductor switches. Thus, during the exchange of energy of the storage device and the link of electromechanical energy conversion, it is possible to influence both the power of the process and its components within wide ranges.

The meaning of the symbols in expressions presented in Table 1 is the following: η_s, e_s, L_s, R_s – the efficiency, the EMF, the inductance and the active resistance of the storage device armature winding, respectively; $2p$, w_s, l_a, a – the number of poles, the number of turns per phase, the active length and the number of parallel branches of the storage device SEMEC armature winding, respectively; D_a – the armature diameter; B_{sr} – the average value of the magnetic flux density in the gap; $\eta_{sum}=\eta_g\eta_m\eta_{inv}\eta_{s\_dc}\eta_s$ – the overall efficiency of the transmission; f_{rr} – the specific value of resistance to movement; L_{s_dc}, R_{s_dc} – the inductance and active resistance of the converter, respectively; K_{chT}, K_{chB} – the conversion factors in acceleration and braking modes, respectively.

Table 1

Traction block mathematical model [14]

Acceleration mode	Braking mode
Storage device power balance	
$-J_s\frac{d\omega_s}{dt}\omega_s\eta_s=u_s i_s$	$J_s\frac{d\omega_s}{dt}\omega_s=u_s i_s\eta_s$
Equilibrium equation for voltage on the SEMEC	
$u_s=e_s-L_s\frac{di_s}{dt}-i_s R_s$	$u_s=e_s+L_s\frac{di_s}{dt}+i_s R_s$
Power developed by the rolling stock	
$(m_{ps}\frac{dv_{ps}}{dt}-F_{rr})v_{ps}=u_{dc}i_{inv}\eta_{inv}\eta_m\eta_g$	$-(m_{ps}\frac{dv_{ps}}{dt}-F_{rr})v_{ps}\eta_{inv}\eta_m\eta_g=u_{dc}i_{inv}$
EMF of the storage device SEMEC	
$e_s=K_e\omega_s$, $K_e=\frac{2pw_s N_f l_a D_a}{a}\sin\theta\cdot B_{sr}$	
DC link current	
$K_{chT}=\frac{U_{dc}}{U_s}$, $i_{inv}=i_{ch}+i_p=\frac{i_s\eta_{s\_dc}}{K_{chT}}+i_p$	$K_{chB}=\frac{U_s}{U_{dc}}$, $i_{inv}=i_{ch}-i_p=\frac{i_s K_{chB}}{\eta_{s\_dc}}-i_p$
Mathematical model of the energy conversion process	
$\begin{cases}\frac{dv_{ps}}{dt}=\frac{\eta_{inv}\eta_m\eta_g u_{dc}(i_s\eta_{s\_dc}/K_{chT}+i_p)}{m_{ps}v_{ps}}+f_{rr};\\ \frac{di_s}{dt}=\frac{K_e\omega_s-u_{dc}/K_{chT}-i_s(R_s+R_{s\_dc})}{L_s+L_{s\_dc}};\\ -\frac{d\omega_s}{dt}=\frac{1}{J_s\eta_s}K_e i_s\end{cases}$	$\begin{cases}\frac{dv_{ps}}{dt}=-\frac{u_{dc}(i_s\eta_{s\_dc}/K_{chB}-i_p)}{\eta_{inv}\eta_m\eta_g m_{ps}v_{ps}}-f_{rr};\\ \frac{di_s}{dt}=\frac{u_{dc}/K_{chB}-K_e\omega_s-i_s(R_s+R_{s\_dc})}{L_s+L_{s\_dc}};\\ \frac{d\omega_s}{dt}=\frac{\eta_s}{J_s}K_e i_s\end{cases}$
The relationship between the rotational speed of the storage device rotor and the speed of the rolling stock	
$\omega_{s(k+1)}=\sqrt{\omega_{sk}-\frac{m_{ps}(v^2_{ps(k+1)}-v^2_{psk})}{J_s\eta_{sum}}}$	$\omega_{s(k+1)}=\sqrt{\omega_{sk}+\frac{m_{ps}\eta_{sum}(v^2_{psk}-v^2_{ps(k+1)})}{J_s}}$

It is important to note that the model includes two adjustable components – the storage device SEMEC EMF (K_e) and the DC link current (K_{ch}), the impact on which provides a controlled power flow between the components of the traction block circuit.

The control of the process of power exchange in the modes of acceleration and braking of the rolling stock is implemented in software in accordance with the diagram shown in Fig. 4 (braking mode), based on logic gates [14].

The control block (CB) implements the following functions:

$$f_{ch}(T_{set}, v_{ps}) = K_{ch0} + (K_{psch} / T_{set}) v_{ps},$$

$$f_e(T_{set}, v_{ps}) = K_{e0} v_{ps}^2 + (K_{pse} / T_{set}) v_{ps}.$$

In this case, the following conditions are met.

For braking mode:

1. If the inverter current $i_{inv} \in [i_{\min};\ i_{\max}]$, then $K_{ch}=f_{ch}(T_{set},v_{ps})$, $K_e=f_e(T_{set},v_{ps})$.
2. If $i_{inv}>i_{\max}$, then $K_{ch}=K_{ch\,\max}$, $K_e=K_{e\,\max}$.
3. If $i_{inv}<i_{\min}$, then $K_{ch}=K_{ch\,\min}$, $K_e=f_e(T_{set},v_{ps})/4$.

For acceleration mode:

1. If the inverter current $i_{inv} \in [i_{\min};\ i_{\max}]$, then $K_{ch}=f_{ch}(T_{set},v_{ps})$, $K_e=f_e(T_{set},v_{ps})$.
2. If $i_{inv}>i_{\max}$, then $K_{ch}=K_{ch\,\min}$, $K_e=f_e(T_{set},v_{ps})/4$.
3. If $i_{inv}<i_{\min}$, then $K_{ch}=K_{ch\,\max}$, $K_e=K_{e\,\max}$.

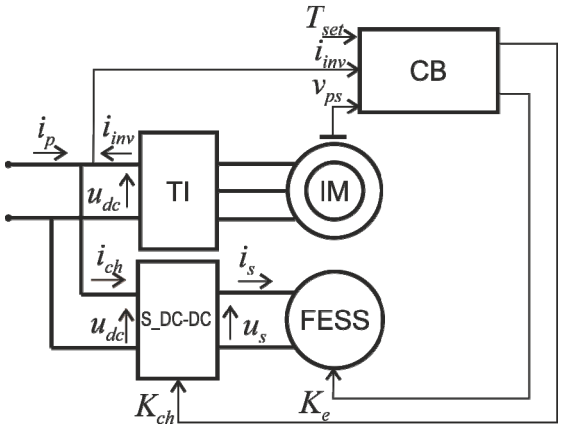

Fig. 4. Control system

To assess the properties of the storage device operation in the traction electric drive system, the efficiency factor of the storage device was proposed [14]:

$$K_{efs} = \frac{J_s(\omega_{send}^2 - \omega_{sdv}^2)}{m_{ps}(v_{psstB}^2 + v_{psendT}^2)}, \qquad (22)$$

where v_{psstB} is the rolling stock speed at the start of braking; v_{psendT} is the rolling stock speed at the end of acceleration; ω_{send} is the storage device rotor rotation frequency at the end of recuperation; ω_{sdv} is the rotation frequency of «dead volume».

Thus, a mathematical model of the traction block is obtained, which connects the process of train movement in modes of acceleration as well as regenerative braking, with the parameters of an inertial energy storage device, characteristics of a traction motor and converters of a traction electric drive. The control system formed on the basis of logical elements programmatically implements power flows in the considered operating modes of the rolling stock between the traction motors, the storage device and the battery of fuel cells (currents i_{inv}, i_{ch}, i_p, respectively). A criterion for assessment of the efficiency of using the technology under consideration is proposed.

Mathematical model of the fuel cell.

The mathematical model of the fuel cell (FC) is clear from the diagram shown in Fig. 2. The main electrical characteristics of the fuel cell are: EMF E_{fc}, output voltage U_{fc}, internal electrical resistance R_{fc}, electrical power P_{fc}, electrical efficiency η_E [16, 17].

The power transmitted to the external load (useful power) is equal to:

$$P_{fc} = U_{fc} I_{fc} = I_{fc} E_{fc} - I_{fc}^2 R_{fc}. \qquad (23)$$

Electrical power dissipated on the internal resistance:

$$P_{fci} = (E_{fc} - U_{fc}) I_{fc} = \frac{(E_{fc} - U_{fc})^2}{R_{fc}} = I_{fc}^2 R_{fc}. \qquad (24)$$

In the above interpretation of powers, the electrical efficiency is will be equal to:

$$\eta_E = \frac{P_{fc}}{P_{fci} + P_{fc}} = \frac{U_{fc}}{E_{fc}}. \qquad (25)$$

Information about the fuel cell and the clarity of its perception is contained in its volt-current plot (VCP). It is a graphical plot of fuel cell voltage versus load current. In most cases, the VCP of solid oxide fuel cells is a straight line. Strictly speaking, the initial and final sections of the VCP have deviations from a straight line, respectively, up and down (due to the electrochemical polarization of the electrodes for the final section). In most cases, these deviations are insignificant and practically do not go beyond 10-15 % of the beginning and end of the VCP curve section, and in some cases they are not observed at all. The middle section of the VCP is more important. Here, with some approximation, it can be assumed that the point of intersection of the VCP line with the voltage axis characterizes the EMF of the element, and the point of intersection of the VCP with the current axis characterizes the short circuit current of the element. The VCP is well approximated by a first order polynomial

$$\begin{aligned} y &= -kx + b, \\ U_{fc} &= -I_{fc} R_{fc} + E_{fc}, \end{aligned} \qquad (26)$$

where y and x are the coordinates of voltage and current; k is the slope equal to tangent α – the angle of inclination of the VCP line to the current axis; b is the value of the segment that cuts off the VCP line on the voltage axis (in our case, b is equal to E_{fc} of the element).

3. Conceptual design.

The task of developing a conceptual design is to select the parameters of a traction block, an inertial energy storage device and a fuel cell battery (in conjunction with a hydrogen storage cell) by solving the traction problem and analyzing the results obtained. Converting units (P_DC-DC, S_DC-DC, TI) will be considered only from the standpoint of the possibility of providing with their help the required energy flows between the blocks under consideration. It is obvious that their efficient operation will take place provided that the nominal values of the power components of the devices under consideration are as close as possible. With the unconditional observance of the power balance and based on the fact that the mentioned units of the traction drive in the DC link are connected in parallel, we believe that the voltage values of these units should be as close as possible. Fulfillment of this condition, in our opinion,

will become the basis for effective regulation of power flows in various modes of operation of electric rolling stock (ERS).

When choosing the parameters of the traction drive units, we will proceed from the fact that the powers of the fuel cell block and the energy storage device are practically the same and the storage device operates only during acceleration and braking of the train, and in the mode of movement at a steady speed, the system is supplied with energy only from the fuel cell battery.

For calculation we take: train length is 42 m, composition – 2 cars, tare weight is 92 tons, car passenger capacity – 280 people, car bodies rest on 3 bogies – two end biaxial and one intermediate biaxial Jacobs bogie, design speed is 124 km/h. Basic resistance to movement is calculated by the formula F_{rr}=1,5+0,006v_{ps}+0,0067v_{ps}^2. The inner axles of the end bogies are equipped with traction motors. The wheel-motor unit of each of these axles contains a wheelset with a wheel diameter of 0.95 m, a two-stage gearbox with a gear ratio of 6.6 and efficiency 0.97 as well as a six-pole induction traction motor. The train has two identical traction drive systems located in each carriage. Each includes a hydrogen storage cell, a block of fuel cells, an inertial energy storage, a traction motor and conversion units.

The characteristics of the motor and the parameters of the drive are given in Table 2, 3, respectively.

Table 2

Traction motor characteristics

P_m, kW	U_m, V	I_m, A	cos φ_m	efficiency	S, %	f_1, Hz	n, rpm
250	760	228	0,88	0,944	1,3	65	1283

Table 3

Storage device parameters

Parameter	Value
Dimensions, mm: $D \times H$	900 × 830
Energy of exchange, MJ	26
Power (maximum), MW	0,27
Voltage (maximum), V	1054
Nominal current, A	250
Flywheel	
Material	Carbon fiber + SmCo
Dimensions, mm: outer diameter × inner diameter × height	700 × 440 × 580
Mass, kg	674
Moment of inertia, kg·m^2	57
Rotation frequency, 1/s: max…min	1071…421
Armature	
Number of poles	4
Pole division, mm	340
Number of phases	4
Conductor cross section, mm^2	50
Inductor	
Magnet dimensions, mm: length × height × width	340 × 420 × 15
Magnetic flux density in the active zone, T	0,22
Gap, mm	3

The movement curves, power and energy dependencies obtained for this train during its movement along a horizontal track section 24.3 km long show that the power of the power source in the form of fuel cells, as well as an inertial storage device per one car, must be at least 260 kW. The flywheel of each inertial energy storage device must accumulate exchange energy of at least 7.25 kWh during braking (the regenerative braking energy is 14.49 kWh).

Calculation and study of the operation of the traction block with the control system (Fig. 4) with the values of the parameters of the control block given in Table 4 were carried out on the basis of a mathematical model (Table 1). The fourth-order Runge-Kutta method was chosen as a numerical method for solving a system of differential equations. The calculation was carried out for three acceleration values – 0.55 m/s^2, 0.37 m/s^2 and 0.28 m/s^2. The calculation results are shown in Fig. 5.

Table 4

Control block parameter values

Parameter	Value	Parameter	Value	Parameter	Value
K_{ch0}	0,1	K_{pse}, s^2/m	7,3	$K_{ch\min}$	0,1
K_{psch}, s^2/m	3,9	$i_{\min}$, A	360	$K_{ch\max}$	4
K_{e0}, s^2/m	0,05	$i_{\max}$, A	440	$K_{e\max}$	7,3

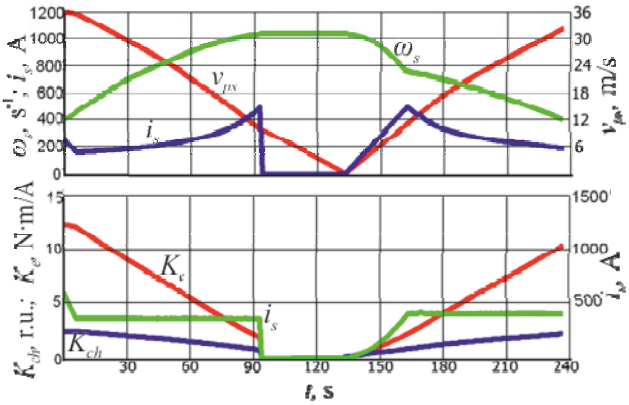

Fig. 5. Energy exchange process at acceleration of 0.55 m/s^2

The analysis of the calculation results showed that the efficiency of using the energy storage at variable accelerations in the range of 0.55–0.28 m/s^2 is 28–37 %. Thus, the use of the storage device makes it possible to save about 40 % of energy in one cycle «braking-acceleration».

For the train in question, the HyPM^{TM}HD30 fuel cell blocks are most suitable. Block power is 31 kW, current is 0–500 A, voltage is 60–120 V, maximum efficiency is 55 %, dimensions are 719×406×261 mm, mass is 72 kg. The performance characteristics are shown in Fig. 6 [15].

9 such blocks, connected in series, on each carriage will provide source power of 280 kW in the voltage range of 540–1080 V when the load changes from 0 to 500 A. Such a battery, located in a container measuring 2.2 × 1.5 × 0.4 m, will weigh 650 kg, and can be placed on the roof of the car without any problems.

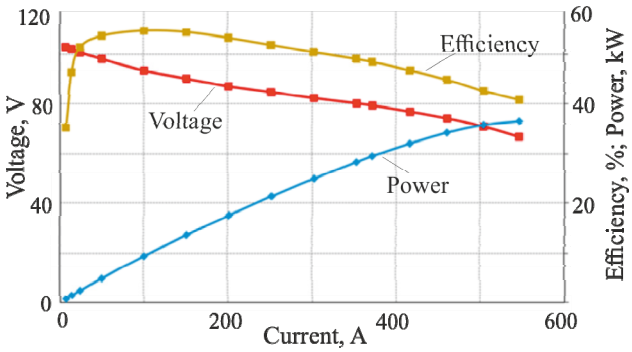

Fig. 6. Performance characteristics of the block HyPM^{TM}HD30

The necessary demand for hydrogen when the rolling stock is moving without a storage device in acceleration and driving modes with constant power is determined by the formula

$$M_H = \frac{E_{Hfc} - E_{Hs}}{E_{Hsp}\eta_E}, \qquad (27)$$

where E_{Hfc} is the electrical energy of the fuel cell battery; E_{Hs} is the energy of recuperation during braking and its subsequent use during acceleration; E_{Hsp} is the specific weight energy index of hydrogen fuel.

For our case, at E_{Hfc} = 396 MJ, E_{Hs} = 63 MJ, E_{Hsp}=120 MJ/kg and η_E = 0.55, the hydrogen consumption per one transport cycle will be 3.9 kg when operating without a storage device, and 3 kg with a storage device.

With the capacity of the currently used tanks with a pressure of 35 MPa and a mass of hydrogen of 5 kg [16], 6 such tanks with a mass of ≈700 kg and an occupied volume of 2.86 m^3 will ensure the movement 188 km of the train in question in the absence of a storage device without refueling. If the drive is storage device, the mileage will be 250 km without refueling.

Thus, the use of the storage device with its one-time use in the simplest transport cycle without taking into account the rational ratios of the parameters of the control block gives a rather tangible effect – saving at least 24.5 % of hydrogen.

Conclusions and prospects for further development.

The studies were carried out on the basis of a mathematical model of a traction electric drive of a train on fuel cells with an inertial energy storage, which is a set of separate blocks of differential and algebraic equations for a train and various blocks of a traction electric drive circuit. This model should be considered as basic. To study the behaviour of rolling stock in conditions close to real ones, it is necessary, on the basis of the developed mathematical models, to create a unified system of differential equations, with the help of which to couple the operation of all blocks of the traction electric drive system, including the operation of converting units of semiconductor devices, with the coordinates of the track both in time and in space.

The solution of such a problem will undoubtedly require the creation of a unified three-level intelligent control system.

The first level should determine the power required by the train, control the speed of the vehicle and transfer the required acceleration or deceleration to the second and third levels.

The second level should control the distribution of power and energy flows between various components of the traction chain: a fuel cell battery, an energy storage device and an actuator – a traction induction motor.

The third level should act on the controls of individual components and adjust their state depending on the power generated or consumed by these components.

Conflict of interest. The authors declare that they have no conflicts of interest.

REFERENCES

1. Thorne R., Amundsen A.H., Sundvor I. Battery electric and fuel cell trains: maturity of technology and market status. *Report 1737/2019. Institute of Transport Economics*, 2020. 32p. Available at: https://www.toi.no/getfile.php?mmfileid=52027 (accessed 22 March 2021).

2. Hoffrichter A., Hillmansen S., Roberts C. Conceptual propulsion system design for a hydrogen-powered regional train. *IET Electrical Systems in Transportation*, 2016, vol. 6, no. 2, pp. 56-66. doi: https://doi.org/10.1049/iet-est.2014.0049.

3. Fender K. *Development of hydrogen-powered trains continues, but battery-powered equipment making more inroads*. December 14, 2020. Available at: https://www.trains.com/trn/news-reviews/news-wire/development-of-hydrogen-powered-trains-continues-but-battery-powered-equipment-making-more-inroads (accessed 22 March 2021).

4. Furuta R., Kawasaki J., Kondo K. Hybrid traction technologies with energy storage devices for nonelectrified railway lines. *IEEJ Transactions on Electrical and Electronic Engineering*, 2010, vol. 5, no. 3, pp. 291-297. doi: https://doi.org/10.1002/tee.20532.

5. Ogawa K., Yamamoto T., Hasegawa H., Furuya T. Development of the fuel-cell/battery hybrid railway vehicle. *2009 IEEE Vehicle Power and Propulsion Conference*, 2009, pp. 1730-1735. doi: https://doi.org/10.1109/vppc.2009.5289693.

6. Chen X., Shen W., Vo T.T., Cao Z., Kapoor A. An overview of lithium-ion batteries for electric vehicles. *2012 10th International Power & Energy Conference (IPEC)*, 2012, pp. 230-235. doi: https://doi.org/10.1109/asscc.2012.6523269.

7. Baumann M., Peters J. F., Weil M., Grunwald A. CO_2 footprint and life-cycle costs of electrochemical energy storage for stationary grid applications. *Energy Technology*, 2017, vol. 5, no. 7, pp. 1071-1083. doi: https://doi.org/10.1002/ente.201600622.

8. Liu X., Li K. Energy storage devices in electrified railway systems: A review. *Transportation Safety and Environment*, 2020, vol. 2, no. 3, pp. 183-201. doi: https://doi.org/10.1093/tse/tdaa016.

9. Hedlund M., Lundin J., De Santiago J., Abrahamsson J., Bernhoff H. Flywheel energy storage for automotive applications. *Energies*, 2015, vol. 8, no. 10, pp. 10636-10663. doi: https://doi.org/10.3390/en81010636.

10. Engel B., Söffker C., Hörl F. *The innovative traction system with the flywheel of the Lirex^{TM}*. Available at: http://www.railway-research.org/IMG/pdf/457.pdf (accessed 22 March 2021).

11. Ogawa K., Yoneyama T., Sudo T., Kashiwagi T., Yamamoto T. Performance improvement of fuel cell hybrid powered test railway vehicle. *Quarterly Report of RTRI*, 2021, vol. 62, no. 1, pp. 16-21. doi: https://doi.org/10.2219/rtriqr.62.1_16.

12. Omelyanenko V.I, Riabov Ie.S., Overianova L.V. Inertial energy storage device as an advanced energy conservation technology for electric rolling stock. *Vestnik VELNII*, 2013, no. 1 (65), pp. 38-54. (Rus).

13. Omelianenko H.V., Overianova L.V., Maslii A.S. Geometric and electrophysical parameters of armature winding of electromechanical converter of inertial energy storage for suburban trains. *Electrical Engineering & Electromechanics*, 2020, no. 1, pp. 65-71. doi: https://doi.org/10.20998/2074-272x.2020.1.11.

14. Severin V.P., Omelianenko O.V. Traction drive of electric train with inertial energy storage. *Bulletin of the National Technical University «KhPI». Series: Problems of Automated Electrodrivs. Theory and Practice. Power Electronics and Energy Efficiency,* 2017, no. 27 (1249), pp. 276-279. Available at: http://repository.kpi.kharkov.ua/bitstream/KhPI-Press/33984/1/vestnik_KhPI_2017_27_Severin_Tyagovyy_privod.pdf (accessed 22 March 2021). (Rus).

15. *HyPM™ HD 30 Heavy Duty Fuel Cell Power Module*. Available at: https://pdf.directindustry.com/pdf/hydrogenics/hypm-hd-30/33492-420319.html (accessed 22 March 2021).

16. Ahluwalia R.K., Hua T.Q., Peng J.-K. Fuel cycle efficiencies of different automotive on-board hydrogen storage options. *International Journal of Hydrogen Energy*, 2007, vol. 32, no. 15, pp. 3592-3602. doi: https://doi.org/10.1016/j.ijhydene.2007.03.021.

Received 13.05.2021
Accepted 17.06.2021
Published 27.08.2021

V.I. Omelyanenko[1], *Doctor of Technical Science, Professor,*
Ie.S. Riabov[1], *PhD,*
L.V. Overianova[1], *PhD, Associate Professor,*
H.V. Omelianenko [1], *PhD, Associate Professor,*
[1] National Technical University «Kharkiv Polytechnic Institute», 2, Kyrpychova Str., Kharkiv, 61002, Ukraine,
e-mail: vicel@ukr.net; riabov.ievgen@gmail.com; overanova@ukr.net (Corresponding author); omeljanenkgalina@i.ua

How to cite this article:
Omelyanenko V.I., Riabov Ie.S., Overianova L.V., Omelianenko H.V. Traction electric drive based on fuel cell batteries and on-board inertial energy storage for multi unit train. *Electrical Engineering & Electromechanics*, 2021, no. 4, pp. 64-72. doi: https://doi.org/10.20998/2074-272X.2021.4.08.

Матеріали приймаються за адресою:
Кафедра "Електричні апарати", НТУ "ХПИ", вул. Кирпичова, 21, м. Харків, 61002, Україна
Електронні варіанти матеріалів по e-mail: a.m.grechko@gmail.com

Довідки за телефонами: +38 050 653 49 82 Клименко Борис Володимирович
+38 067 359 46 96 Гречко Олександр Михайлович

Передплатний індекс: 01216